THE CREEP BEHAVIOUR OF ASTM A437 GRADE B4B STEEL FOR STEAM TURBINE APPLICATIONS

A Thesis Submitted to the College of
Graduate Studies and Research
in Partial Fulfillment of the Requirements
for the Degree of Masters of Science
in the Department of Mechanical Engineering
University of Saskatchewan
Saskatoon

By
Andrew M. Hamilton

PERMISSION TO USE

In presenting this thesis in partial fulfillment of the requirements for a Postgraduate degree from the University of Saskatchewan, I agree that the Libraries of this University may make it freely available for inspection. I further agree that permission for copying of this thesis in any manner, in whole or in part, for scholarly purposes may be granted by the professor or professors who supervised my thesis work or, in their absence, by the Head of the Department or the Dean of the College in which my thesis work was done. It is understood that any copying or publication or use of this thesis or parts thereof for financial gain shall not be allowed without my written permission. It is also understood that due recognition shall be given to me and to the University of Saskatchewan in any scholarly use which may be made of any material in my thesis.

Requests for permission to copy or to make other use of material in this thesis in whole or part should be addressed to:

Head of the Department of Mechanical Engineering
University of Saskatchewan
Saskatoon, Saskatchewan (S7N 5A9)

Abstract

This study is a continuation of a project to characterise ASTM A437 Grade B4B martensitic stainless steel for use In Hitachi Canadian Industries Ltd's (HCI) steam turbine casing bolts. ASTM A437 Grade B4B steel is commercially available and was chosen for the study due to its chemical similarity to a proprietary steel currently used by HCI.

High creep resistance is essential for any candidate so creep-rupture and creep-strain tests were performed at and above the intended service temperature of 538°C. Hardness measurements and transmission electron microscopy were performed on the steel in the as-received condition as well as on crept samples to determine the effect of elevated temperature on the development of the steel's microstructure.

During testing, it was found that ASTM A437 Grade B4B steel has a well defined second stage leading to an abrupt transition into the third stage. The second stage begins in the first 10% of its creep life, while the third stage begins at 90% of its creep life. This equates to 5% and 30% of the final strain, respectively, with an average final strain of 20%.

Time-to-Rupture data show good similarity to the creep life as predicted using the Larson-Miller method. When plotted, the steady-state creep rate shows a definite correlation between the creep stress and temperature. From this an empirical relationship was developed to predict the steady-state creep rate.

Transmission electron microscopy (TEM) results showed a significant change in the microstructure between crept and as-received steel. Coarsening of carbides along grain boundaries most likely led to a recovery of the microstructure in the crept samples. Literature suggests that the composition of the carbides is most likely tungsten and molybdenum intermetalics and carbides that coarsened from the depletion of chromium from solution. This was supported by energy dispersive spectroscopy (EDS) analysis.

The coarsening of carbides correlates with the decrease in creep resistance of the material and it is likely that the growth of precipitates and recovery of the microstructure causes the entry of the steel into third stage creep.

Acknowledgements

I would like to acknowledge the following for their contributions to this project:

I would like to thank my supervisor, **Dr. Spiro Yannacopoulos**, for allowing me to work on the project and for all his guidance. **Dr. Ikechukwuka Oguocha**, for his guidance and much appreciated help in editing this work. **Mr. David Crone**, for assistance in the laboratory and allowing me to generally do as I like.

I would also like to thank **Mr. Henry Berg** and all the members of **Engineering Shops** as well as **Sherri Haberman**, **April Wettig** and all the administrative staff.

Lastly but not least, I would also like to thank **Mr. Tom Kishchuk** and **Hitachi Canadian Industries Ltd** for providing funding for the project.

Table of Contents

List of Tables

List of Equations

List of Figures

List of Symbols

ε – Strain (creep strain)

σ – Stress (creep stress)

E – Modulus of Elasticity / Young's Modulus

$\acute{\varepsilon}_{ss}$ – Steady state strain rate

Q – Creep activation energy

R – Ideal Gas Constant, 1.987 cal/mol·K

T – Absolute temperature (K)

T_m – Melting Temperature (K)

A – Material Constant

n – Coefficient of stress

C – Larson-Miller constant

t_r – Time to rupture (hrs)

m – Mason- Haferd constant

t_a – Mason-Haferd convergent time

T_a – Mason-Haferd convergent Temperature

$\acute{\varepsilon}_1$ – average strain rate of stage 1

$\acute{\varepsilon}_2$ – average strain rate of stage 2

$\acute{\varepsilon}_3$ – average strain rate of stage 3

τ_1 – time to stage 1 maximum strain rate

τ_2 – time to minimum strain rate (second stage)

τ_3 – time to stage 3 maximum strain rate

M – Metallic atom

X – Carbon or Nitrogen atom

List of Acronyms

ASTM – American Society of Testing and Materials

EDS – Energy Dispersive Spectroscopy

HCI – Hitachi Canadian Industries Ltd.

STEM – Scanning - Transmission Electron Microscope

SVLC – Super Variable Linear Capacitor

TEM – Transmission Electron Microscope

U of S – University of Saskatchewan

1.0 Introduction

1.1 Introduction to the Creep Testing Problem

Due to changes in the market, the current growth of HCI is towards refitting and rebuilding of existing power plants as opposed to the design and sale of new equipment. The Hitachi 12%CrMoVW stainless steel is only manufactured in Japan. As a result, the long turnaround time needed for the steel to arrive from Japan does not facilitate the schedule needed for a plant shutdown. Using an ASTM grade of steel manufactured in North America can shorten turn around time to fit the most demanding schedule. Unfortunately, most ASTM grades that meet HCI's requirements have had little long term testing and not much is known about how they will perform under elevated temperature service.

Creep is defined as the continuous deformation occurring in a material subjected to constant loading. In common application the deformation occurs at a very slow rate. This can make testing difficult as conditions have to be duplicated so that the time it takes for a material to fail is shortened enough that it can be studied, but not shortened so much that different creep mechanisms become active that wouldn't normally be expressed in service. Due to this problem, creep-strain and creep-rupture data obtained from testing cannot be used independently to predict service life until the mechanisms responsible for the creep behaviour are understood.

The work presented in this thesis is the result of collaboration between the Department of Mechanical Engineering at the University of Saskatchewan and Hitachi Canadian Industries Ltd.(HCI). The objective of this collaboration is the characterization of a

suitable replacement for a 12%CrMoVW stainless steel currently used by HCI for steam turbine casing bolts with more readily available steel.

1.2 History

In 1999, HCI Ltd. donated ten creep test frames to the Department of Mechanical Engineering at the University of Saskatchewan for characterizing the high temperature behaviour of suitable replacement materials for the proprietary steel. Shane Griffin [1] began work on the project by studying the following three common grades of ASTM steel: (i) A193 Grade B16 – low alloy CrMoV martensitic steel, (ii) A355 Class A – low alloy nitride hardenable steel, and (iii) A437 Grade B4B – high alloy CrMoVW martensitic stainless steel.

The ASTM A437 Grade B4B had the highest resistance to creep deformation of the three and also showed a very prominent second stage (a period where the sample deforms at a constant rate) over the lifetime of the sample.

Initial testing of the ASTM A437 Grade B4B steel was promising and the work was continued by Darryl McCullough [2] into further characterizing the steel's high temperature performance. Creep testing as well as microstructural investigations into the development of the microstructure in the steel was continued. Hardness testing was performed on samples at different stages in its life to determine when major microstructural changes occurred in the steel. Scanning electron microscopy (SEM) was then utilized with energy dispersive x-ray spectrometry (EDS) to further map the development of the steel's microstructure. Although EDS could not specifically identify what phases were forming during creep, it was suggested that a recovery of the microstructure and a coarsening of sub-grain carbides were occurring.

1.3 Objectives

Since the inception of the project in 1999, a great deal of creep-rupture and creep-strain data have been generated for ASTM A437 Grade B4B. The evolution of the steel's microstructures during creep has also been investigated. Only recently, enough creep data has been available to develop a comprehensive model of the steels development. The objectives for this thesis are:

- Using the generated time-to-rupture data, determine if established models of creep prediction are able to accurately predict the creep life of ASTM A437 Grade B4B steel.
- Using creep-strain data determine if a relationship exists between the steady-state strain rate and test conditions that will allow prediction of second-stage creep life.
- The microstructure of crept steel will be compared to the as-received steel to determine what, if any changes are occurring during creep testing. By identifying what is occurring in the evolving microstructure, the validity of the creep testing can be established.
    - This will include a metallographic examination that will be described in Chapter 3 of this thesis.

1.4 Scope and Methodology

In earlier work by Shane Griffin [1], it was determined that ASTM A437 Grade B4B could be characterized by the Larson-Miller method. However, the limited range of creep data made predicting long term performance difficult.

- To design the testing schedule for the work described in this thesis, the Larson-Miller method was used to estimate the time-to-rupture of each test. The estimates were then compared to the actual time-to-rupture to determine the accuracy of the method.

- The Larson-Miller parameter was also calculated for each test in order to generate a Larson-Miller master plot for ASTM A437 Grade B4B. The linearity of the plot is an indication of the validity of the method.
- Other properties, such as the time spent in each stage of creep, the steady state creep rate, etc. were calculated using creep-strain data from testing. This information was then used to further characterize the material and determine where to begin the metallographic analysis.

From analyzing the creep data it was theorized that the material undergoes a significant change during the end of second stage creep, possibly responsible for triggering the material's entrance into third stage creep. To try and confirm this, a metallographic examination was performed on both crept samples and material in the as-received condition.

- Changes in steel's microstructure can be correlated to its strength. Hardness measurements were performed on each sample from areas in the gauge length that exhibited both temperature ageing and high stress. This was compared to the hardness measured from outside the gauge that would have been exposed to significantly lower stress.
- Transmission electron microscopy was used to compare the microstructure of crept and as-received material. By doing so, mechanisms responsible for changes could be identified and correlated to what was observed in the creep-strain data.
- Due to time restraints, a metallographic comparison of samples at different stages of creep was not attempted.

1.5 Thesis Outline

A review of the literature on creep and the effects of high temperature and stress on metals focusing on steel is contained in Chapter 2. This chapter also contains a literature review on the microstructural evolution of martensitic high alloy steels under high temperature and stress.

The experimental methods used, including the equipment and procedure used during creep testing and the derivation of the testing schedule used in the study, are explained in Chapter 3. A review of the metallographic equipment used in the study and the experimental procedure are also included.

Chapter 4 focuses on three separate sections: a discussion of the creep data generated during the project, the results from hardness testing, and the metallographic results.

Chapter 5 concludes the results of the study discussed in the previous chapter.
There are two appendices, the first containing the creep data generated during the study and the graphical analysis of the data. The second contains the derivation of the empirical steady state creep equation for ASTM A437 Grade B4B steel.

2.0 Literature Review

2.1 Creep

2.1.1 Introduction

Creep is a process where continuous deformation occurs in a material subjected to constant loading. A typical example is a pressure vessel. The vessel will remain at a relatively constant pressure during its lifespan and a constant stress will exist in the shell, welds and/or bolted connections. If the pressure in the vessel creates a stress greater than the yield strength of the steel, the bolt will continuously strain and over time fail [3]. In this section the mechanics of creep and methods used to predict it in steel are discussed.

2.1.2 Effect of High Stress and Temperature on Steel

Creep is characterized by continued increasing strain in a material exposed to constant loading. The strain can occur at temperatures as low as room temperature if the load on the material is high enough to cause yielding; however, creep is not usually seen until the service temperatures reach approximately 40% of the material's melting temperature [3]. An example of this is the relaxation of high tension bolted connections used at elevated temperatures, such as in a steam turbine. In service, the bolt will begin to creep, reducing the preload on the stud. As the preload decreases, the creep strain rate will slow until a maximum strain is reached; however, the reduction in preload may be significant enough that cyclic loading is introduced [4]. Because of this, a crept bolt will not usually fail in tension but rather due to a combination of fatigue and creep.

2.1.3 Stages of Creep

The creep strain-rate of a metal subjected to a static loading at an elevated temperature is not constant and will exhibit three characteristic stages: primary creep, secondary creep, and tertiary creep. These stages are illustrated in Figure 2.1. The initial strain that appears in the diagram is the instantaneous strain due to the initial loading of the sample.

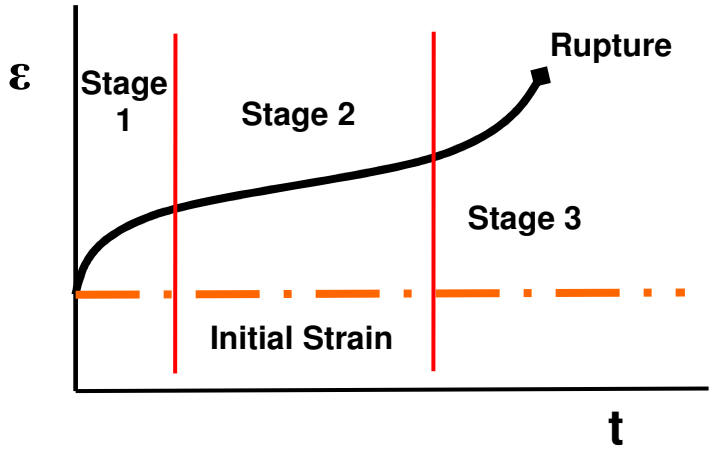

Figure 2.1. Strain vs. Time Plot (Creep Plot) [5].

Primary creep (stage one creep) is characterized by a period of rapidly decreasing strain rate. This is due to dislocation glide being balanced by the work-hardening of the metal. At first, dislocation movement is relatively free but as dislocations multiply during further strain, the dislocation density increases and dislocations begin to tangle. The tangling of dislocations is what hardens the material. Eventually, the two competing mechanisms, dislocation movement and work hardening, will cancel each other out resulting in a constant or steady-state strain rate. This steady-state strain rate defines the second stage of creep and in most low alloy steels, can be used to characterize the overall creep life of the steel. As the material continues to strain, micro-fractures and an eventual reduction in area of the sample will occur and increase the strain rate. As the strain rate increases, the flaws continue to grow, which in turn continues to increase the strain-rate until the material reaches its true tensile limit, causing the sample to fracture. Changes in the microstructure, such as the physical growth and agglomeration of

carbides or the destruction of the grain boundaries recovery or migration, can also lead to an increase in the strain-rate. It is thought that changes in the material microstructure are what cause the rapid increase in strain rate, which is characteristic of third stage creep [5].

The strain-time curve shown in Figure 2.1 is characteristic to all materials, but slight differences in the shape of the plot will distinguish between materials. For example, a predominant second stage creep characterizes most pure metals and low-alloyed metals but in other metals, such as high alloy steels, the characteristic constant strain rate is reduced to a point of minimum creep rate [6]. When a material exhibits this type of curve, life prediction becomes difficult as the curve loses its linearity. This is discussed in more detail in Section 2.1.5.

2.1.4 Mechanics of Creep

As mentioned in Section 2.1.3, creep occurs as a result of competing mechanisms such as dislocation glide, work hardening (dislocation tangling) and evolution of the microstructure. These mechanisms are discussed in more detail in this section. Depending on service conditions such as temperature and loading, different mechanisms will become dominant and affect the creep strain-rate as well as the development of the microstructure. Figure 2.2 is an illustration of which mechanism will become dominant under different conditions; the temperature scale is normalized to the melting point of the material and the stress to its modulus of elasticity. Precise temperatures where mechanisms become dominant will vary for different alloys. These mechanisms may overlap and be present at the same time.

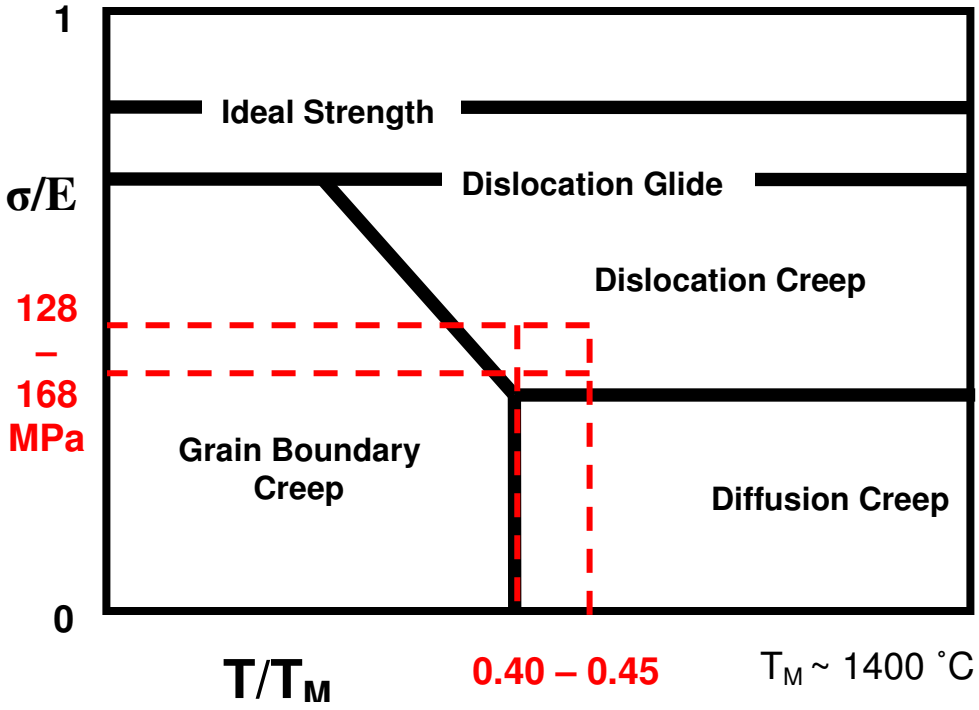

Figure 2.2. Creep Mechanism Dominance Plotted over a Normalized Stress-Temperature Map [7] (Testing temperatures used and the intended service stress are indicated in red).

2.1.4.1 Grain Boundary Sliding

As shown in Figure 2.2, grain boundary sliding is primarily dominant at low to intermediate temperatures. This mechanism is characterized by grain boundaries physically slipping due to high stress fields in their vicinity. The growth of precipitates at the grain boundaries will effectively pin grain boundaries preventing movement [5] The neighbouring grains may also act to effectively prevent grain boundary sliding by changing the forcing the plane of sliding to change direction. As a result, a material with a fine microstructure will tend to be highly resistant to grain boundary sliding as the path of slip will be forced to change repetitively. In comparison, a material with a coarser grain structure will not be as effective in resisting grain boundary sliding as the path of sliding will be relatively linear [8].

2.1.4.2 Diffusion

At high temperatures (0.4 T_m) but under relatively low load, the material will gain enough energy for atoms to overcome inter-atomic forces and move to new positions (vacancies) within the matrix. The energy for an atom to overcome inter-atomic forces is called the activation energy and is considered a material constant [8]. The activation energy may change as the material undergoes an evolution during creep, or in the case of steel, if they are heat treated to alter their microstructure. When a material is heated and the activation energy is reached, atoms are able to move to vacancies causing the material to flow and strain when otherwise it would remain solid. This type of strain is called diffusion creep [5]. Diffusion of atoms can also cause dislocations that had previously been either constrained by other dislocations or blocked by inclusions, faults or precipitates, to have enough energy to overcome these barriers and allow the metal to creep. The diffusion mechanism dominates at high temperatures and is considered to be the main driving mechanism for creep.

2.1.4.3 Dislocation Movement

All metals contain defects that interrupt the crystalline structure. Some defects occur when crystalline structures of different orientation join, creating a large continuous interface. These interfaces are called grain boundaries. Other defects can occur within the crystal structure on a much smaller scale; these are referred to as dislocations [9]. Dislocations can either express themselves as a distortion along a plane in the crystalline matrix creating an edge dislocation, or pass through the crystal planes in a helical pattern, creating a screw dislocation. These are shown in Figure 2.3.

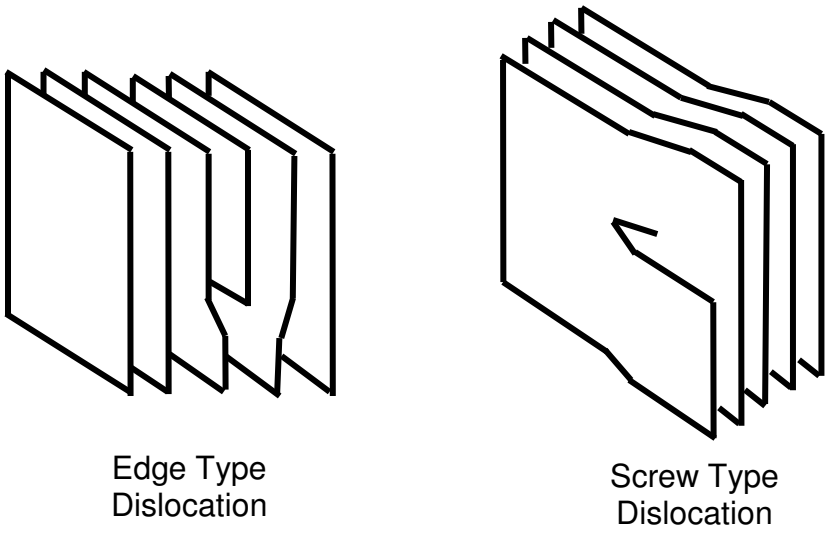

Figure 2.3. Schematic representation of edge and screw type dislocations.

The dislocations in the lattice are at a higher energy state than the surrounding matrix and will try to return to a lower energy state by removing the discontinuity. When a stress is applied to the material, a dislocation will begin to move through the matrix parallel to the stress field until it reaches the end of the structure, such as a grain boundary. Edge dislocation movement is illustrated in Figure 2.3. As the vacancy flows through the crystalline matrix it results in a permanent strain [5].

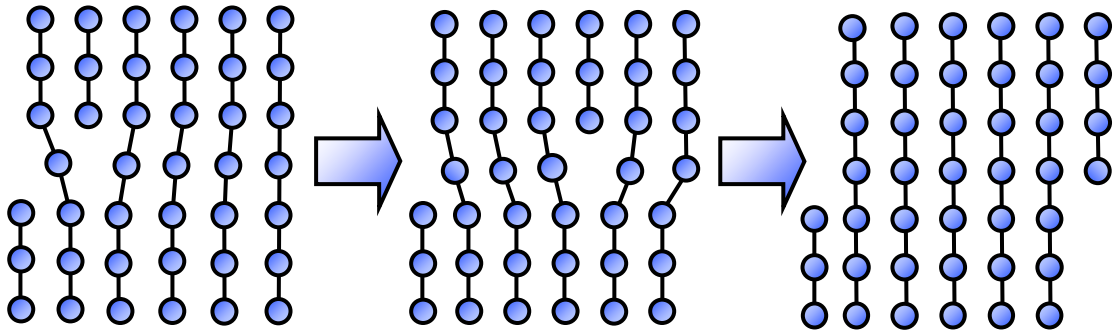

Figure 2.4. Dislocation movement causing permanent strain.

2.1.4.4 Dislocation Glide

According to Figure 2.2, dislocation glide occurs at high levels of stress. This mechanism occurs due to the movement of a dislocation through a metal due to shear forces acting upon it. The stress fields force high energy dislocations to move to lower energy areas such as grain boundaries. When significant dislocations are present, this mechanism is called dislocation slip and can be seen in the slip bands that appear in steel during the onset of yielding [9].

Dislocation climb is similar to dislocation glide. In climb however, the dislocations move from vacancy to vacancy in the structure. Quite often the vacancies are above or below the dislocation's slip plane causing it to jump or "climb" to the new plane, giving the mechanism its name. This form of movement is more commonly found in high temperature service due to the high diffusive energies needed for vacancies to diffuse towards dislocations.

2.1.4.5 Dislocation Creep

Dislocation creep is a combination of dislocation glide and diffusion. The dislocation will begin to glide due to a stress field but can easily become immobilized by becoming tangled with other dislocations or blocked by discontinuities in the matrix such as precipitates. At elevated temperatures, vacancies will move towards dislocations, allowing them to glide over barriers that would have impeded movement at a lower temperature and continue to move through the material in a new plane. This action is shown in Figure 2.5. In most elevated temperature service, dislocation creep is the dominant mechanism of deformation.

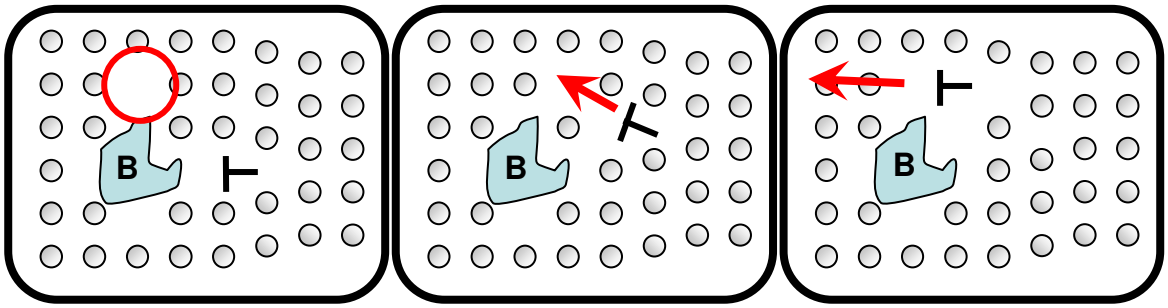

Figure 2.5. (a) At low temperatures dislocation (⊥) is pinned by presence of precipitate (labled B) (b) at higher temperatures the dislocation can diffuse to vacancy (outlined in red) in a different plane and (c) continue.

2.1.5 Methods of Creep Prediction

Traditionally, creep life prediction was very inaccurate and required a large amount of testing to be performed as creep tests needed to be in the order of the same length of time as the intended service life. Strain-time plots were generated over a range of temperatures and loading that could result in decades of testing in order to accurately portray the life expected in service. Creep characteristics for the metal at different temperatures and loading would then be inferred from the creep life and the final elongation then estimated for different conditions [10]. As the amount of data for different metals and alloys began to become available, researchers saw trends in how different materials would react. Work to derive equations that could characterize a material and estimate its strain-rate and creep life began. One of the first usable theories was the Larson-Miller method, first published in 1952 [11]. It was developed using data gathered from plain carbon steels and was intended as a generic formula to quantify a steel's behaviour over time under different temperatures and loading. In order to make a generalized equation, the method makes some very broad assumptions, and as a result, the method will not be accurate for many alloys without significant modification. The first assumption made is that creep is purely dependent on diffusion. This assumption is valid when characterizing steels during heat treating, tempering, and other high temperature low stress applications but during creep, the steel is exposed to significant loading and the stress field in the steel contributes greatly to dislocation movement.
It was also assumed that the steady-state strain exhibited in the second stage of creep can be used to characterize the entire creep life of the steel. In some steels this may hold

true, but for most ferrous and non ferrous alloys, the second stage can be very short to the point of being a single point of inflection of minimum strain rate. This again reduces the accuracy of the Larson-Miller method. Equation 2.1 was developed using the Larson-Miller method and is used to predict the steady-state strain rate of steel during second stage creep [11].

$$\dot{\varepsilon}_{ss} = A\sigma^{n} \exp\left(\frac{-Q}{RT}\right) \tag{2.1}$$

where

$\dot{\varepsilon}_{SS}$ is the steady state creep rate

A is a constant

σ is the creep stress

n is a material constant

Q is the material's activation energy

R is the ideal gas constant (8.134 J/mole K)

T is the absolute temperature in Kelvin

The equation is very similar to a generic diffusion equation and assumes that the steady-state strain rate is predominantly due to diffusion creep. In most cases, the activation energy constant used in the formula is almost identical to the material's specific activation energy. The factor, *n*, is material dependent and ranges from 3-8. For pure metals, *n* is always 5.

Comparing creep data from various low alloy steels, Larson and Miller determined that the final strain or elongation of steel before it ruptures will be a constant no matter what temperature the sample is tested at or loaded to. Taking Equation 2.1 and integrating the strain rate over the creep life of the steel, Equation 2.2 was developed.

$$T\left(C + \log_{10} t_r\right) = 0.434\left(\frac{-Q}{RT}\right) \tag{2.2}$$

where

T is the absolute temperature in Kelvin

C is the Larson - Miller constant

t_r is the time to ruputure

The integration constant, C, is material dependent but is considered to be constant for most plain carbon steels and is often taken to be 20.

The Larson-Miller method is considered to be accurate for a large range of different materials but is most commonly used with low carbon steels or any material that is characterized by a large period of steady-state creep. Despite this, the method may easily be adjusted to characterize other alloys. By testing a specific material at constant stress over different temperatures, the data will begin to converge at a specific rupture time as the test temperature tends to infinity. This convergence point will be the specific Larson-Miller constant for the alloy.

Most of the commonly used methods of predicting creep life are based on the Larson-Miller method. The most commonly used of these is the Manson-Haferd method [12]. Manson and Haferd used similar assumptions as Larson and Miller but disagreed in one specific area. Larson-Miller assumes that the effect of stress upon the creep life will diminish since the time-to-rupture converges to a constant as temperature increases. Manson-Haferd agrees that iso-stress tests would converge at a specific time-to-rupture as well, but theorized that the effect of stress will become inconsequential at a finite temperature. These differences are demonstrated below in Figure 2.6. While the Manson-Haferd plot shows a finite temperature (T_a) when rupture time becomes constant, the Larson-Miller method indicates that convergence occurs at an infinite temperature.

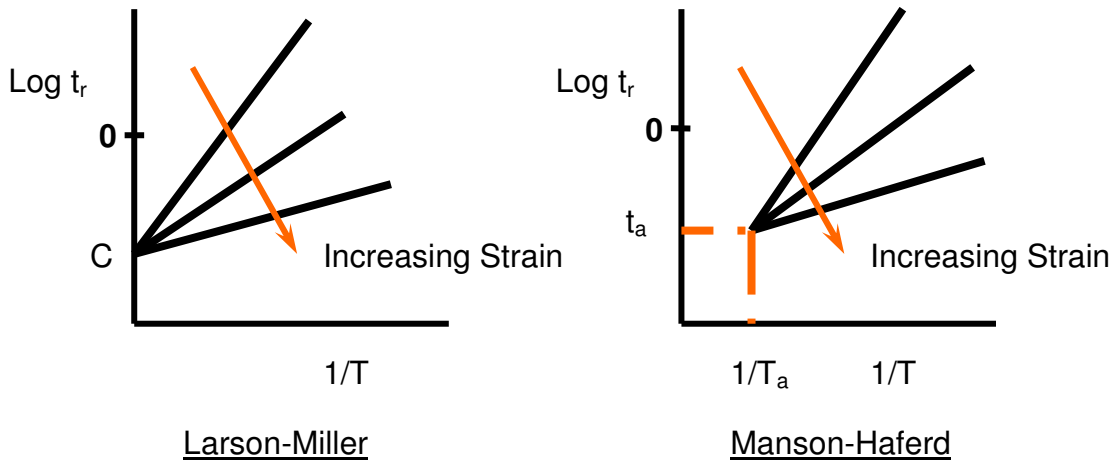

Figure 2.6. Comparison of Larson-Miller/Manson Haferd Theories [11, 12].

Taking into account these differences, Manson and Haferd developed Equation 2.3. T_a and t_a represent the temperature and time respectively, that a plot of iso-stress test will converge.

$$\frac{\log t_r - \log t_a}{T - T_a} = m \tag{2.3}$$

where

m is the Manson - Haferd constant

t_a is the time to convergence

T_a is the temperature at convergence

To verify the equation, Manson later began testing a variety of different materials. He found that the convergence point is a constant, as in the Larson-Miller equation. This reduces t_a and T_a to constants, leaving only the variable, m, a function of type and amount of loading applied to the material. As a result, Equation 2.4 was developed, which is only a function of stress and temperature.

$$\log t_r + \frac{\log^2 t_r}{40} - \frac{40000}{T} = m \tag{2.4}$$

where

t_r is the time to rupture

m is the Manson - Haferd constant

T is the absolute temperature in Kelvin

The Larson-Miller and Manson-Haferd methods are the most commonly used models for predicting creep life. When compared, the modified Miller-Haferd method is considered to give overly conservative results, generally predicting the time to rupture to be much less than what is predicted by the Larson-Miller method. For both methods, accuracy can be greatly improved by determining the actual Larson-Miller or Manson-Haferd constant for the specific material.

Work has also been done to develop an equation that can be used to represent the full stress-time plot of specific steels. Being able to develop such an equation would be very beneficial as it would be able to accurately describe the creep nature of a material and not just the time-to-rupture or constant strain-rate. Unfortunately, most of these methods rely heavily on empirical methods such as curve fitting to a set of test data to generate a formula. The resulting formulas are generally filled with constants specific to material and loading conditions and require extensive experimentation to be able to apply them to specific steel. For example, the Batsoulas' equation [13] (Equation 2.5), one of the most recent attempts, has a total of five individual constants (k_1 to k_5), each one interdependent on temperature, loading and material properties. Because of this, there is no way to apply this equation to a specific material without extensive testing.

$$\varepsilon = \frac{k_5 e^{k_1 t}}{k_2 k_3 + k_4}\left(1 - e^{-\left(k_2 + \frac{k_4}{k_3}\right)}\right) \tag{2.5}$$

where :

k_1, k_2, etc are empirically derived constants

To combat this problem, work has been done to create a general equation [13] (Equation 2.6) based on an average creep rate expressed in each of the three stages and the time the material spends in each stage.

$$\varepsilon = \frac{\left(\dot{\varepsilon}_1 - \dot{\varepsilon}_2\right)t}{\left[1+\left(\frac{t}{\tau_1}\right)^{n_1}\right]^{1/n_1}} + \frac{\left(\dot{\varepsilon}_2 - \dot{\varepsilon}_3\right)t}{\left[1+\left(\frac{t}{\tau_2}\right)^{\tau_2 n_{21}/\tau_3}\right]^{\tau_1/\tau_2 n_2}} + \dot{\varepsilon}_3\, t \qquad (2.6)$$

where :

- $\dot{\varepsilon}_1$ is the average strain rate of stage 1
- $\dot{\varepsilon}_2$ is the average strain rate of stage 2
- $\dot{\varepsilon}_3$ is the average strain rate of stage 3

τ_1, τ_2, τ_3 are time constants based on the time to each point of inflection

The advantage of this equation is that as its constants reflect the steel's development at key points in its creep life and a great deal of specific information can be gained from the constants. The drawback of the equation is that it requires a great deal of testing to generate enough data for a specific material over a range of service conditions.

All these methods of theoretically predicting creep rate have one thing in common: they all try to predict creep life through empirical methods like simple curve fitting from extensive testing. With the power of personal computers increasing and their prices continuing to drop, numerical methods are becoming more accessible to predict creep life and the evolution of microstructures. A common method is to use finite element method software to predict the life of components that are either made up of different materials or have specific zones that exhibit different known characteristics at high temperatures. A second approach is to use software to model different processes to try and predict how the microstructures of a specific metal will develop over time and from this infer creep life.

To explain how a finite element process would work, the weld creep life of a pressure vessel will be used as an example [14]. A weld is an example of a multi zoned element made up of three specific areas. This is illustrated in Figure 2.7.

Zone 1 is the deposited weld material and assuming the example is carbon steel, it is composed of a supersaturated well ordered lathed martensitic microstructure. Characteristically, this zone is very hard and brittle when compared to the parent material. Zone 2 is the heat affected zone, made up of parent material whose microstructure has been altered by high heat flux passing through it as weld material is deposited. Zone 3 is parent material unaffected by the heat from welding. Each zone can have very different properties due to the welding process and type of weld material used. As a result it can be very difficult to predict a weld's creep life.

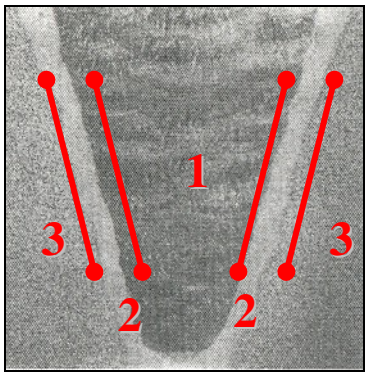

Figure 2.7. Weld zones [14].

Recently, finite element software has been used to model the welded area [14]; this is fairly simple to do as a weld has very well defined boundaries. By entering in the basic material properties for each zone and using empirically developed equations, the strain rate in the secondary and tertiary stages can be quite accurately predicted. This is shown in Figure 2.8.

Three isothermal creep tests were run at creep stresses of 85, 100 and 110 ksi (shown by the dotted curves). Creep strain was then calculated as a sum of all three zones using a numerical simulation (solid line curves) and plotted against experimental data. All numerical results showed good comparison to experimental tests, particularly at the lowest load level at which diffusion creep becomes more dominant and creep prediction

methods like the Larson-Miller can be made more accurate by using empirical data. Expanding on this, a complex composite's creep behaviour could be accurately modelled and predicted, allowing optimization of designs to reduce maintenance as well as increase performance.

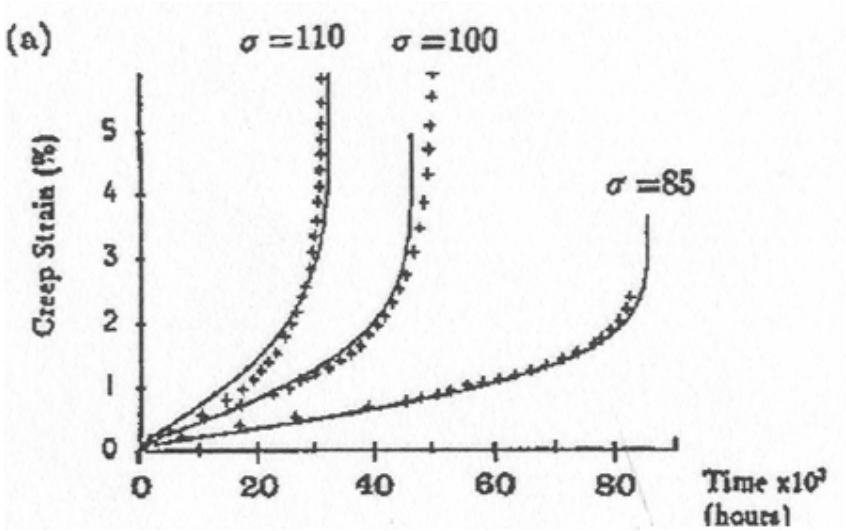

Figure 2.8. Theoretical and experimental secondary and tertiary creep plot [14].

The second method goes one step further. Instead of applying traditional empirically derived equations to macro sections of material, the microstructure is modeled and properties determined by calculating subgrain interaction. Currently, models have been developed that can very accurately determine the microstructure of a metal in a specific stage of development [15]. With this model, one can predict how different radiation or ultrasonic waves will be scattered and create different methods of non destructive testing to determine the remaining life in a component.

The accuracy of static models has increased but they still cannot be used to predict creep characteristics or the microstructural evolution of an alloy. Recently models have been built using three dimensional cell units that can very accurately model dislocation growth and interaction to predict strain hardening [16]. These models use varying cubic cells to represent grain structure. An individual cell can then have attributes applied to it such as dislocation density. By summing the interactions of the cells, gross properties of a metal can be determined. By then adding external forces, a stress strain plot could be

generated with a high degree of accuracy. Examples of this can be seen in Figure 2.9. In the first plot, different stress strain curves have been generated based on the method of deformation. In the second plot, the post yield strain hardening rate has been generated for different deformation modes. This is of great benefit as traditional tensile testing cannot accurately predict how a material will behave under different modes of deformation. Numerically modeling an unusual deformation mode could reduce the amount of physical testing needed and to characterize how a material will react.

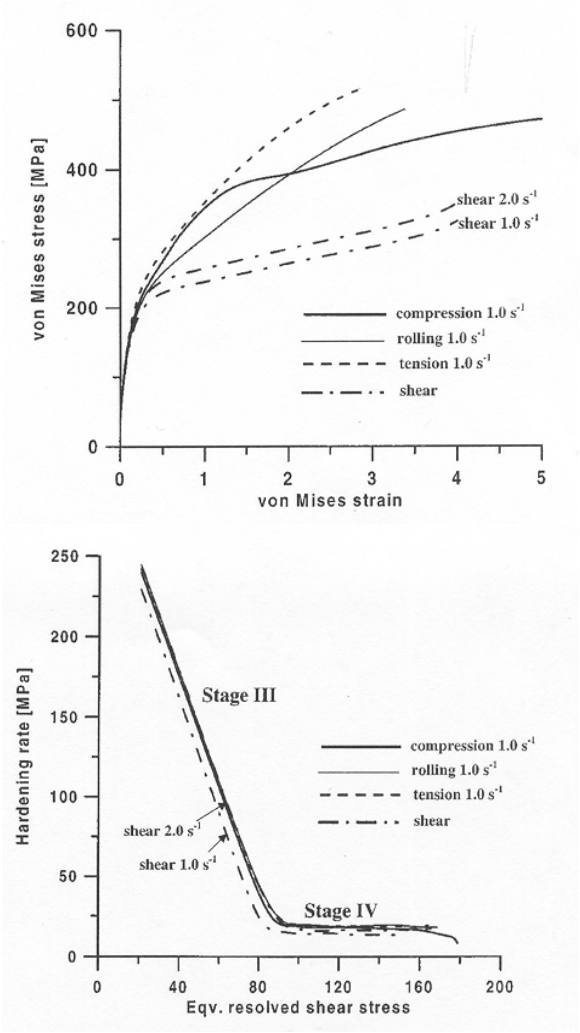

Figure 2.9. Theoretical and experimental comparison between numerically generated and measured stress-strain curves [16].

Another group [17] is experimenting on dynamically modelling precipitation density and coarsening. Using diffusion equations and an understanding of the metal's evolution, they have been able to extrapolate precipitation rates. These, in turn, are related to different points in the material's creep life and can be used to calculate strain rate and finally creep life. They have also been able to make phase maps of very complex steel alloys in order to identify the evolution of the microstructure at different temperatures. Numerical and experimental comparisons of carbide precipitation density growth rate are shown in Figure 2.10.

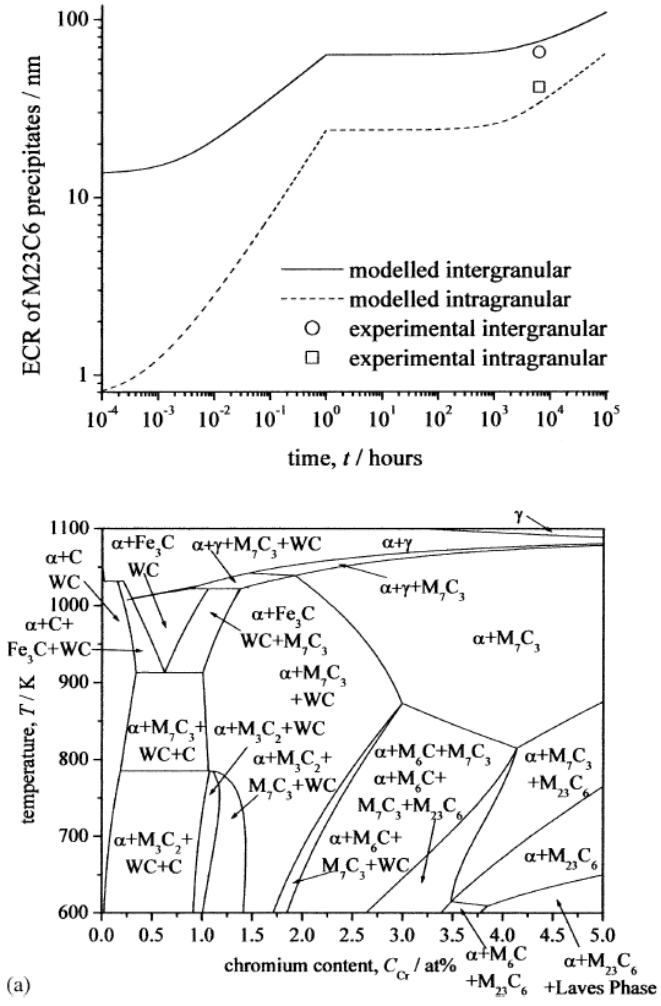

Figure 2.10. (a) Theoretical model of $M_{23}C_6$ precipitation density growth (b) Theoretical phase diagram [17].

In theory, the model's complexity could be increased by further incorporating more experimental data. In time, it is conceivable that such a model could be used to calculate the creep behaviour of a metal under any conditions.

2.2 Materials

2.2.1 Steel

Steel is an alloy of iron and carbon that is characterized by having a carbon content of no more than 2.1 wt. % [6]. Alloys of iron and only carbon have disadvantages. For example, steel alloyed with a large amount of carbon (i.e. tool and knife steels) will be strong but at the same time extremely brittle with very low toughness. While this might be appropriate for some applications, it is more often a negative trait. As a result, steel is commonly alloyed with elements other than carbon to increase its strength. Depending on the concentration and type of alloying elements used, steel can be made to exhibit many different properties to meet specific requirements. Due to the ease of customization, there are many different varieties of steel on the market and classification can become very difficult. As a result, most steels are categorized by their mechanical properties (American Petroleum Institute grades of steel), use (tool steels) or microstructure (austenitic stainless steels, trip steel) and generally not their chemical composition like magnesium or aluminium alloys. The following is a breakdown of the more common alloying elements found in steel and their effect upon properties [6][18].

Chromium (Cr) is added to stainless steels to create a durable oxide layer that protects the steel from corrosion. The increased resistance to corrosion is what gives the steel its name. Chromium also increases the hardness, strength and wear resistance of steels but most significantly increases the hardenability of steels (the steel's ability to create martensite, a strong but brittle iron phase). Nickel (Ni) is commonly added to increase corrosion resistance but in the low amount that it appears in A437 Grade B4B, it will mainly increase its hardenability. During hardening, the steel is rapidly cooled below the Martensite Start (Ms) temperature. This is the temperature that martensite begins to

form instead of the carbon diffusing out and creating iron carbide. The addition of nickel and chromium will raise the Ms point increasing the lowest temperature that martensite will begin to form. Nickel also counters the ferrite forming effects of molybdenum and vanadium, allowing a higher concentration of these metals present in the steel without decreasing strength.

Manganese (Mn) will increase the strength and hardenability of steel by increasing the Ms point.

Molybdenum (Mo) will increase the toughness, hardness and creep resistance of a steel. Molybdenum also stabilizes M_2X phases, small dislocation blocking carbides that are essential in preventing creep, by slowing coarsening of the phase that will lead to a decrease in the creep resistance of steel [19].

Vanadium (V) behaves similarly to molybdenum as it is very effective in stabilizing small carbides. However, it has the disadvantage of increasing the amount of ferrite retained in the microstructure by inhibiting the formation of martensite. This effect is usually countered with the addition of nickel.

Tungsten (W) has a similar effect as molybdenum in stabilizing M_2X precipitates but also will increase the precipitation of these carbides and raise the maximum allowable tempering temperature of the steel [19]. By allowing steel to be tempered at higher temperatures, the microstructure will become stable when in service at temperatures lower than tempering. This will allow the steel to be able to be used at higher operating temperatures. This makes tungsten an essential additive to any hardenable steel intended for elevated temperature use.

Carbon (C) gives steel its strength and is essential in creating the high strength martinsite phase. It also has high affinity to chromium and other precipitate-forming metals and at higher temperatures will actively pull chromium and other metals out of solution to create carbides. This can create large chromium deficient areas that will

substantially decrease the corrosion resistance of the steel. As a result, most steels used in high temperature environments will contain no more than 0.3% by weight carbon. Nitrogen also has similar strengthening effects but does not have as strong an affinity to chromium as carbon does; subsequently it is often used to replace carbon as a strengthener. Nitrogen is commonly added by exposing the steel to a nitrogen-rich environment at elevated temperatures. This process is called nitriding and will result in a hard durable shell at the surface of the steel where nitrogen is diffused into the steel, but will still have a tough interior increasing the fatigue and wear resistance of the steel. Increasing the chromium content to 16-18% will also minimize the effect of carbon removing it from solution, but at the same time will reduce the hardenability of the steel and substantially increase the cost.

2.2.2 12% Cr Martensitic Steel Microstructure and Development

When alloying two or more metals together, the solute atoms can either replace atoms in the lattice (substitutional) or occupy the space between atoms in the lattice (interstitial). These methods of strengthening are referred to as substitutional solid solution strengthening and interstitial solid solution strengthening respectively. This is shown in Figure 2.11. In interstitial solid solution strengthening, atoms of the alloying elements are small enough to occupy interstitial positions within the matrix, physically restricting the movement of dislocations by pinning voids. In steels, carbon and nitrogen are interstitial strengtheners and are commonly added as a means of increasing strength. In substitutional solid solution strengthening, the solute atoms are equivalent in size to the parent metal and will replace parent atoms in the crystaline matrix. The substitutional atoms, while being on the same order of magnitude as the matrix atoms are still able to effectively pin dislocation movement [6, 10]

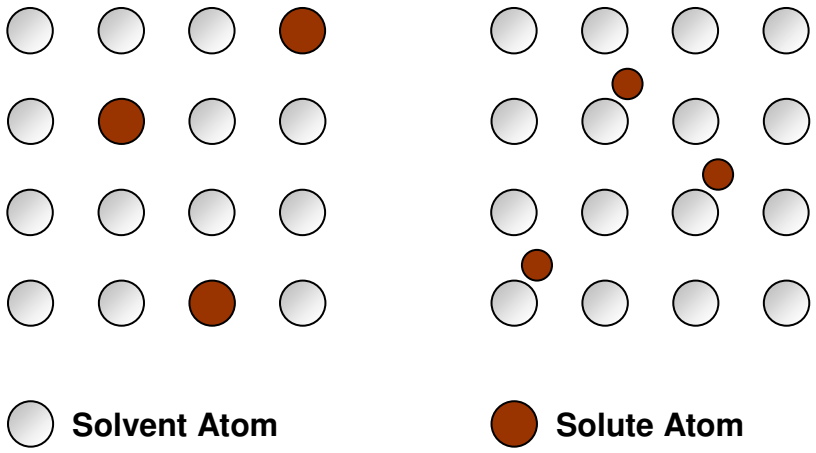

Figure 2.11. (a) Substitutional solid solution hardening, (b) Interstitial solid solution hardening [6].

The martensitic phase is a distorted body centered cubic (bcc) or body centered tetragonal (bct) structure and is created when interstitial carbon is retained in the matrix during iron's transition from the austenite phase to ferrite phase. This transformation is shown in Figure 2.12. Austenite is a face centered cubic structure. Due to the arrangement of atoms, an fcc structure has more interstitial space than a bcc structure and, as a result, has higher carbon solubility than ferrite, a body centered cubic structure. Under slow cooling, the transition from austenite to ferrite occurs slowly and carbon is able to precipitate at grain boundaries to form iron carbides. Under rapid cooling, carbon will not be able to diffuse rapidly enough out of the matrix and becomes trapped, distorting the ferrite.

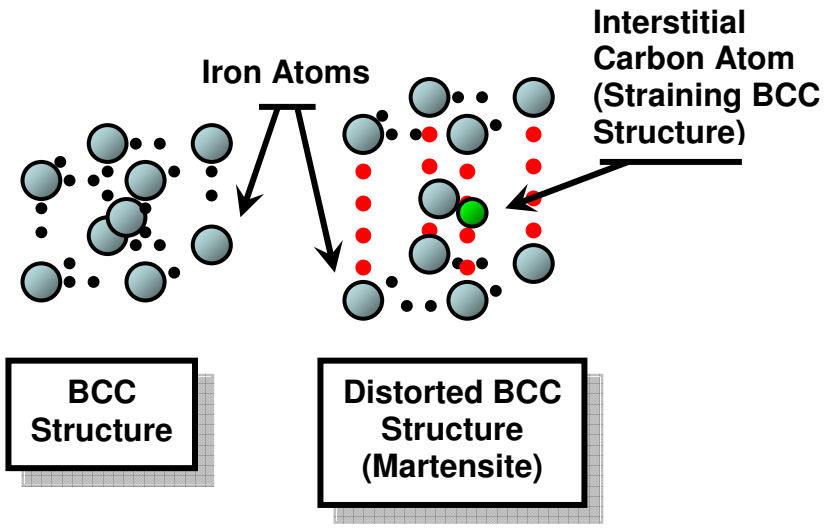

Figure 2.12. Strengthening of martensite.

Due to the shearing effect of the carbon remaining in solution, dislocations are formed within the martensitic structure in high concentrations. Due to the high density, dislocations will begin to impede the movement of other dislocations and in effect tangle. This "tangling" will give the steel high strength but will also reduce ductility resulting in a brittle material.

At high temperature, dislocations will gain enough energy to untangle and begin to glide freely. This causes an abrupt reduction in the steels strength and allows the material to begin to creep. The high temperature also increases the energy of trapped interstitial atoms and causes them to begin to diffuse out into the matrix to low energy areas such as grain boundaries. At low energy points in the metal, the precipitated carbon will pull other elements out of solution, recovering the steel and creating large carbides within the grain boundaries. This process is shown in Figure 2.13.

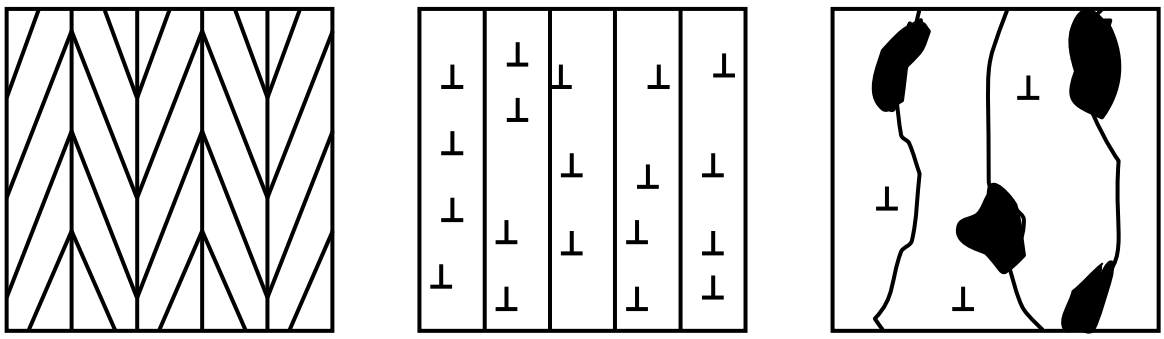

Figure 2.13. (a) Lathe martenstic structure (b) tempered martensite, large numbers of dislocations are being pinned by small MX precipitates in the matrix (c) crept microstructure, large course carbides are forming in grain boundaries leading to a destabilization [2].

The newly formed carbides are not as effective as smaller MX carbides or interstitial atoms in preventing dislocation movement. As a result, a martensitic microstructure will not be as effective in high temperature, creep environments as an aged microstructure.

In order to control the recovery of a martenstic steel and create a stable microstructure at high temperatures, carbon and other unstable atoms are precipitated by a controlled method such as a specific heat treatment. Typically, in order to do this, martensitic steel

is elevated to a temperature higher than what it was intended for in service, but below the austenitic transformation point. At this temperature it is then held for a period of time to allow a new microstructure to develop. During this time, retained carbon gains energy and diffuses into former austenite grain boundaries and sub-grain boundaries to form iron carbide (Fe_3C). Due to carbon's high affinity to metal elements, its precipitation will also draw out solute atoms to create metal carbides. By tempering at a very high temperature, carbides will become stable and resistant to further precipitation at lower temperatures during service. A tempered and aged martensitic microstructure is illustrated in Figure 2.14. Outlined in red in Figure 2.14, small carbides in the grain act as effective dislocation blockers, increasing the creep strength of the material. The resulting microstructure is a weakened martensite due to the removal of carbon, but will still remain stronger than ferrite.

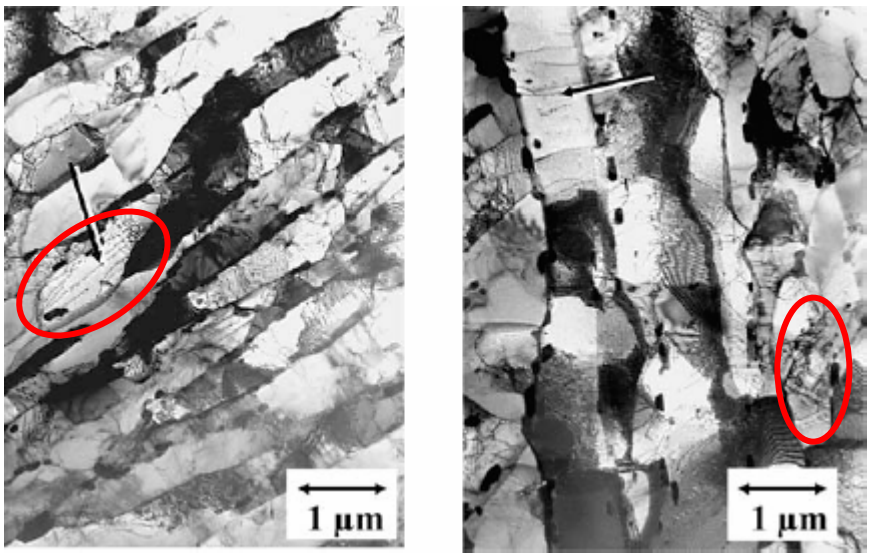

Figure 2.14. TEM image of tempered and aged martensite structure of a 12% Cr (a) and 9% Cr (b) martenstic steel, note high number of pinned dislocations in grain boundaries (outlined in red) [20].

During tempering, dislocations gain energy and conglomerate around emerging precipitates to form highly developed sub grain boundaries. Emerging structures are usually MX and M_2X phase carbides. In 12%CrMoVW steel, carbides are typically made up of refractory metals such as Mo, V, and W, but in stainless steels such as ASTM A437 Grade B4B, the carbon will also draw out chromium to create larger

$Cr_{23}C_6$ carbides [21]. These carbides are much larger than MX phases and are not as effective in preventing dislocation movement. In low chromium steel such as ASTM A437 Grade B4B, the creation of large chromium rich carbides will cause a chromium deficient area in the matrix around grain boundaries. This will reduce the corrosion resistance of the steel and may lead to inter-granular corrosion [22]. The difference in the dislocation pinning abilities of large chromium carbides and small MX carbides can be seen in Figures 2.15 and 2.16. In Figure 2.15, dislocations are effectively stopped within the grain by small precipitates, whereas in Figure 2.16 larger chromium carbides have grown in the grain boundaries allowing free dislocation movement through out the steel.

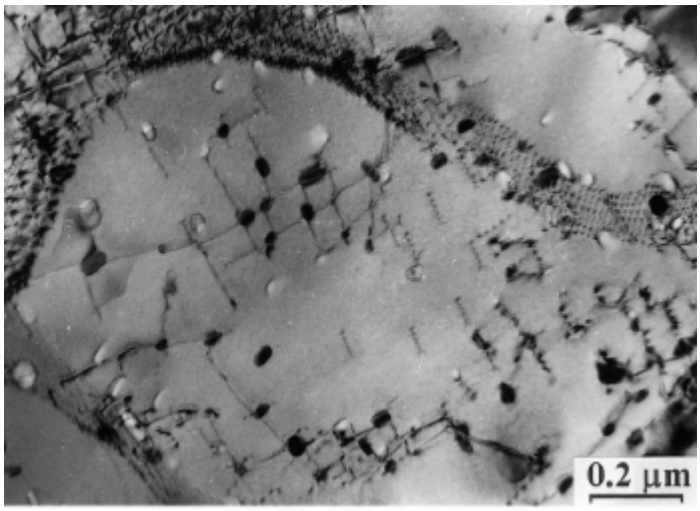

Figure 2.15. TEM image of fine MX, M_2X carbides within 9% Cr martensitic steel, effectively blocking dislocations within the grain [23].

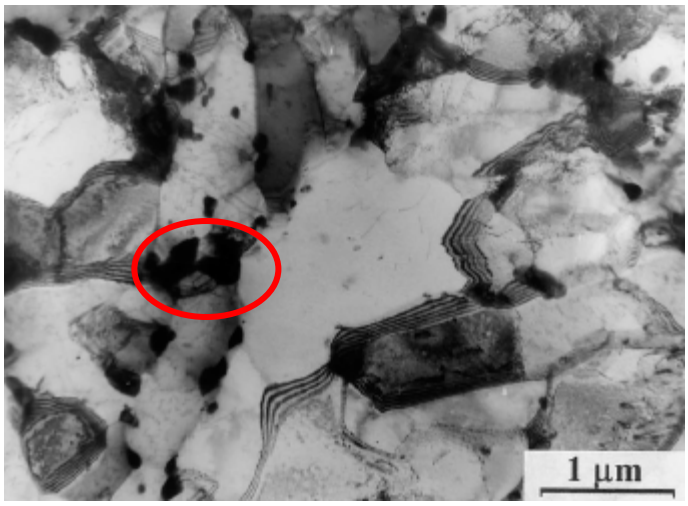

Figure 2.16. TEM image of 9% Cr martensitic steel with larger $Cr_{23}C_6$ forming in sub grain boundaries (outlined in red) [23].

2.2.3 Martensitic Development

After tempering, high alloy martensitic steel can be expected to have a large agglomeration of $M_{23}C_6$ carbides in the sub grain boundaries with a fine dispersion of MX carbides in the matrix [21]. The MX carbides, due to their size (approximately 5-10 nm) are effective dislocation blockers, and are responsible for steel's good creep strength.

ASTM A437 Grade B4B contains a relatively high amount of carbon and chromium (0.2 % wt. C and 11.5 % wt. Cr.). Due to the high affinity between carbon and chromium, it is expected that the large $M_{23}C_6$ carbides found at the grain boundaries are to be comprised mainly of chromium drawn out of solution in the surrounding areas [24]. With the high percentage of other precipitate-stabilizing metals such as vanadium and tungsten, larger structures should also have some of these elements in it, especially when high tempering temperatures are used. This will help stabilize these structures and prevent a recovery of the grain boundaries during service.

Fine MX particles are expected to comprise molybdenum, vanadium and tungsten. Expected structures are Mo_2C, VC, V_2C and WC, W_2C. These structures are not stable

and will coarsen during the steel's service eventually reducing the creep resistance of the steel [25, 26].

As the steel ages, intermetallics will form in the matrix, such as Fe_2W or Fe_3Mo. The phases are initially good creep inhibitors but, over time, will tend to coarsen at a much higher rate than the large $M_{23}C_6$ carbides and lead to an eventual breakdown in grain boundaries [24, 27]. The initial coarsening of these carbides will cause the creep rate of the steel to decrease to a minimum, when the carbides become too large to prevent dislocation movement. The coarsening of these particles beyond their effective size has been suggested to be the cause of the increase in creep rate, indicating the entry into third stage of creep [5, 19].

3.0 Experimental Procedure

3.1 Carpenters 636

ASTM A437 Grade B4B steel is a standard for steels used for high temperature bolting applications and is commercially unavailable as a product; however, many foundries will make steels that conform to the ASTM standard. Carpenters 636 is one such steel guaranteed to conform to, if not exceed the ASTM standard for ASTM A437 Grade B4B steel. It is also readily available in small lots as it is commonly stocked by vendors. All Carpenters 636 was purchased directly from Carpenters by HCI. A comparison between the ASTM Grade B4B steel and the Hitachi 12%CrMoVW steel is shown in Table 3.1. The true chemical composition of the lot of Carpenters 636 used in the study is also included in the table.

Both the ASTM and Hitachi have similar requirements for chemistry with the specific lot of Carpenters 636 used meeting both practices. Because of this Carpenters 636 was chosen to represent the ASTM grade due to its availability and adherence to the ASTM standard.

Despite meeting both the ASTM and Hitachi stands, tolerances in both are low enough that slight changes in the trace elements, such as titanium, a grain refining additive, can cause large changes in the creep characteristics of the steel. This is why creep testing is necessary to qualify a new material for use.

The low concentration of nickel specified in the ASTM specification may have the effect of lowering the hardenability of the steel due to the large amount of tungsten and

vanadium present in the steel. However, since the ASTM standard demands that the steel be fully austenitized and oil quenched to develop a fully martensitic microstructure, the difference in hardenability due to nickel content should have very little effect on the final properties of the steel.

Table 3.1. Comparison of the ASTM [28] Standard to the Hitachi standard and the measured chemical composition of Carpenters 636.

	Chemical Composition by % wt.		
Element	**ASTM A437 Grade B4B**	**Carpenters 636 (As Measured)**	**Hitachi 12%CrMoVW**
C	0.20-0.25	0.21	0.20-0.25
Cr	11.0-12.5	11.82	11.0-12.5
Mn	0.50-1.00	0.73	0.50-0.90
Mo	0.90-1.25	1.09	0.90-1.25
V	0.20-0.30	0.22	0.20-0.30
W	0.90-1.25	1.03	0.90-1.25
P	0.025 max	0.014	0.025 max
S	0.025 max	0.001	0.025 max
Si	0.20-0.50	0.33	0.50 max
Ni	0.50-1.00	0.73	0.50-0.90
Al	0.05 max	Nil	0.04 max
Ti	0.05 max	Nil	0.03 max
Sn	0.04 max	Nil	0.20 max

In order to create a uniform martensitic microstructure, the steel is first heated to 1025 to 1050ºC and then liquid quenched below 316 ºC. To then create a stable microstrucutre of tempered martensite and the fine precipitates required for good creep resistance, the steel is then tempered 55ºC above the intended operating temperature, but no less then 620ºC. This is performed in an air atmosphere for a minimum of 2 hours [28]. For the purposes of this study the Carpenters 636 was tempered at 620ºC. This was performed by the manufacturer with all steel used in the study coming heat treated from the

supplier. In order to test the as-received characteristics of the material prepared for service, the steel was not re-heat treated and all testing was performed with the same heat treatment regardless of test temperature.

Surface finish can have a profound effect on the creep life of the steel and the presence of localized stress raisers within the gauge length can act as initiation points for fracture or localized corrosion leading to premature failure. To ensure homogenous samples for testing, samples were machined to the final test standard from 28.5 mm heat treated bar stock. During machining, care was taken so that the microstructure was not altered by overheating or deformed by permanent strain in the sample's surface. Samples were then polished using 600 grit sand-paper to achieve 15 μm finish.

3.2 Experimental Setup for Creep Tests

A schematic layout of the University of Saskatchewan's creep laboratory is shown in Figure 3.1. The laboratory consists of ten SATEC creep frames controlled by a central pc using a LinkPac digital interface. The interface is capable of monitoring equipment status, as well as the temperature and strain output from each machine. Data may be also sent to a strip chart recorder to make a hard copy for redundancy. Each machine is also equipped with visual temperature displays, an event timer, and a Mitoyu dial-gauge extensometer for manual sampling. During a power failure the machines can run on battery backup for three hours without powering down or experiencing a significant drop in test temperature.

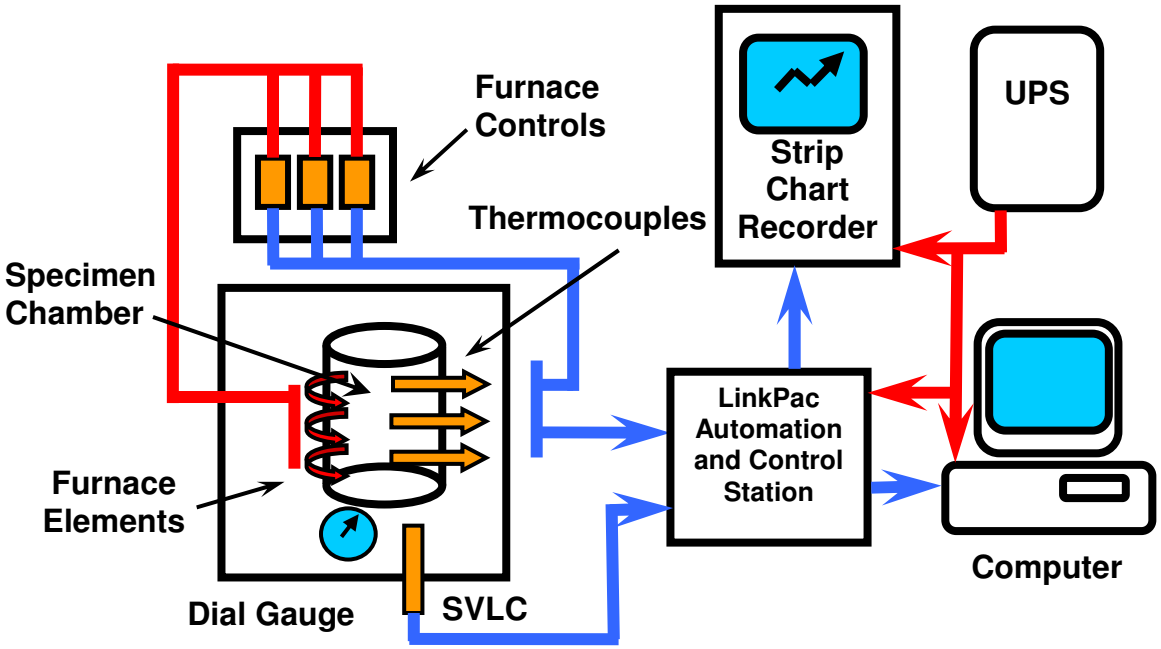

Figure 3.1. Creep laboratory setup.

3.2.1 Creep Frames

As previously stated, testing was performed using ten SATEC creep frames, half of which are equipped with extensometer frames capable of real time strain measurement. A typical frame is shown in Figure 3.2 followed by a schematic representation of the load train in Figure 3.3.

The SATEC frame makes use of static loading with a 10:1 mechanical advantage on the load arm. Since the frame makes use of static weights, the mechanical advantage allows for a large range of stresses to be applied to the sample. As summary of testing that includes the range of creep stress tested at is shown in Section 3.3. This makes it possible for comparative testing of very strong or weak materials while maintaining consistent sample geometry. A self-levelling, double-edged fulcrum is employed in the setup to ensure that constant loading is provided throughout the test, regardless of the amount of strain a test may generate. Round bar specimens were used machined according to ASTM Standard E-139-96. These are discussed in more detail in Section 3.2.4.

Figure 3.2. SATEC creep frames.

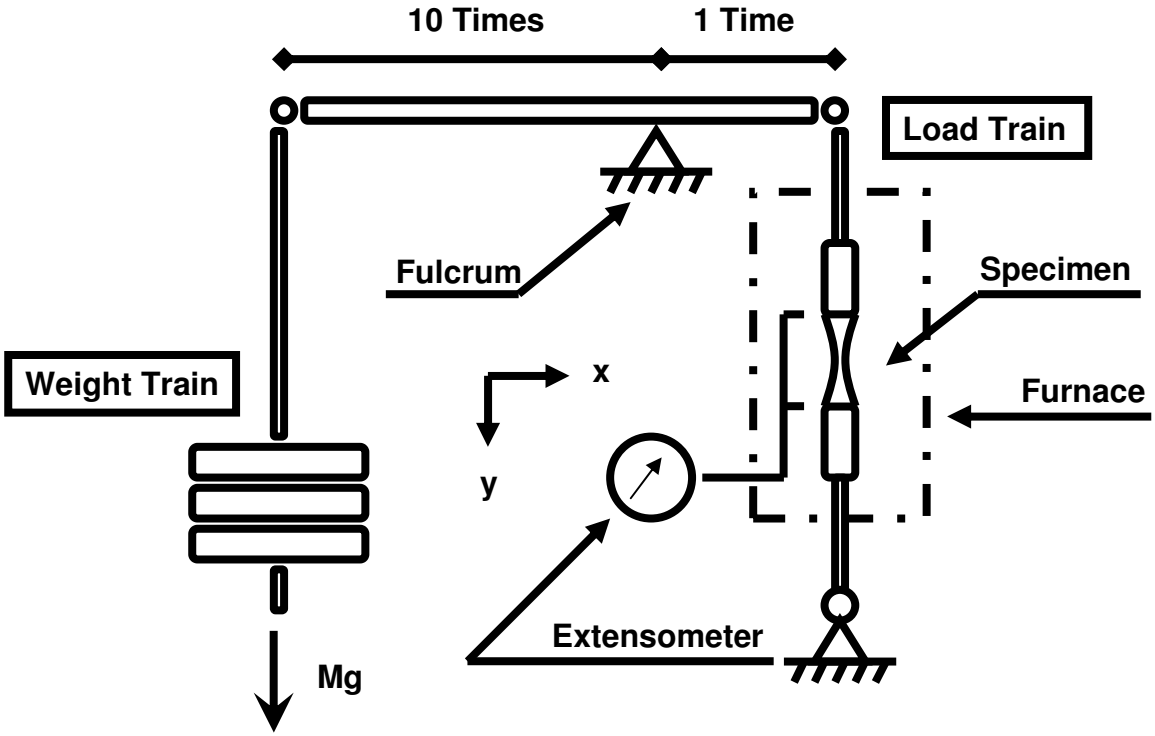

Figure 3.3. Creep frame schematic.

3.2.2 Strain Measurement

To measure strain, a single Super Linear Variable Capacitor (SLVC) was attached to the extensometer frame and was remotely monitored by the main computer. Data were sampled every 90 seconds, but were only written if there was a significant change in strain. This is to attenuate the data and reduce the size of the data files. To complement the automated sampling, a Mitoyu dial gauge extensometer was used to take manual measurements of strain. The extensometer frame (shown in Figure 3.4) was directly attached to the gauge length, and provided a 1:1 ratio of sample strain, to extensometer frame extension. The dial gauge is rated at +/- 1µm through out the range with the SVLC having an error of 0.1%, this equates to a maximum error of approximately +/- 9 µm. Compared to the +/- 0.1 mm error in measuring the gauge length using a digital calliper, the error in measuring displacement is significantly lower. In total there is a maximum error of 0.1 µm in strain measurement largely due to error in measuring the specimen's dimensions.

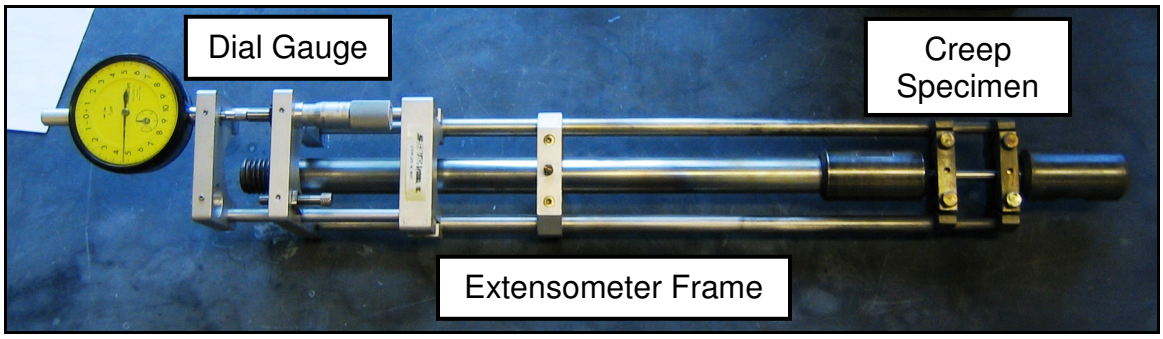

Figure 3.4. Extensometer frame with dial gauge and sample.

3.2.3 Temperature Control

The temperature is controlled using SATEC model 847 proportional-integral-differential (PID) controllers. Each controller reads from a platinum-rhodium (R) type thermal couple attached to the gauge length of the sample (shown in Figure 3.5). In total, three thermocouples were used, mounted at the top, middle and bottom of the gauge length. Each thermocouple is controlled by its own SATEC controller. The controllers are then

monitored by the LinkPac PC. In the event of a thermal couple reading over or under the test temperature by more than +/- 5º, the computer will automatically shut down the test and log the error. Each PID controller is responsible for regulating one of three ceramic heating elements. Elements are mounted inside the furnace at the top, middle and bottom of the test cylinder. This configuration allows the system to provide constant temperature throughout the furnace with less than a 0.5°C variance in temperature.

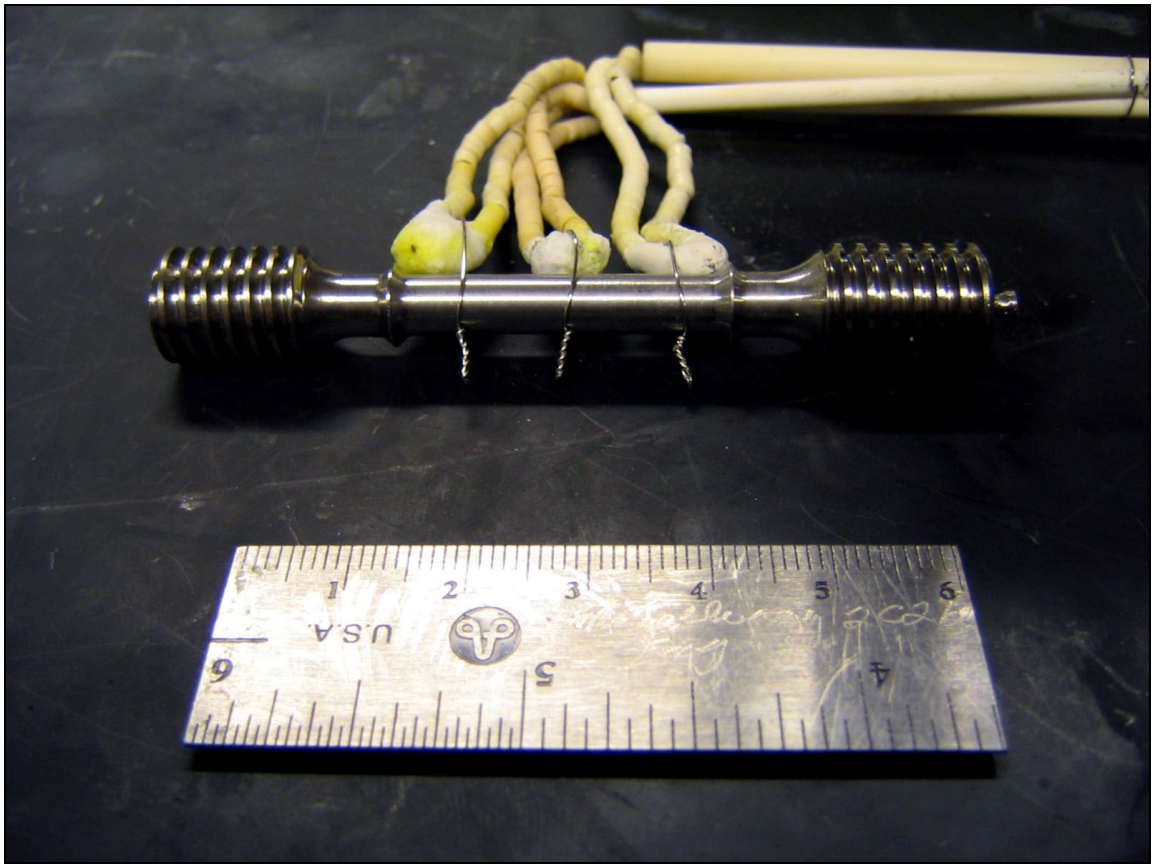

Figure 3.5. R-type thermocouples mounted on gauge areas of creep sample.

3.2.4 Creep specimens

Specimens were machined to ASTM standard E 139-96 (shown in Figure 3.6) from heat treated barstock. After machining, the samples were polished on a jewellers lathe by hand to a 15 µm finish using 600 grit silicon carbide sand-paper. The diameter of the sample was measured at six different points along the gauge length (once at the two

opposite ends and then in the middle of the reduced section). The sample was then rotated 90° and the three points measured again. Samples were rejected if there was more than a 5% standard deviation in diameter along the entire gauge length.

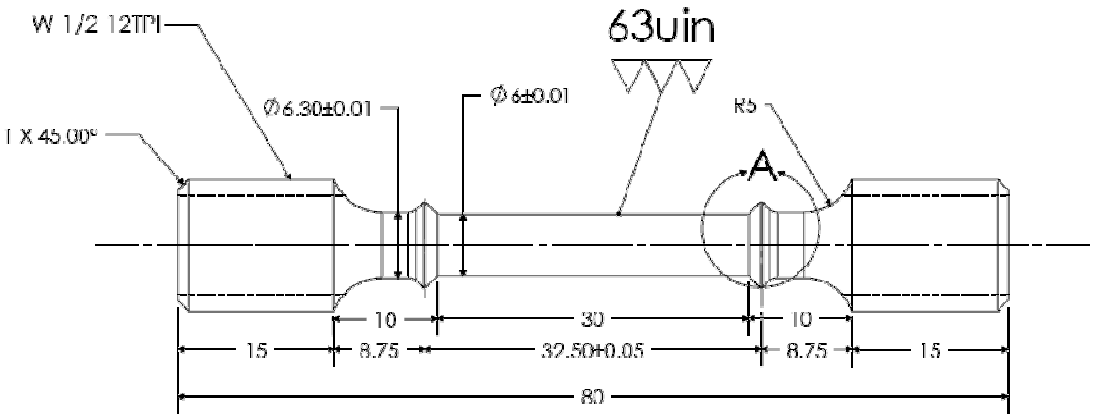

Figure 3.6. ASTM Standard E-139-96 creep test specimen specifications (dimensions in mm)[29].

3.3 Creep Testing

By creep testing, one tries to infer the long term time-dependant deformation characteristics of a material by observing its behaviour under conditions that are similar to those that it would be exposed to in service but that will accelerate the time-to-rupture. Studies are carried out on the material at temperatures and stress-levels that are higher than what the material would be exposed to in service in order to accelerate testing. As Figure 3.7 shows, increasing the stress and temperature in order to accelerate testing will shorten the time-to-rupture and allow for a quick test, but doing so can also greatly change the creep behaviour of a material before failing.

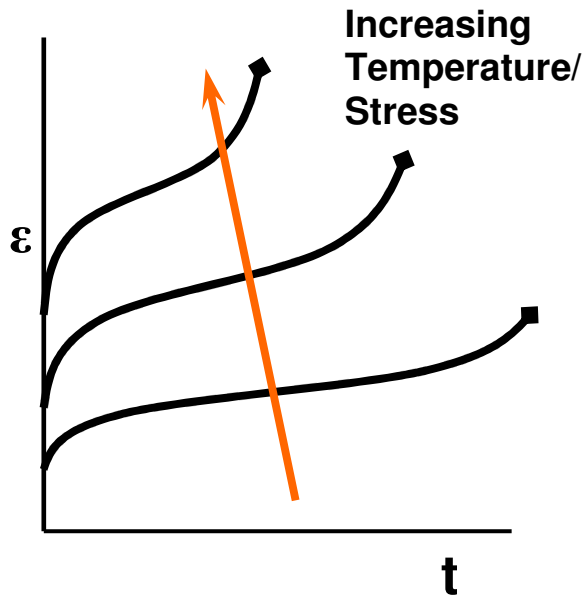

Figure 3.7. Effect of stress and temperature on creep.

By even slightly increasing the temperature and/or stress to reduce the time to failure, the dominating mechanism controlling the mode of creep may change. If this occurs, what is observed during experimentation will be very different from what the material experiences in use. As a result, creep tests are rarely accelerated more than three times the intended service life of the material. In this study, the longest test was accelerated approximately 17.5 times that of the intended service life: 10000 hrs instead of the 20+ year intended service.

To determine the range of temperatures and loading to be used in testing, the conditions that the bolts are expected to experience in service were determined. It was found that the bolts used by HCI in casing applications will be exposed to a stress of 161 MPa at a temperature of 538 ºC [1]. Using the Larson-Miller method, a testing schedule was generated around the intended service conditions. Previous isostress testing was performed on ASTM A437 Grade B4B steel by Griffin [1] and a Larson-Miller constant of 30 was determined for the steel. By using the revised constant, the accuracy of the Larson-Miller method is increased.

A schedule consisting of three sets of isothermal tests at 549 ºC, 593 ºC and 649 ºC was developed to give a range of expected creep life from 36 to 10000 hours over a range of stress. At least one creep-rupture and one creep-stress test was performed at each temperature/stress combination. A summary of the schedule is shown below in Table 3.2.

Table 3.2, Testing Matrix Based Upon Larson-Miller Predicted Time-to-Rupture

℃	32		56		180		320			560		
538	**4B §**	**9AA**	**9U**	**4C §**	**5D §**	**5J §**	**5H**		**9R §**	**9D**	**9Q**	**9F §**
	426.6	424.57	416.55	400	394.3	394.2	394.6		386.71	381.99	396.31	396.31
	18.37	83	79.88	111.05	185.36	214.97	234.49		1103	608.89	407.73	655.03
	DM	AMH	AMH	DM	DM	DM	DM		AMH	DM	AMH	DM
593	**9T §**	**9O**	**9K**	**9V §**	**4E**	**9J**	**4F**	**9M**	**9X §**	**4I §**		
	323.86	340.44	324.28	316.37	305.8	347.14	276.7	259.25	300.29	260.3		
	31.46	19.87	49.33	41	134.14	166.66	299.42	394.05	105	524.85		
	AMH	AMH	DM	AMH	DM	DM	DM	AMH	AMH	DM		
649	**5I §**	**9L**	**5A**	**9Y**	**4J §**	**5E §**	**9AM**		**9P §**	**9H §**	**9Z**	
	181.7	184.55	159.6	198.78	139.7	139.9	125.8		129.63	121.34	120.93	
	35.98	43.88	76.33	43.92	155.56	173.95			316	724	498.18	
	DM	AMH	DM	AMH	DM	DM	AMH		AMH	DM	AMH	

℃	1000		1800			3200			5600		10000		
538	**4D §**	**9G §**	**4K**	**9AI §**		**5B §**	**9AL**		**9AF §**	**9AN**	**9AE/9AG §**	**9AH**	
	370.6	381.47	348.7	350.49		330.8	330.9		315.27	315.49	301.8/304.9	298.966	
	797.63	730.14	1617	1101		3932			3676*	5335.92	19219.64	13747.8	
	DM	DM	DM	AMH		DM	AMH		AMH	AMH	AMH	AMH	
593	**4G**		**9E §**	**6A**	**4H**	**6I**	**6J**	**6K §**	**5G**		**5L §**	**6L**	**6N**
	220.8		208.63	198	197.6	161	161	161	139.9		130.04	130.04	130.04
	1277		2343	1932	2316	3854	3866	4230	4978		10358.2	12056	9449.01
	DM		DM	DM	DM	DM	DM	DM	DM		DM	DM	DM
649			**9C**	**5C**	**5F**	**9S**			**9W §**	**9AD**	**4M §**	**9AB**	
			107.88	93.5	80.3	77.69			68.96	300	50.2	60.16	
			1415	2082	2128	4236			4236	5622.35	14221	16859.52	
			DM	DM	DM	AMH			AMH	AMH	DM	AMH	

Key:

4M	Specimen (**§** Indicates Creep-Strain Test)
50.2	Stress (MPa)
14221	Time to Rupture (hrs)
AMH	Person Responsible for Test. AMH: Andrew Hamilton DM: Darryl McCullough

3.4 Hardness Measurements

Samples from completed tests were used for hardness measurements. Hardness testing was performed using a Mitoyu Vickers Microhardness tester. A 300 g load and twelve second resident time was used in all tests. Points were taken a sample's crept gauge length (where high stress was apparent) and outside the reduced section. The area outside the reduced section can be assumed to be relatively unaffected by creep stress and the development of the microstructure should be primarily due to increase in energy due to aging at an elevated temperature. Samples were cut longitudinally along the gauge length and polished to 1 µm surface finish. Hardness measurements were traversed across the radius of the sample at three separate locations orientated longitudinally from the fractured end.

3.5 Transmission Electron Microscopy

As-recieved samples of heat treated ASTM A437 Grade B4B steel were compared to long term tests to observe changes in microstructure. Samples used for TEM analysis first had the fracture area removed and the remaining gauge length sectioned above the necked area. This was done to ensure that the observed microstructure did not exhibit the effects of intensified localized stress caused during necking. Samples were sectioned into 0.5 mm thick disks using a low speed diamond cutter. The sectioned areas were then mounted on a polished steel base and thinned to a thickness of 20 µm using consecutively finer grit sandpaper, beginning with a 320 grit paper and ending with a 600 grit paper. Sandpaper was affixed to a glass plate to ensure even polishing. Both sides of the sample were thinned to ensure that both sides of the disk were homogenous. The thinned sections were then punched into 3 mm diameter disks and further reduced using a Struers electropolishing machine. An etchant composed of 10 vol. % Perchloric acid, 20 vol. % Glycerol and 70 vol. % Ethanol was used in the polishing machine and a potential of 20 VDC was applied across the sample. The electropolishing method is outlined by the flow chart in Figure 3.8. Cooled etchant was jetted onto the center of the sample from either side. At the same time, an electrical potential was applied to the

sample to make it anodic. This was done to allow an even removal of material from the sample by the etchant. Eventually a depression was formed on either side of the sample that grew until the two depressions met and created a hole on the order of one or two µm. At this point, light was able to pass through the hole to trigger a photogate switch, stopping the process. The resulting area around the hole was thin enough (2-5 µm thick) for electrons to pass through during transmission election microscopy and create an image of the steel's microstructure

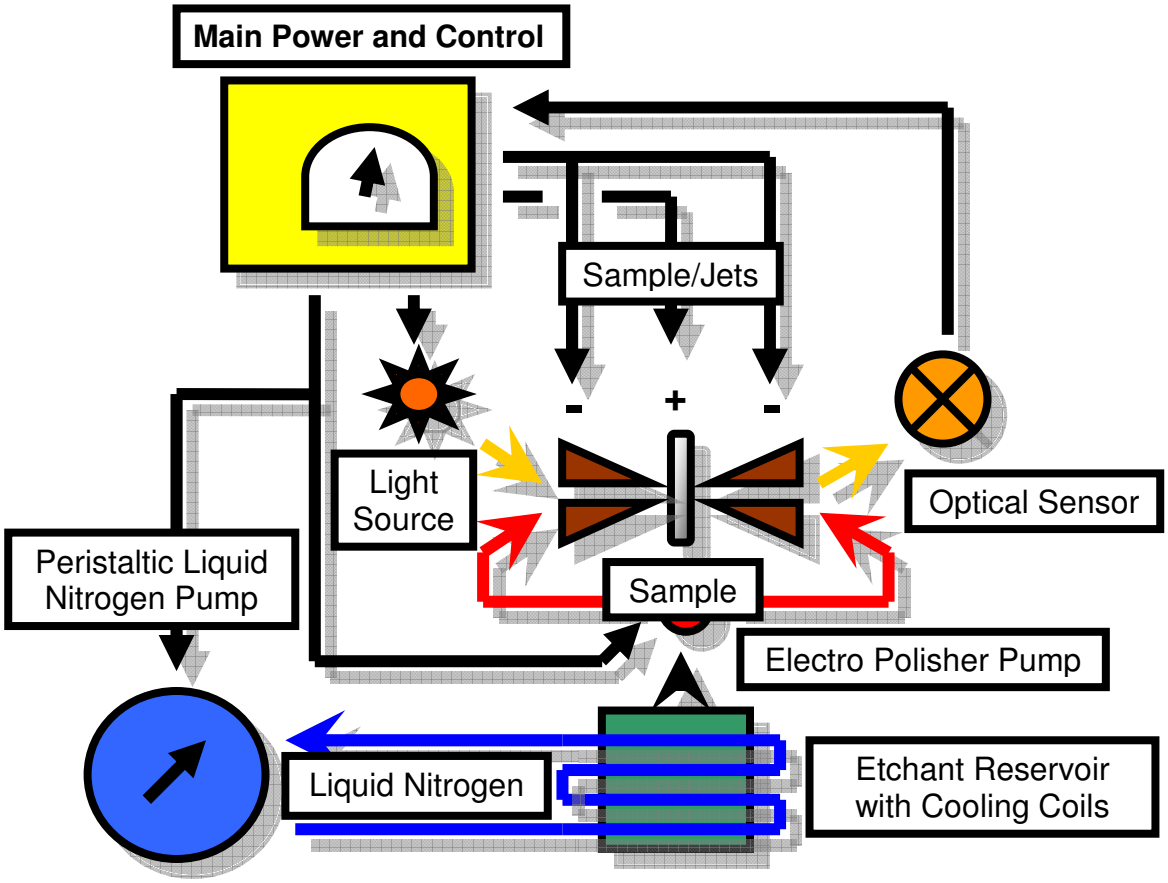

Figure 3.8. The electro-polishing process.

During electron bombardment in the TEM, the energy transferred from electrons will cause the sample to become even more magnetic. This makes TEM analysis very difficult as the electron beam can curve due to the magnetic interference. This will create a severe distortion of the image and cause a false reading in the energy dispersive spectrometer (EDS). To counter this, a demagnetizer was used in producing samples and was effective in reducing the magnetic interference. The demagnetizing process is

shown in Figure 3.9. By moving the sample through a magnetic field, the magnetic iron phase aligns itself with the field, negating its own magnetic field. The end result is a slightly less magnetic sample, but severe mechanical damage can be caused to the sample damaging the thin area around the hole.

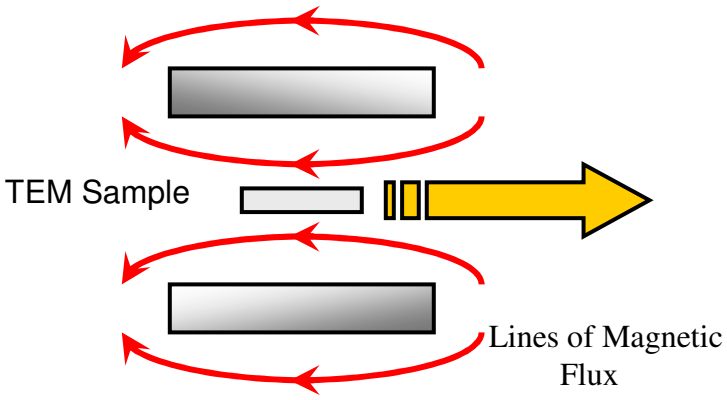

Figure 3.9. Effect of demagnetising.

A Hitachi HF-2200 field emission scanning, transmission election microscope (STEM), shown in Figure 3.10, was used for imaging and a Cambridge 7480 Energy dispersive X-rayspectrometer (EDS) was used for phase identification. Pictures were manually taken using an eight frame stitch digital camera with a 17.4X lens magnification. This setup is capable of resolving images up to approximately 3 million times magnification. After a picture was taken, the electron beam spot size was focused upon phases to be studied and the microstructure manually mapped. Due to the nature of the Cambridge EDS, light elements, such as carbon, could not be accurately analyzed.

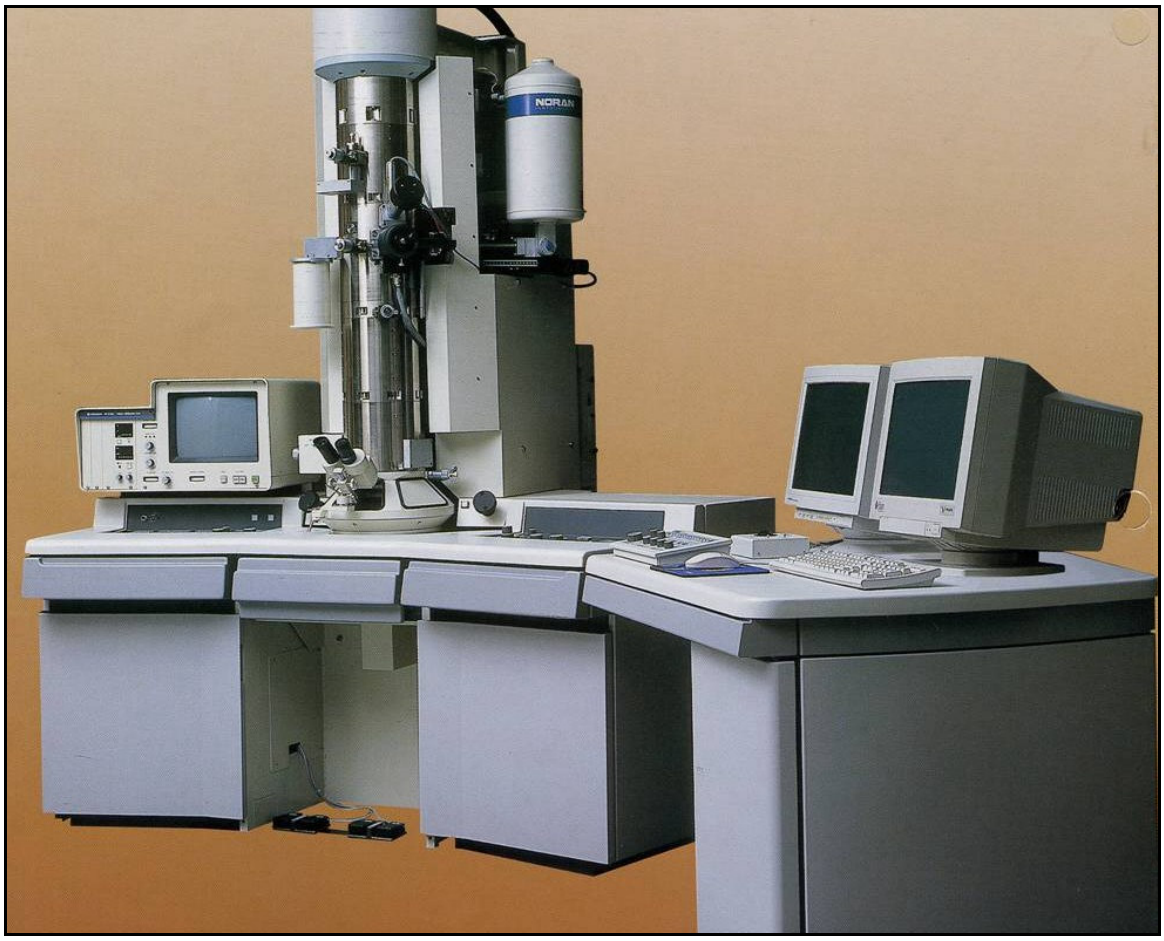

Figure 3.10. Hitachi HF-2200 field emission scanning transmission electron microscope [30].

4.0 Results and Discussion

4.1 ASTM A437 Grade B4B Creep Results

4.1.1 Introduction

Testing of ASTM A437 Grade B4B steel was first begun by Shane Griffin [1] with a series of isostrain creep-rupture tests. This was done as part of his research to characterize three hardenable steels. The Larson-Miller and Goldhoff-Sherby methods of characterizing creep life were then used to characterize the data and determine if one of the methods could be used to predict creep life for ASTM A437 Grade B4B steel. Using a modified Larson-Miller constant of 30, it was determined that the Larson-Miller method of prediction best characterized the steel. Utilizing the Larson-Miller method, a testing schedule was developed to further characterize ASTM A437 Grade B4B steel and testing continued under McCullough [2].

4.1.2 Larson-Miller Analysis

The Larson-Miller plot, shown in Figure 4.1, was generated using time-to-rupture data from tests performed on ASTM A437 Grade B4B steel. The intended service conditions for the steel is a constant temperature of 538˚C, at a stress of 128 or 161 MPa. From previous work, the Larson-Miller constant for ASTM A437 Grade B4Bsteel was determined to be 30.

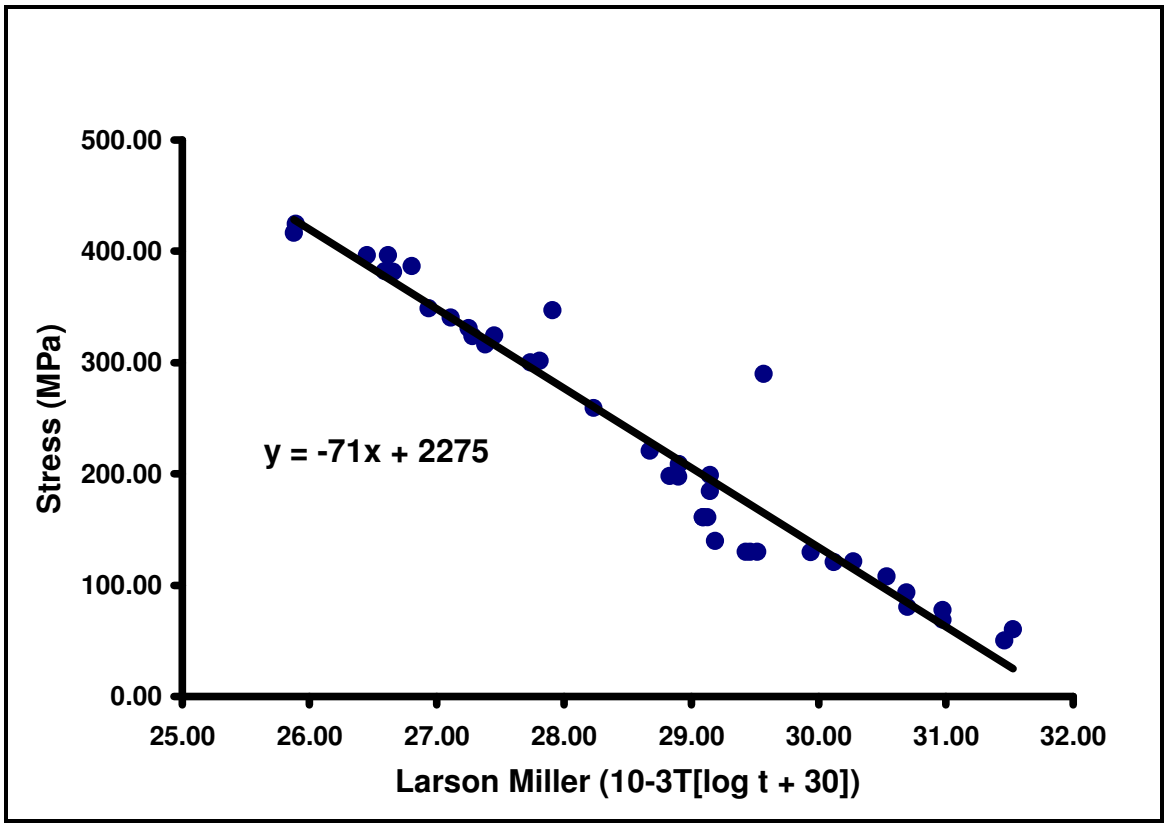

Figure 4.1. Larson-Miller plot for ASTM A437 Grade B4B steel.

When examining the plot, the Larson-Miller method shows good agreement with the data data, and a linear trend can be observed. Since the Larson-Miller method assumes that diffusion is the primary mode of creep, the good agreement suggests that the samples tested crept under this single mechanism. The consistency in data generated at different stress levels also suggests that the same mechanism is active for the low temperature, high stress tests as for lower stress tests. This means that the Larson-Miller method of prediction should remain valid for ASTM A437 Grade B4B steel outside the parameters used in this study.

4.1.3 Time to Rupture

Figure 4.2 is a plot of time-to-rupture for ASTM A436 Grade B4B steel. The time-to-rupture is plotted with respect to creep-stress for each of the three temperatures used in

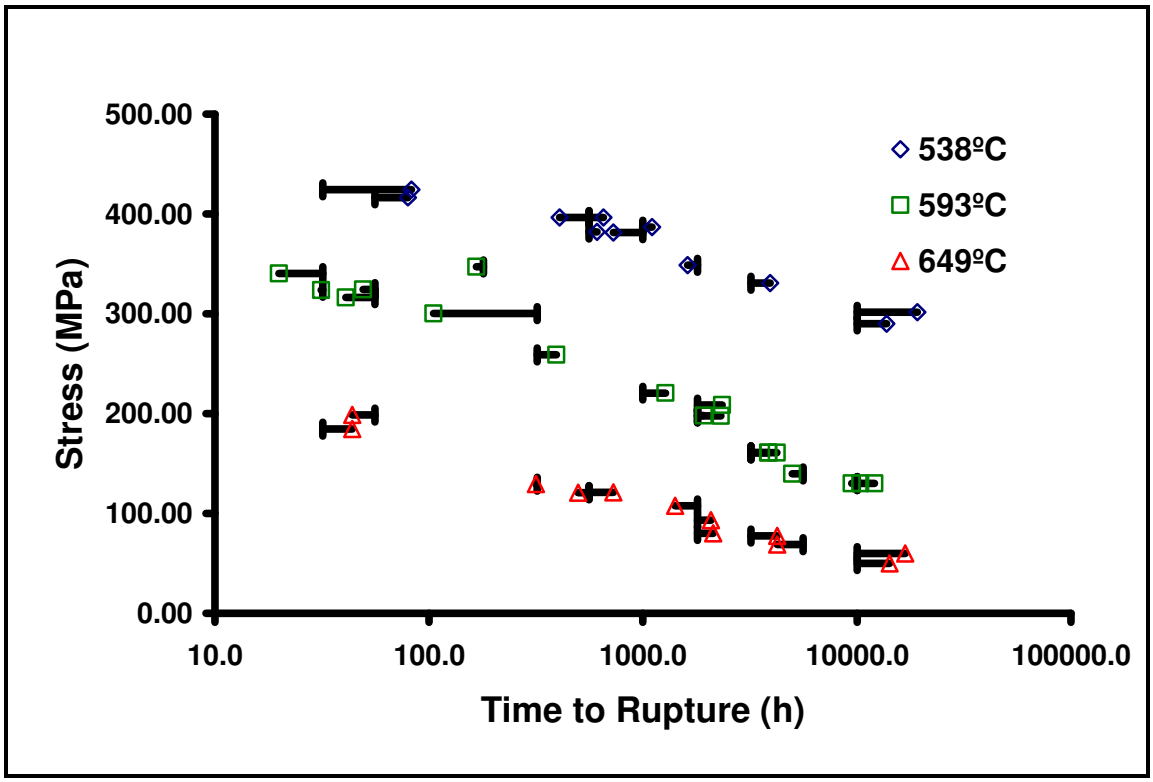

Figure 4.2. Plotted time-to-rupture of ASTM A437 Grade B4B steel at the three test temperatures of 538ºC, 593 ºC and 649 ºC.

testing. The error bars indicate the theoretical time to rupture calculated using the Larson-Miller method.

As the test conditions tended to one extreme; high temperature/low stress or low temperature/high stress. The error in predicting creep life appeared to increase. As the time to rupture increased, the error tended to be conservative. This is to be expected, as increasing stress will cause mechanisms such as dislocation creep to become more prominent instead of pure diffusion creep. Decreasing the temperature will also cause dislocation creep and grain boundary sliding to become more prominent. Since the Larson-Miller method only takes into account diffusion creep, it is unable to accurately predict the life of a component in extreme service conditions. The intended service stress is very low compared to the stress level the steel was tested at; therefore creep should be primarily due to diffusion, with stress effects not becoming as dominant as the short term tests. Because of this, Larson-Miller should be accurate in predicting creep life for ASTM A437 Grade B4B in service.

4.1.4 Creep Plots

ASTM A437 Grade B4B showed similar creep development at all conditions tested. Testing indicated that ASTM A437 Grade B4B undergoes a very short, almost non-existent primary stage followed by a well defined secondary stage. This is shown in Figure 4.3, a stress-strain plot generated from creep-strain test 9AI. Because the secondary stage creep dominated the creep life, it can be used to characterize the steel's creep behaviour. A summary of the time spend in each stage of creep for the creep-strain tests is shown in Table 4.1. ASTM A437 Grade B4B reached a minimum creep strain rate at 8-9% of its life, which ended approximately at 90% into its life where the strain rate begins to rapidly increase. The beginning and end of this period corresponds to approximately 5% and 30% of the final total strain, respectively. From the data, it appears that the start and end of secondary stage does not vary in relationship to test life, temperature or stress. It is thought that entry into second stage creep is based upon the retardation of dislocation movement due to strain hardening and entanglement of new dislocations; while the exit of second stage is attributed to the formation of micro-fractures, necking and reduction of actual area, as well as changes in the microstructure. Depending on the dominance of individual creep mechanisms, the entry into third stage creep will change. The homogeneity of the data suggests that the selected range of test conditions occurred within the same dominant creep mechanism.

The tertiary stage is relatively short, generally occupying the last 10% of the test life. It is in this stage that the greatest creep strain occurs (roughly two thirds of the total creep strain). The increase in strain rate at the end of second stage creep and the subsequent transition into third stage occurred rapidly for all the tests. A transition like this is characteristic of the formation of micro fractures within the sample, leading to a reduction in area and increasing the creep stress in the sample. This also can be indicative of a significant change in microstructure. A transition like this can also be due to the coarsening of semi-stable phases that otherwise would pin and prevent dislocation movement, but also could be due to the migration of chrome out of solution to the grain boundaries, resulting in a chromium deficient matrix. A chromium

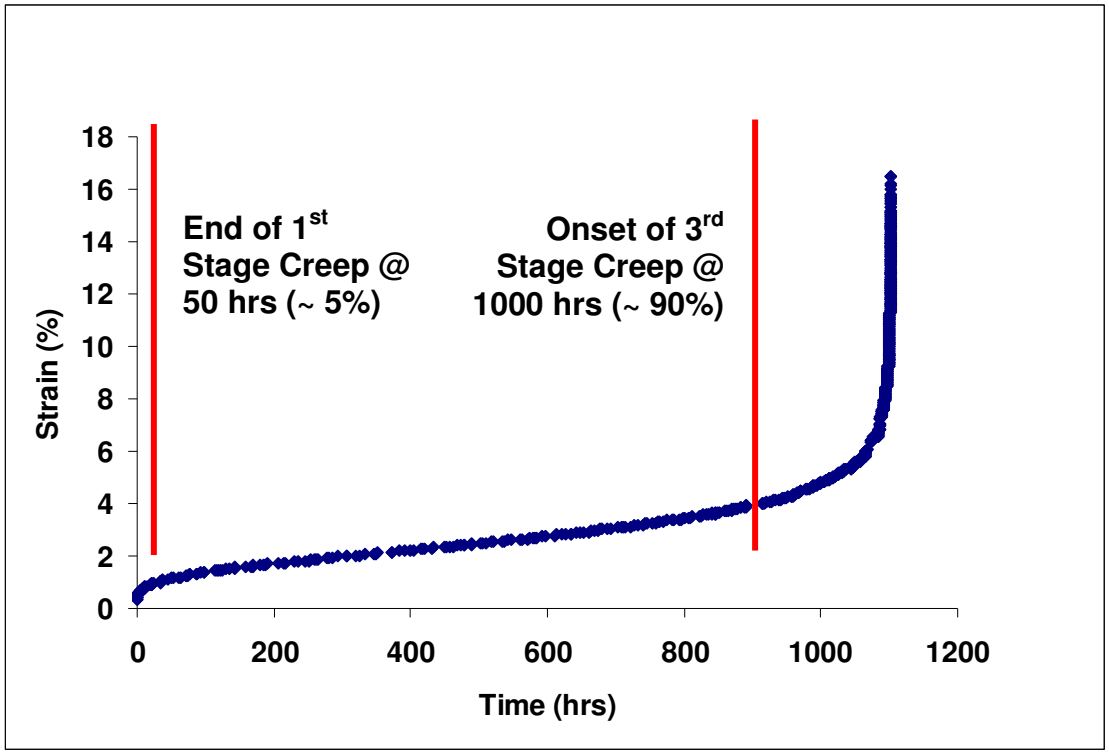

Figure 4.3. Strain-time curve for test 9AI.

deficiency around the grain boundaries will lead to inter-granular corrosion, creating micro-fractures that can be responsible for the eventual weakening and failure of the material [22].

During low stress tests, the secondary stage appears to lose its linearity and become two periods of decreasing and then increasing strain rate separated by an inflection point of minimum creep rate. This suggests that when creep conditions have a high temperature to stress ratio, different creep mechanisms begin to show dominance. Most likely in lower stress tests, dislocation density growth during work hardening is not as high. The increase in dislocation density and subsequent tangling as dislocations impede other dislocation movement is what causes the work hardening associated with the onset second stage creep. A reduction in the dislocation density would result in the slowing of the strain rate, characteristic of first stage creep, to become less localized and more drawn out.

Table 4.1, Summary of Testing

Test No.	Temperature (℃)	Creep Stress (Mpa)	Predicted Time to Rupture (hrs)	Time to Rupture (hrs)	Start of Stage 2				Start of Stage 3				Total Strain, %	Strain Rate (%/hr)
					Time (hrs)	% of Total Test Time (%)	Strain	% of total strain	Time (hrs)	% of Total Test Time (%)	Strain	% of total strain		
4B	538	426.6	32	18	3	13.6	1.5	7.4	16	87.1	7.9	38.9	20.3	0.3242
4C	538	400.0	56	111	10	9.0	1.3	6.4	100	90.0	7.3	36.0	20.3	0.0520
5D	538	394.3	180	185	18	9.7	1.3	7.2	160	86.3	5.9	32.8	18.0	0.0050
5J	538	394.2	180	215	20	9.3	1.4	8.4	190	88.4	6.0	36.1	16.6	0.0203
9F	538	396.3	560	655	50	7.6	0.7	4.1	580	88.5	3.6	20.9	17.3	0.0057
4D	538	370.6	1000	798	70	8.8	0.5	2.0	710	89.0	5.1	20.5	24.9	0.0050
9AI	538	350.5	1800	1101	90	8.2	-	-	990	89.9	5.2	16.1	32.3	0.0028
5B	538	330.8	3200	3932	300	7.6	1.1	8.9	3500	89.0	4.0	32.3	12.4	0.0070
9AG	538	304.9	10000	19219	830	4.3	0.3	2.2	17800	92.6	2.8	20.7	13.5	0.0002
9V	593	316.4	56	41	4	9.8	0.9	10.8	35	85.4	4.3	51.8	8.3	0.0795
9X	593	300.3	320	105	9	8.6	0.8	9.9	92	87.6	3.8	46.9	8.1	0.0256
4I	593	260.3	560	525	46	8.8	0.7	4.1	465	88.6	3.6	20.9	17.3	0.0040
9E	593	208.6	1800	2343	175	7.5	0.5	3.2	2040	87.1	3.7	23.7	15.6	0.0009
5I	649	181.7	32	36	3	6.9	0.6	3.4	31	86.2	5.5	31.1	17.7	0.1001
4J	649	139.7	180	156	13	8.4	0.5	2.0	135	86.8	5.1	20.5	24.9	0.0164
9P	649	129.6	320	316	22	7.0	0.2	0.8	300	94.9	7.8	37.0	21.1	0.0119
9H	649	121.3	560	724	55	7.6	0.3	1.3	620	85.6	5.5	24.7	22.3	0.0031
9W	649	69.0	5600	6921	1000	14.4	0.5	3.1	6600	95.4	7.1	44.7	15.9	0.0007
4M	649	50.2	10000	14221	-	-	-	-	10500	73.8	5.2	16.1	32.3	0.0003
					Average	**8.3**	**0.6**	**5.0**	**Average**	**88.1**	**5.2**	**30.1**		
					St. Dev.	**2.3**	**0.6**	**3.2**	**St. Dev.**	**4.5**	**1.5**	**10.7**		

4.1.5 Steady State Creep

Figure 4.4 shows the correlation between minimum strain rate and creep life for all the testing. The minimum strain rate appears to follow a direct power relationship with creep life. The fact that temperature and stress do not appear to independently affect creep life indicates that the range of testing falls within the boundaries of one dominant creep mechanism. This means that under the same test temperatures a low stress test will have the same creep characteristics as a high stress test. This further indicates that if the intended service parameters fall within the Larson-Miller curve, creep life and strain rate can be accurately determined for the steel.

When the strain rate is compared to the creep strain, a repeating exponential function dependant upon test temperature appears. This is shown in Figure 4.5.

Figure 4.5 suggests that strain rate is exponentially dependant upon creep stress and driven by a power law relationship to temperature. From this, an empirical function for minimum strain rate, based on stress and temperature, can be derived[1].

[1] The derivation of the relationship can be found in Appendix B.

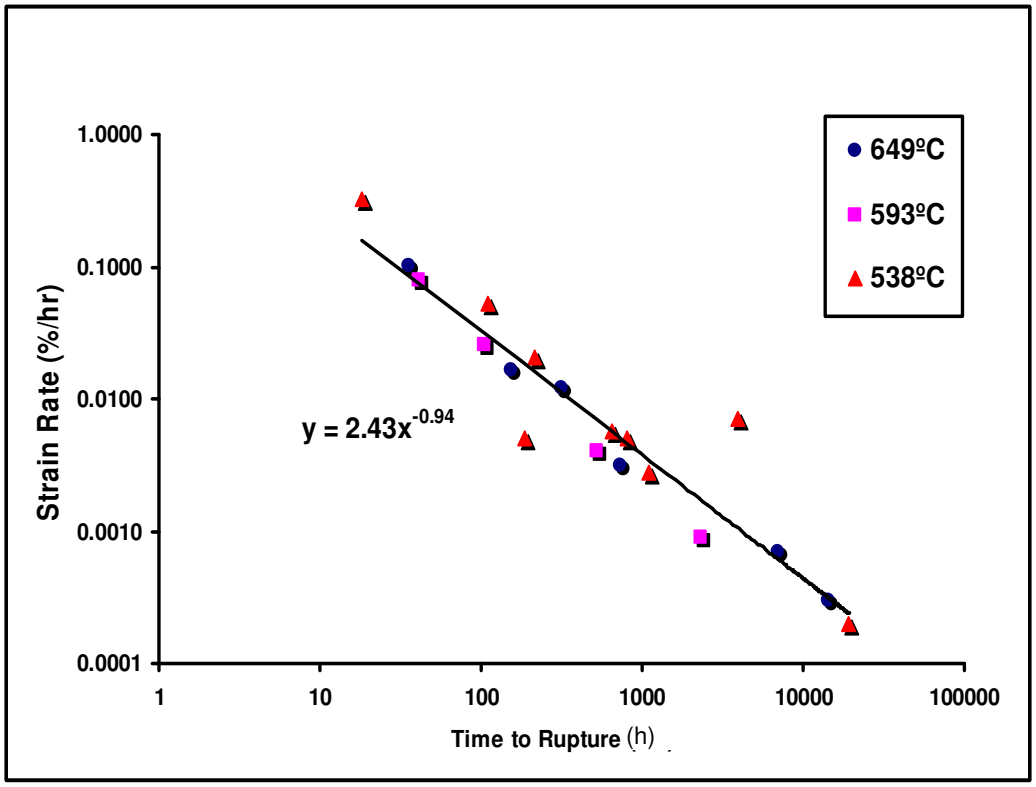

Figure 4.4. Strain rate as a function of creep life.

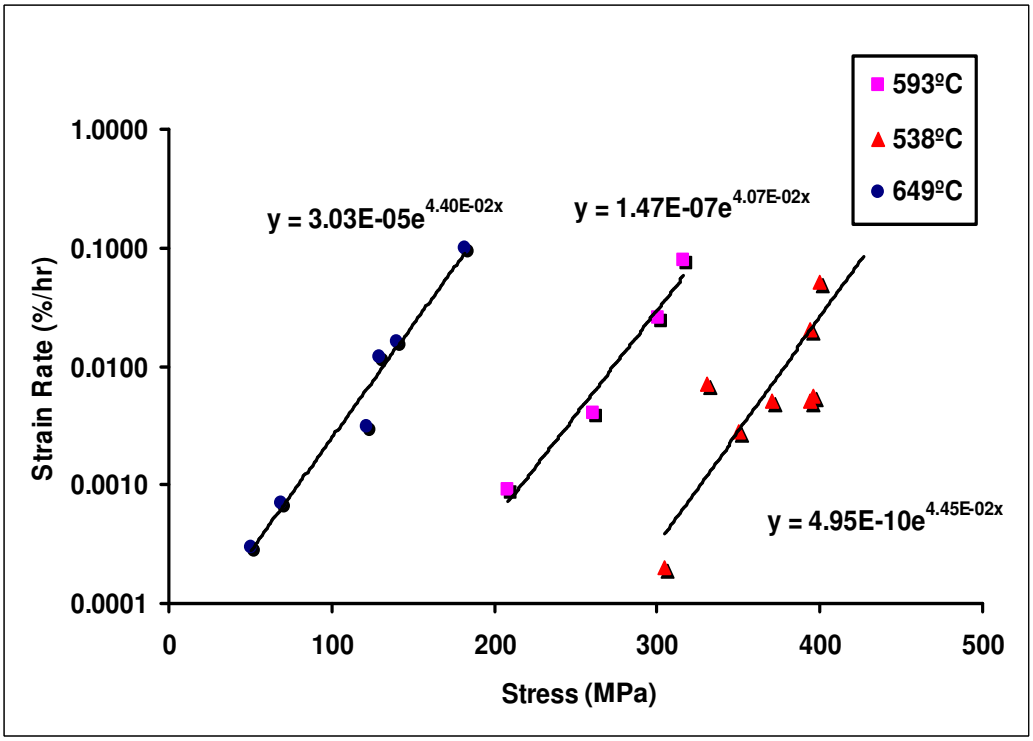

Figure 4.5. Steady state strain rate as a function of stress.

Equation 4.1 below is significant in that it suggests that creep rate does not follow the Arrhenius equation. The Arrhenius equation or power law relationship assumes that the diffusion mechanism dominates, meaning that creep is largely temperature driven. Mechanisms such as increasing dislocation density and/or changes in the microstructure are not taken into account. Equation 4.1 contradicts this.

The first part of the equation has a very high power constant of 84.6; this means that until the creep temperature approaches 1043 K (~770°C) the steady state creep rate is low and driven mainly by creep stress. As the creep temperature nears 1043 K, equation 4.1 suggests that the steady state creep rate will be completely dependant on temperature. This also suggests that at temperatures above what was used in the study, the Larson-Miller method and Equation 4.1 will become increasingly inaccurate.

Second stage creep is considered to be driven by dislocation glide competing with work hardening. Both are stress driven mechanisms; as the creep stress increases, dislocation glide will increase, exponentially driving up the steady state creep rate. At temperatures below 1043 K, diffusion is not as prevalent, but when the temperature approaches 1043 K, diffusion counters the effects of work hardening, allowing the strain rate to increase and enter the third stage creep. The resulting strain-time plots indicated large periods of second stage creep that characterize the entire creep life. This suggests that at the same temperature or at temperatures lower than what were used in this study, stress driven mechanisms dominate creep and the Larson-Miller method and Equation 4.1 will be very accurate in predicting life. Since temperature driven diffusion is not prevalent in the secondary stage, the data suggest that the recovery of the microstructure and growth of precipitates does not occur until the third stage creep

$$\dot{\varepsilon}_{SS} = \left(\frac{T}{1043}\right)^{84.6} \exp[0.044\sigma] \tag{4.1}$$

where:

$\dot{\varepsilon}_{SS}$ is the steady state creep rate

T is the absolute operating temperature in Kelvin

σ is the creep stress in MPa

4.2 Hardness Testing Results

Figure 4.6 shows a plot of the hardness of each crept sample in relation to time-to-rupture. Table 4.2 is a summary of hardness testing. Hardness measurements were taken from inside the gauge length as well as outside of the reduced section of the creep specimens in order to give an indication of an "aged" hardness were the effect of stress upon the development of the steel was relatively low.

According to the plot, the "aged" area shows a significantly higher hardness than the gauge length. The reduction in hardness is most likely due to the recovery of the microstructure as creep strain will increase the hardness of the steel due to work hardening. Recovery is generally thought to mainly be the result of elevated temperature, with solution strengthening elements gaining energy and creating precipitates in the sub-grain and grain boundaries. The removal of solid solution strengthening and the creation of large precipitates will weaken the metal and lead to the destruction of grain boundaries and lower the steel's strength and subsequently its hardness. Because the low stress area is significantly harder than the gauge length, it suggests that creep stress and not temperature acts as the prominent destabilizing element, responsible for speeding up the recovery of the microstructure. The aged hardness and crept hardness also appear to converge as time-to-rupture increases; this is to be expected as the relative levels of stress inside and outside of the gauge area decrease and the creep stress decreases. In this study, long term tests were created by lowering the creep stress of the sample meaning that as test length increased, changes in the microstructure should also be slowed.

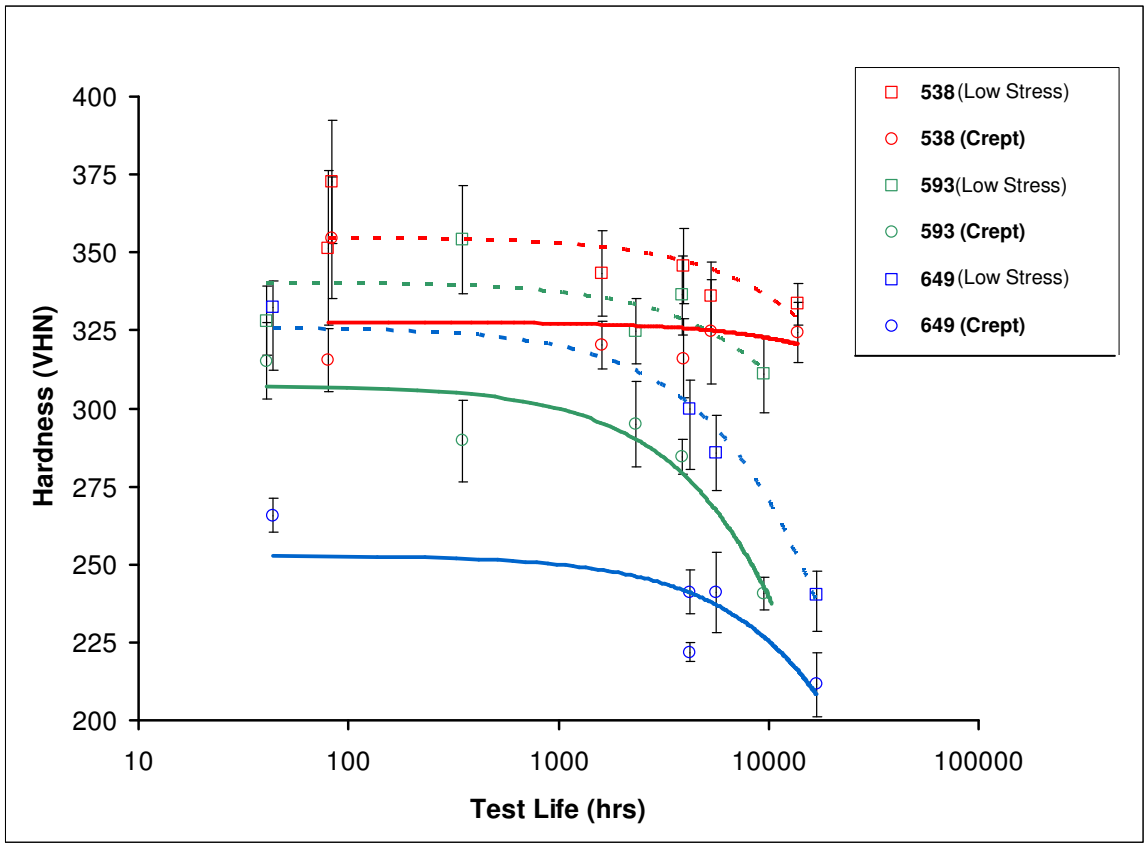

Figure 4.6. Comparison of the hardness between low stress and crept hardness distinguished by test temperature.

Table 4.2. Summary of low stress and crept hardness.

Sample #	Temperature (°C)	Test Life (hrs)	Hardness (Crept)		Hardness (Low Stress)	
			Average	Std.Dev.	Average	Std.Dev
9U	538	79.9	315.4	10.0	351.5	24.7
9AA	538	83.0	354.7	19.6	372.6	19.6
4K	538	1617.0	320.3	7.5	343.2	13.7
5B	538	3932.0	316.1	12.6	345.7	12.1
9AN	538	5335.9	324.6	16.7	335.9	10.9
9AH	538	13747.0	324.3	9.7	333.5	6.7
9V	593	41.0	336.9	12.3	328.1	11.2
9M	593	349.0	315.2	13.2	354.2	17.1
9E	593	2343.0	289.6	13.7	324.8	10.4
6J	593	3866.0	294.8	5.6	336.3	12.8
6N	593	9449.0	284.6	5.3	311.0	12.4
5L	593	10358.2	240.5	4.4	-	-
9Y	649	43.9	265.7	5.6	332.4	8.6
9W	649	4236.0	221.9	3.0	-	-
9S	649	4236.0	241.1	7.1	300.0	9.0
9AD	649	5622.0	240.9	12.9	285.9	12.1
9AB	649	16859.0	211.5	10.3	240.4	7.5
As Received	-	0.0	320.7	6.5	-	-

4.3 Transmission Electron Metallography

Figure 4.7 is a TEM micrograph of as-received ASTM A437 Grade B4B steel. The micrograph exhibits three main structures characteristic of aged and tempered martensitic steel.

Fine precipitates have formed inside the grain boundaries (shown in circle A). The orientation suggests that they have formed along sub-grain boundaries (grain boundaries that have little disorientation between crystal planes). Due to their size, these precipitates are most likely MX and M_3C carbides; it is these precipitates that give ASTM A437 Grade B4B steel good creep resistance. The carbides are most likely to be Vanadium and Tungsten carbides due to the elements' affinity to Carbon and their abundance in ASTM A437 Grade B4B. Tungsten and especially Vanadium tend to create the more stable MX carbides that resist growth at high temperatures. Very few dislocations are apparent within the grain which is to be expected as the sample has been stress relieved during tempering and is at a low stress state.

Along the grain boundaries, larger precipitates have formed (outlined circle B). They are most likely the larger unstable M_3X carbides formed from chromium and molybdenum. Both chromium and molybdenum show high affinity to carbon and tend to form in grain boundaries and other low energy locations as opposed to inside the grain. M_3X carbides, as mentioned previously, are unstable and will agglomerate into larger $M_{23}C_6$ carbides. Due to the high percentage of chromium in the steel, it is most likely that the larger carbides are mainly composed of chromium. Due to their size, the larger $M_{23}C_6$ carbides are not effective in preventing dislocation movement and do little to improve the steel's creep resistance. The agglomeration of M_3X carbides into larger carbides is apparent in the grain boundaries and is highlighted by circle C.

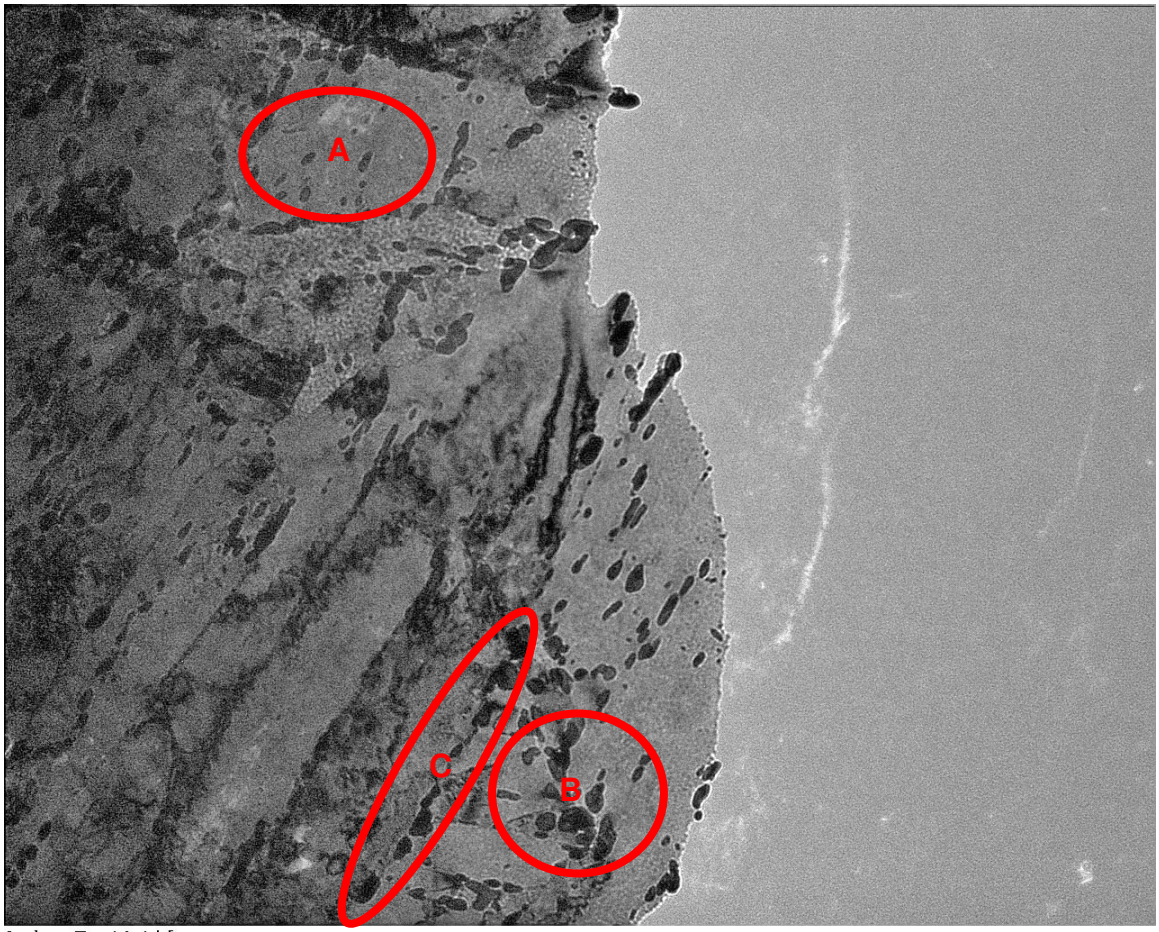

Figure 4.7. TEM micrograph of heat treated ASTM A437 Grade B4B steel.

Figure 4.8 is a TEM micrograph of a crept sample that ruptured after 11300 hrs. This is one of the longest tests performed and a great deal of recovery and carbide growth should be apparent in the microstructure. The micrograph is taken at the same magnification as the as-received sample.

The microstructure no longer has a well defined grain structure and the precipitates have grown substantially. Well ordered grain boundaries apparent in the as-received sample are gone, with former grain boundaries now occupied with large agglomerations of carbides. Small MX carbides still remain within the grain (Outlined by Circle A), but the majority of precipitates are of the larger $M_{23}C_6$ type, present in former grain boundaries (Circle B). Very little evidence of grain boundary sliding is evident with there being little evidence of grain boundaries, let alone the characteristic distinct rounded edges expected from grain boundary interaction. The breakdown of grain boundaries is generally attributed to the formation of Fe_2W or Fe_3Mo intermetallics, which will agglomerate into very large structures at the grain boundaries. Due to the high affinity of vanadium and chromium to carbon, and the unstable nature of M_3X particles, it is likely that the precipitates present at the grain boundaries are a combination of iron-tungsten-molybdenum and chromium carbides. The migration of chromium out of solution and into the grain boundaries will result in a deficiency in the surrounding areas. This opens the door for inter-granular corrosion and can lead to micro-fractures in the material.

Dislocation density has also increased substantially, but that is expected as the sample has been exposed to high stresses. Dislocation movements in the grain (Circle C) do not exhibit a “cork-screw” spiral shape, characteristic of pinning due to the presence of precipitates. Large dislocations are also present in large numbers around former grain boundaries. The larger $M_{23}C_6$ carbides have little effect on slowing movement, with the dislocations moving around the larger particles with little restriction.

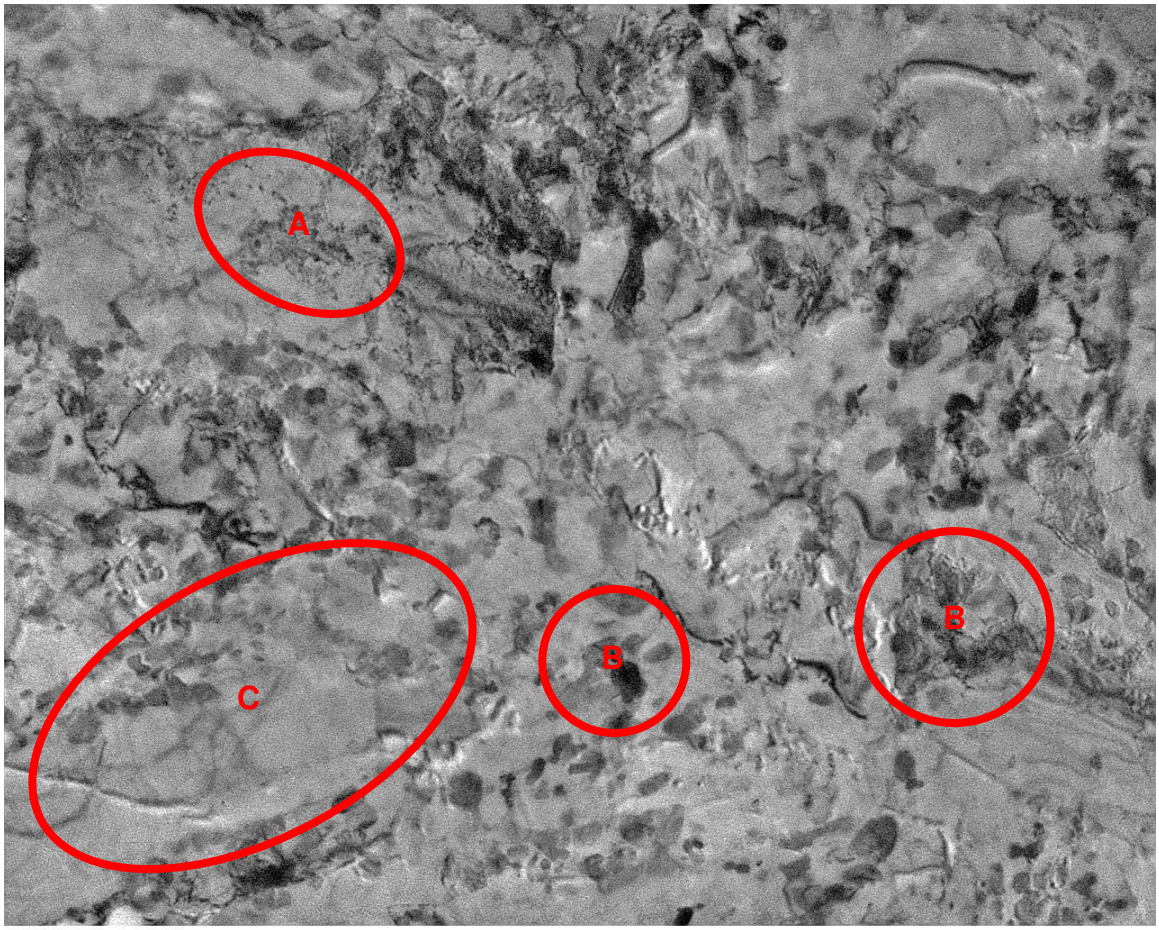

Figure 4.8. TEM Micrograph of a crept sample of ASTM A437 Grade B4Bsteel.

EDS Mapping was attempted to determine what elements were being drawn out of solution to create the phases appearing during creep. Figure 4.9 is a micrograph taken from the test specimen 9T. At this resolution, the more micro-alloyed elements, such as vanadium and titanium, are not apparent in the maps. It does, however, clearly show chromium being pulled out of solution to form the larger carbides, leaving a deficient area in the matrix. The largest agglomeration of chromium appears in the large particles with the smaller neighbouring particles not leaving a footprint in the chromium spectra map. This leads to reinforce the hypothesis that the larger $M_{23}C_6$ are comprised mainly of chromium drawn out of solution during creep aging.

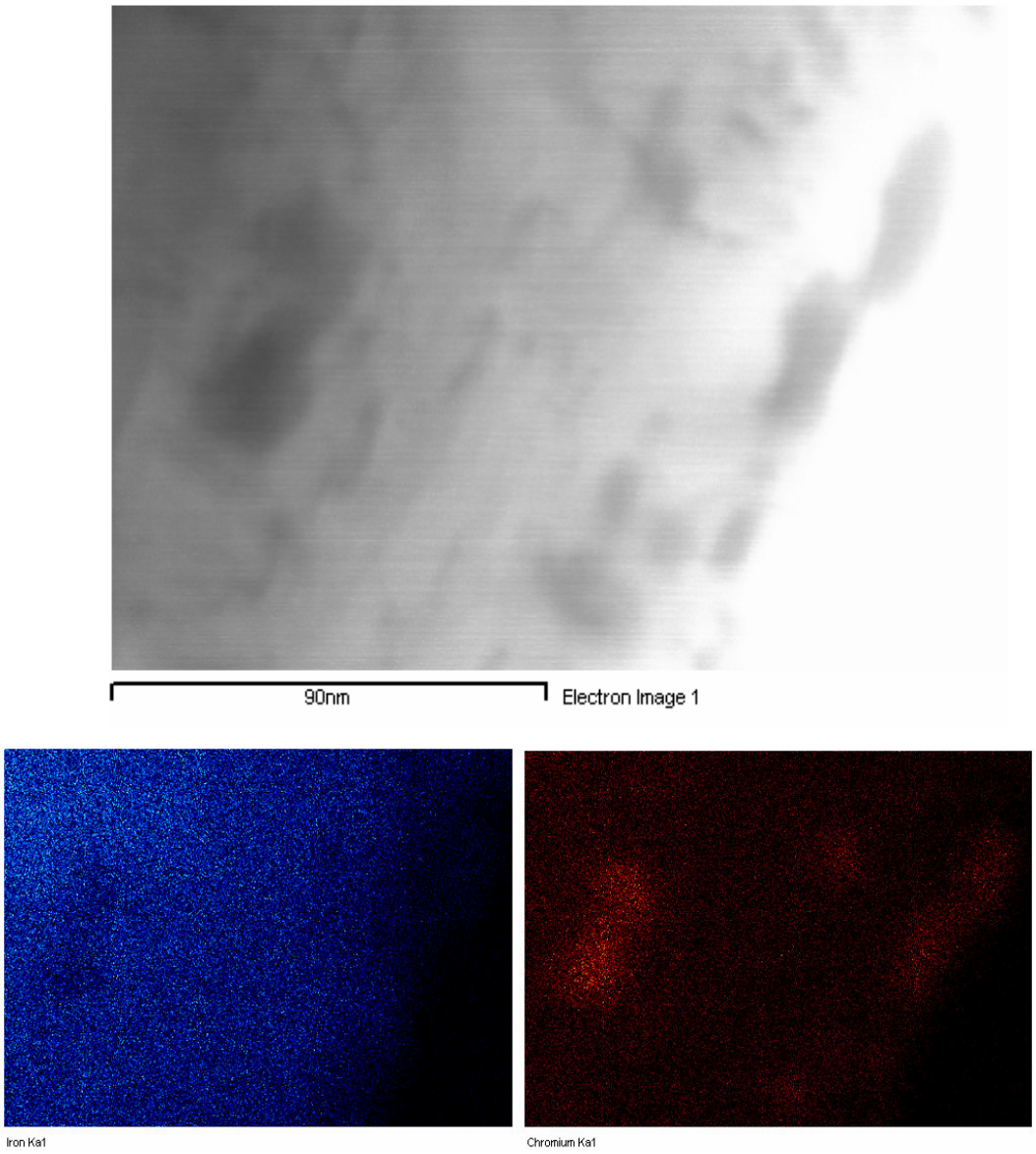

Figure 4.9. TEM micrograph of sample 9T, (a) iron spectrum map, (b) chromium x-ray map.

Figure 4.10 is a higher magnification micrograph of sample 9T taken using the (S)TEM in analog mode. In it, smaller carbides are visible that were not previously resolved in figure 4.9. In analog mode, the mapping functions of the microscope are not available so EDS was performed by adjusting the electron beam so that it is only focused on the area to be analyzed. The first spectrum was taken from the matrix (area outlined in red in Figure 4.10 with the spectra shown in Figure 4.11 and Table 4.3). This was done to verify the accuracy of the method as well as establish a base to compare the following spectrums to. The matrix showed an iron, chromium and nickel rich environment. This

agrees with the chemistry of the steel and is as expected. The scan also showed oxygen, carbon and silicon in large amounts but this can be attributed to contamination during preparation of the samples.

Next, carbides were analyzed (labelled A and B). EDS analysis (shown in Figures 4.12 and 4.13 and Tables 4.4 and 4.5) showed relatively high amounts of chromium and manganese present, with the larger carbides showing significantly more chromium. Tungsten and iron are also apparent in relatively large concentrations. The presence of tungsten suggests that these carbides may have formed from unstable Fe_2W intermetallics. Chromium would have then been drawn out of solution during creep, forming around the unstable phase to create the large $M_{23}C_6$ carbides that are apparent in the microstructure.

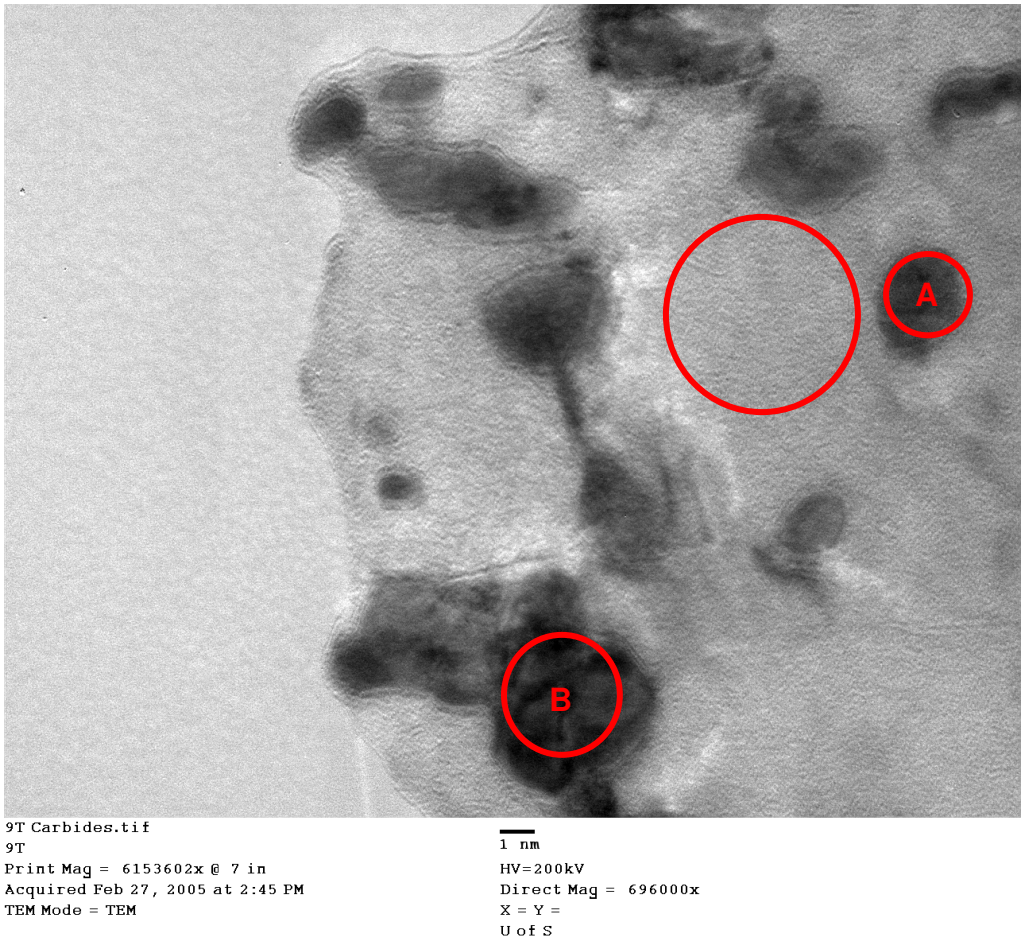

Figure 4.10. TEM micrograph of sample 9T.

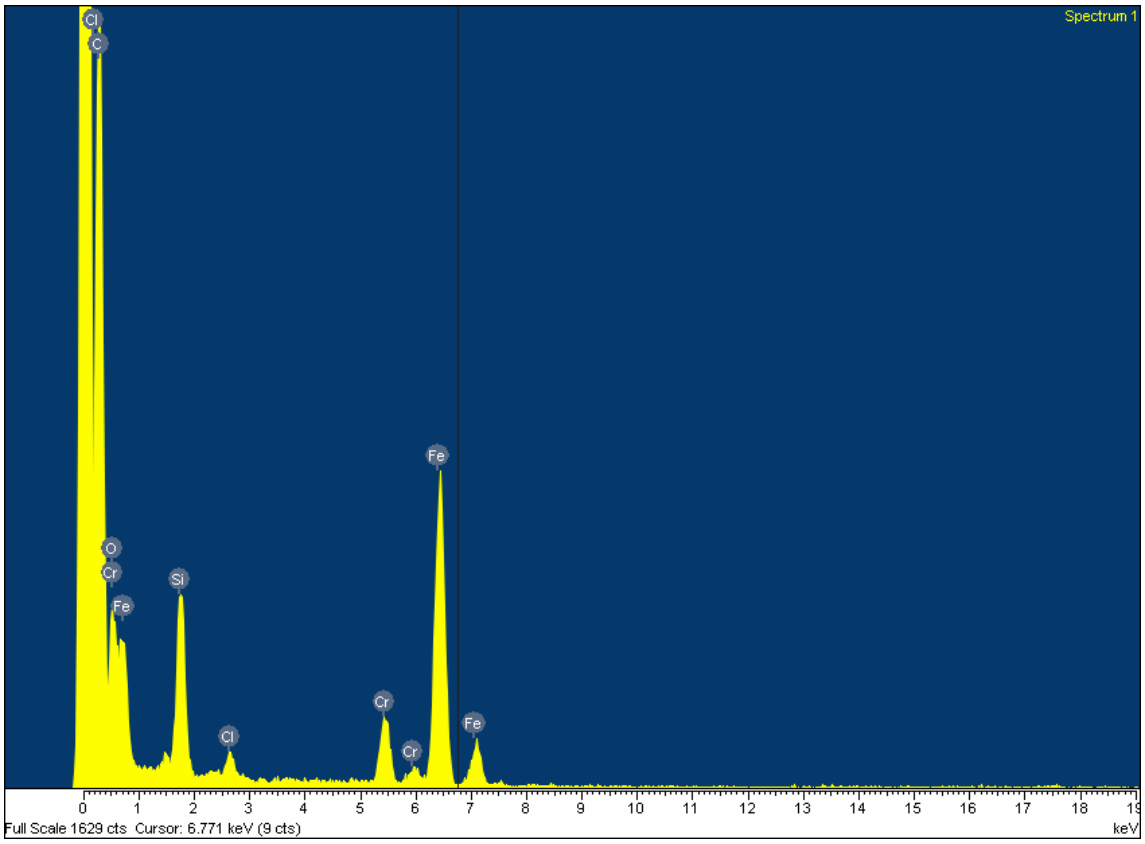

Figure 4.11. EDS spectra from the matrix of Figure 4.10.

Table 4.3. EDS quantization from the matrix

Spectrum Element	C	Si	O	Cr	Cl	Fe	Total
wt. %	62.93	8.49	2.32	4.49	1.21	20.55	100.00

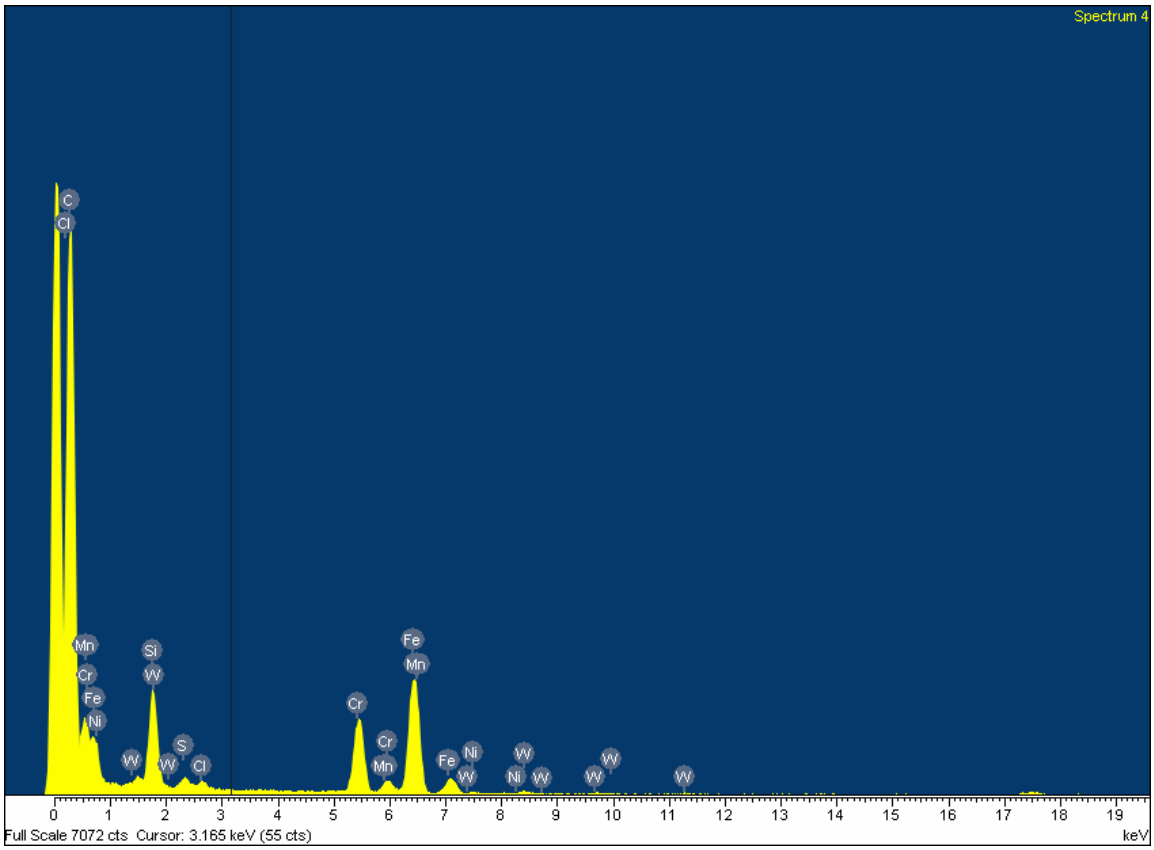

Figure 4.12. EDS spectra from carbide A.

Table 4.4. EDS quantization from carbide A

Spectrum Element	C	Si	S	Cl	Cr	Mn	Fe	Ni	W	Total
Wt. %	72.04	5.22	0.71	0.46	7.42	0.11	12.83	0.16	1.04	100

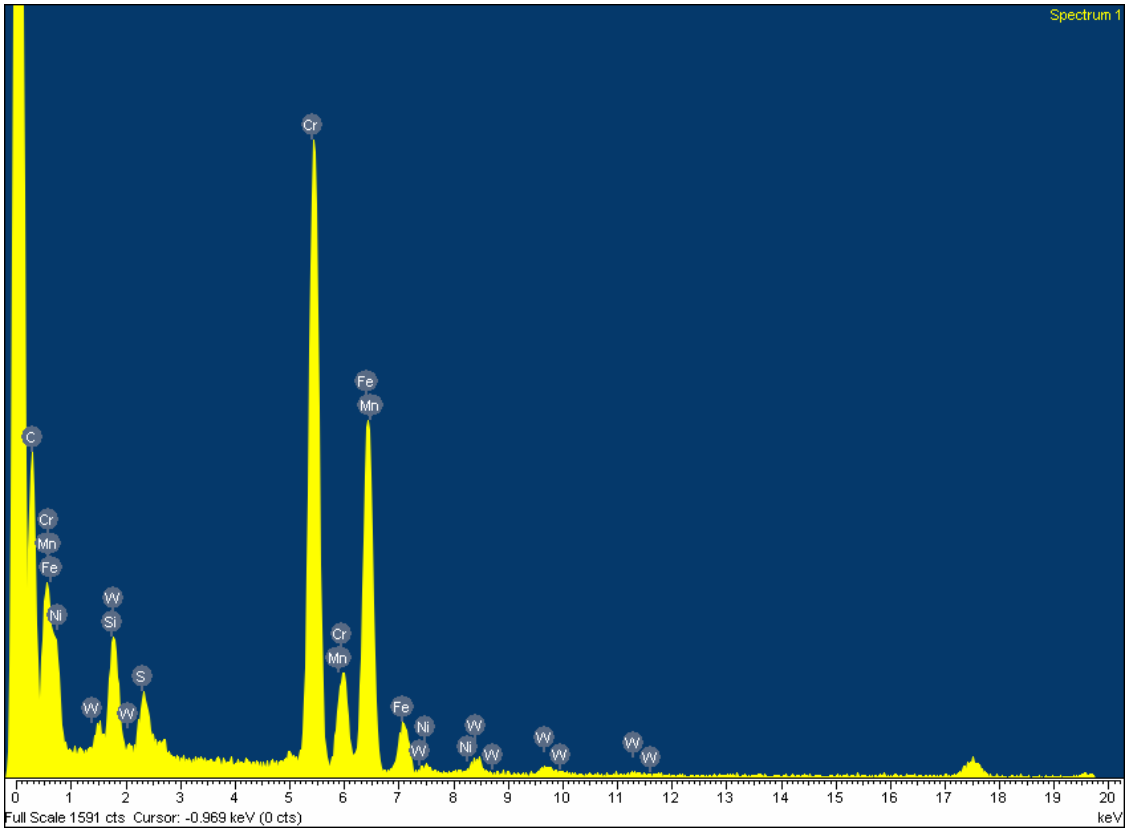

Figure 4.13. EDS spectra from carbide B.

Table 4.5. EDS quantization from carbide B

Spectrum Element	C	Si	S	Cr	Mn	Fe	Ni	W	Total
wt. %	24.48	2.19	2.50	40.52	0.96	24.99	0.50	3.87	100.00

5.0 Conclusions

With the submission of this thesis, creep evaluation of ASTM A437 Grade B4B steel is complete. Short term creep-strain and creep-rupture tests were performed and their results discussed in earlier chapters of this thesis; hardness and initial TEM microscopy were performed and the results discussed.

The following are the conclusions drawn from testing as well as recommendations for the direction of future work on ASTM A437 Grade B4B steel.

Creep Data

A Larson-Miller master plot was completed for ASTM A437 Grade B4B steel. ASTM A437 Grade B4B steel has a very well defined second stage of creep leading to an abrupt transition to third stage. The following observations were made:

1) The secondary stage begins in the first 10% of creep life, with third stage beginning at 90% of creep life.
2) This equates to 5% and 30% of the total creep strain, respectively, with an average final strain of 20% of gauge length.
3) Two thirds of the total strain occurs in the tertiary stage of creep.
4) Because of the homogeneity of data between tests, it is possible to predict the creep life of a component by calculating the steady state strain rate and using the Larson-Miller master plot to determine total creep life.

Time-to-Rupture data showed good correlation to creep life predicted using the Larson-Millar method; with the following observations:

1) Error increased as the creep stress decreased and the length of the test increased.
2) Despite the error, the Larson-Miller method predicted conservative times to rupture for longer life tests with specimens failing after the estimated creep life; and
3) The creep data showed a definite correlation between steady state strain rate, temperature, and creep stress. The resulting empirical formula was developed from data:

$$\dot{\varepsilon}_{SS} = \left(\frac{T}{1043}\right)^{84.6} \exp[0.044\sigma]$$

where, T is the absolute temperature in Kelvin and σ is the creep stress in MPa.

The formula suggests that during service, temperature does not begin to affect the steady state strain rate until it reaches 1040 K (770ºC). Typically, ASTM A437 Grade B4B steel would not be used in service much above 600ºC leaving stress as the driving mechanism behind creep.

With the above information, it is possible to model the life of a component. To explain using the example of a bolted connection, the stress relaxation of the connection may be predicted using the above equation since it can be safely assumed that the material can be characterized by second stage creep. Maintenance schedules can be then developed to re-tension the connection and using Larson-Miller a lifetime for the bolt can be estimated, allowing scheduled replacement.

Hardness

Hardness testing was performed using a Vickers microhardness indenter on crept samples of ASTM A437 Grade B4B steel in both the gauge length and the low-stress, aged area. Results showed a significant drop in hardness in the strained gauge area when compared to aged areas. This reinforces the above stated correlation that stress

has an important destabilizing effect upon microstructure, decreasing strength. As the test temperature increased, both the aged and crept hardness decreased.

TEM

Preliminary TEM results showed significant differences in the microstructure of the crept and as-received steel. The following observations were made:

1) Coarsening of carbides along grain boundaries caused a recovery of the microstructure;
2) The lack of definite grain boundaries suggests that these phases are Fe_2W and Fe_3Mo with larger $M_{23}C_6$ particles probably comprising of Chromium and Vanadium;
3) Dislocations within the creep microstructure are not as effectively restricted by precipitates; the creep resistance of the material has decreased substantially; and
4) Most likely the growth of precipitates and recovery of the microstructure coincides with the entry into third stage creep.

Recommendations for Future Work

With creep testing finished, future work should be devoted to identifying the evolving microstructure. By identifying what elements are dropping out of solution during creep, the kinetics behind the evolution of the microstructure can be determined and the accuracy of the Larson-Miller method to predict creep life can be evaluated.

Interrupted testing can also be utilized to determine where during creep, recovery and precipitation growth begins. Hardness testing on samples interrupted before and after entry into third stage creep should show significant differences in hardness. It has been suggested the growth of precipitates and the destruction of grain boundaries is what signals the entrance into third stage creep. Relating the evolving microstructure to changes in hardness will confirm this.

References

1. S. H. Griffin, "The Creep Behavior of Three Alloy Steels for Steem Turbine Applications" M.Sc. Thesis, University of Saskatchewan, 2001

2. D. M. McCullough, "Creep behavior of 12CrMoVW Martensitic stainless steel" M.Sc. Thesis, University of Saskatchewan, 2002

3. D. McLean, 1977, *Mechanical Properties of Metals*, Huntington, New York, p.291

4. M. Tendo, K. Yamada, 2001, "Stress Relaxation Behavior at High-Tension Bolted Connections of Stainless-Steel Plate", *Transactions of the ASME*, p. 198-201

5. F. W. McClintock and F. A. Argon, *Mechanical Behavior of Materials*, Addison Wesley Press, 1996, page 625.

6. R. A. Flinn, P. K. Trojan, *Engineering Materials and Their Application*, 4th Ed., John Wiley & Sons, Toronto, p. 367

7. C. Sargent, 2001, "ME471 Lecture Notes", Department of Mechanical Engineering, University of Saskatchewan, Saskatoon

8. E. C. Rollanson, *Metallurgy for Engineers*, 4th ed., English Language Book Society, 1973.

9. J. P. Hirth and J. Lothe, *Theory of* Dislocations, McGraw-Hill, 1968

10. J. F. Shackelford, *Introduction to Materials Science for Engineers*, 4th ed., Prentice-Hall Inc, 1996.

11. F. R. Larson, J. Miller, 1952, "A Time-Temperature Relationship for Rupture and Creep Stresses" *Transactions of the ASME*, p. 765-774

12. S. S. Mason, A. M. Haferd, 1943, "A Linear Time-Temperature Relation for Extrapolation of Creep and Stress-Rupture Data" *National Advisory Committee for Aeronautics*, Technical Note 2890.

13. K. W. Poh, 1998, "General Creep-Time Equation, *Journal of Materials in Civil Engineering*, Vol. 10 Issue 2, p. 118

14. D. R. Hayhurst, 1994, "The Use of Computational Creep Continuum Damage Mechanics to Optimize Materials Selection for High-temperature Weldments", *Modelling Simul. Mater. Sci. Eng.*, UK, p. 423

15. H. Jeong, D. H. Kim, 2002, "Estimation of Creep Voids Using a Progressive Damage Model and Neural Networks" *Nondestructive Evaluation*, Springer-Verlag New York, New York, pp. 33-45
16. L. S. Toth, A. Molinari, 2002, "Strain Hardening at Large Strains as Predicted by Dislocation Based Polycrystal Model", *Journal of Engineering Material and Technolog*, ASME, pp. 71-76
17. Y. F. Yin and R. G. Faulkner, "Modeling the effects of alloying elements on precipitation in ferritic steels" *Materials Science & Engineering*, vol. A344, 2003 pgs 98, 100.
18. Bethlehem Steel, *Modern Steels and Their Properties*, Bethlehem Steel Corporation, Bethlehem, PA, 1972
19. K. J. Irvine, D. J. Crowe and F. B. Pickering, "The physical metallurgy of of 12% Chromium Steels" *The Metalurgical Evolution of Steels*, The Metals Society, 1979 page 48.
20. J. Presicka, R. Kuzel, A. Dronhofer and G. Eggeler, "The evolution of dislocation density during heat treatment and creep of tempered martensite ferritic steels" *Acta Materialia*, vol. 51, 2003, page 4852.
21. J. Janovec, M. Scoboda, and J. Blach, "Evolution of secondary phases during quenching and tempering 12% Cr steel" *Materials Science & Engineering*, vol. A 249, 1998, page 184..
22. F. B. Pickering, "The Metalurgical Evolution of Stainless Steels", *The Metalurgical Evolution of Stainless Steels*, The Metals Society, 1979.
23. A. Orlova, J. Bursik, K. Kucharova and V. Sklenicka, "Microstructural development durring high temperature creep of 9% Cr. Steel" *Materials Science and Engineering*, vol. A245, 1998, pg. 42.
24. J. Janovec, B. Richarz and H. J. Grabke, "Some Aspects of Intermetallic Phase Precipitation in a 12% Cr-Steel" *Scripta Metallurgica et Materialia*, vol. 233 pg. 295.
25. D. H. Ping, M. Ohnuma, Y. Hirakawa, Y. Kasoya and K. Hono, "Microstructural evolution in 13Cr–8Ni–2.5Mo–2Al martensitic precipitation-hardened stainless steel" *Material Science & Engineering*, vol. A 394, 2005, page 295.

26. P. J. Ennis, A. Zielinska-Lipiec, O. Wachter and A. Czyrska-Filemonowicz, "Microstructural Stability and Creep Rupture Strength of the Martensitic Steel P92 for Advanced Power Plant" *Acta Metallugica*, vol. 45, page 4903.
27. F. Abe, "Creep rates and strengthening mechanisms in tungsten-strengthend 9Cr steels" *Materials Science & Engineering*, vol. 319, 2001 page 771.
28. "Standard Specification for Alloy-Steel Turbine-Type Bolting Material Specially Heat Treated for High-Temperature Service", *A 437/A 437M – 97, 1998 Annual Book of Standards*, American Society for Testing and Materials, West Conshoken, PA, 1998.
29. ASTM Standard E-139-96, 1996 Annual Book of Standards, American Society for Testing and Materials, West Conshoken Society for Testing and Materials.
30. Hitachi High technologies America Inc, http://www.hitachi-hta.com/.

Appendix A – Creep-Strain Plots

The following are strain-time plots for each creep strain test performed on ASTM A437 Grade B4B steel. The full curve as well as the linear region has been plotted. A plot of the strain rate which was used to determine the time spent in each of the stages of creep is also shown.

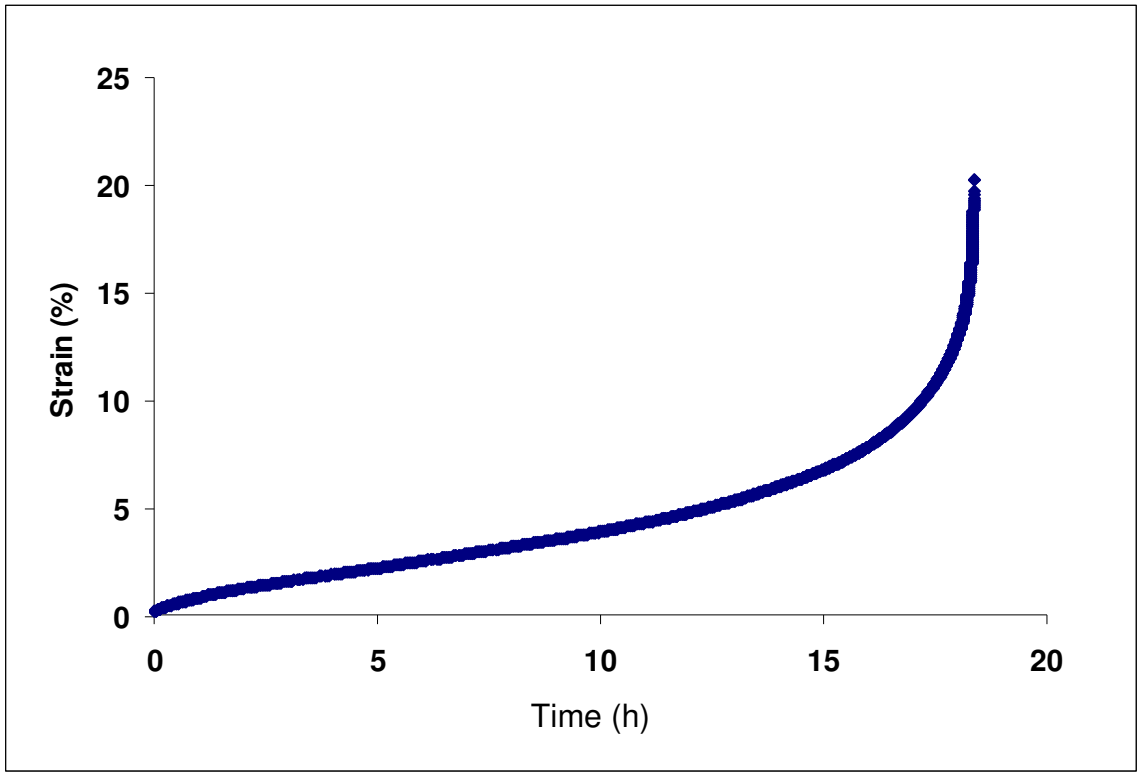

Figure 1-a, Test 4B 538°C @ 426.6 MPa.

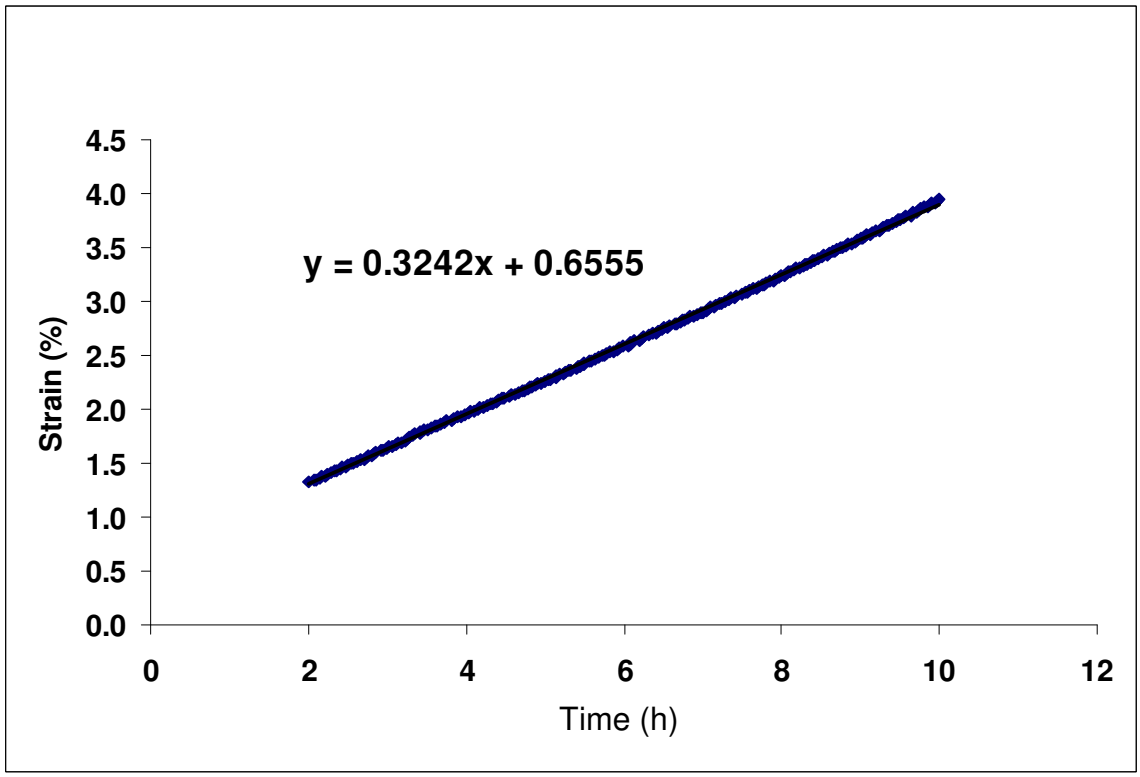

Figure 1-b, Test 4B, second stage creep plot.

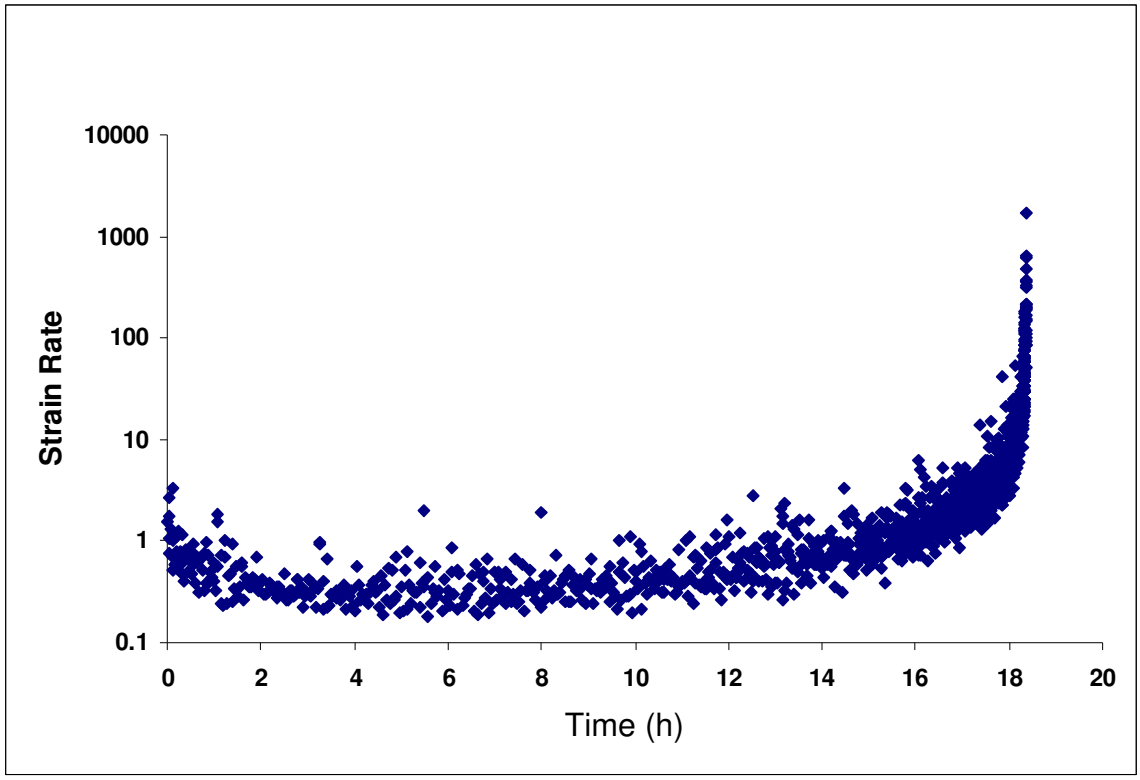

Figure 1-c, Test 4B creep rate plot.

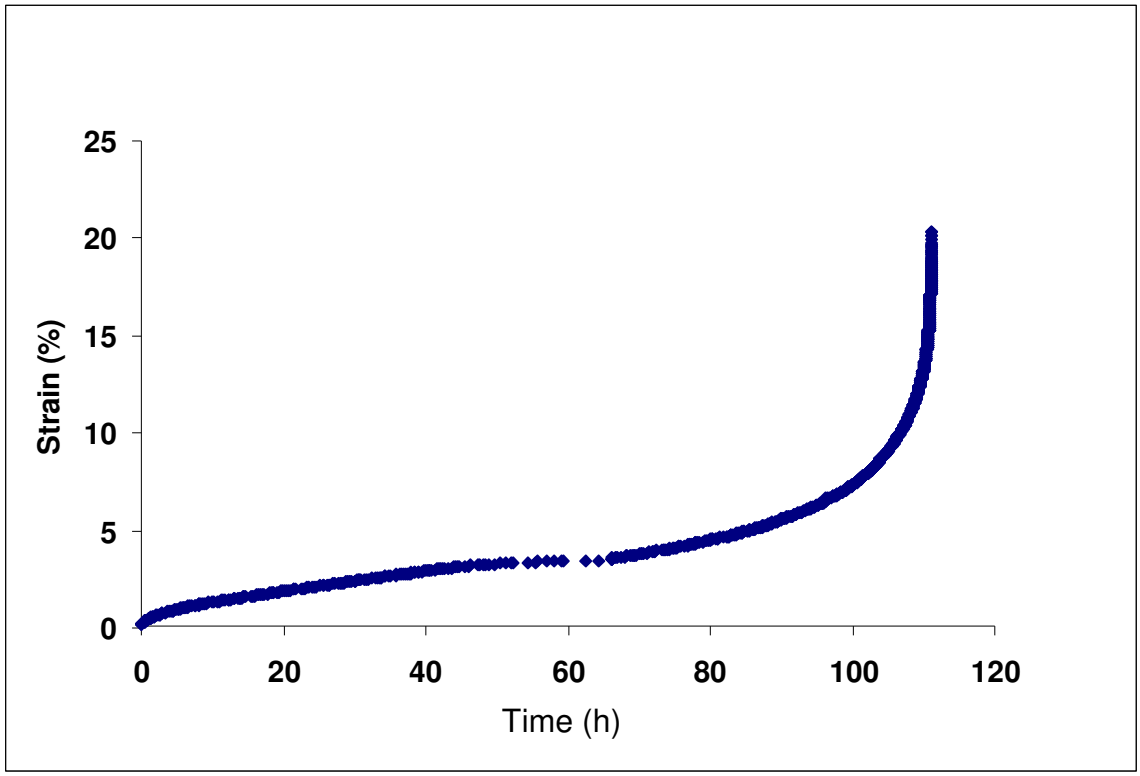

Figure 2-a, Test 4C, 538°C @ 400 MPa.

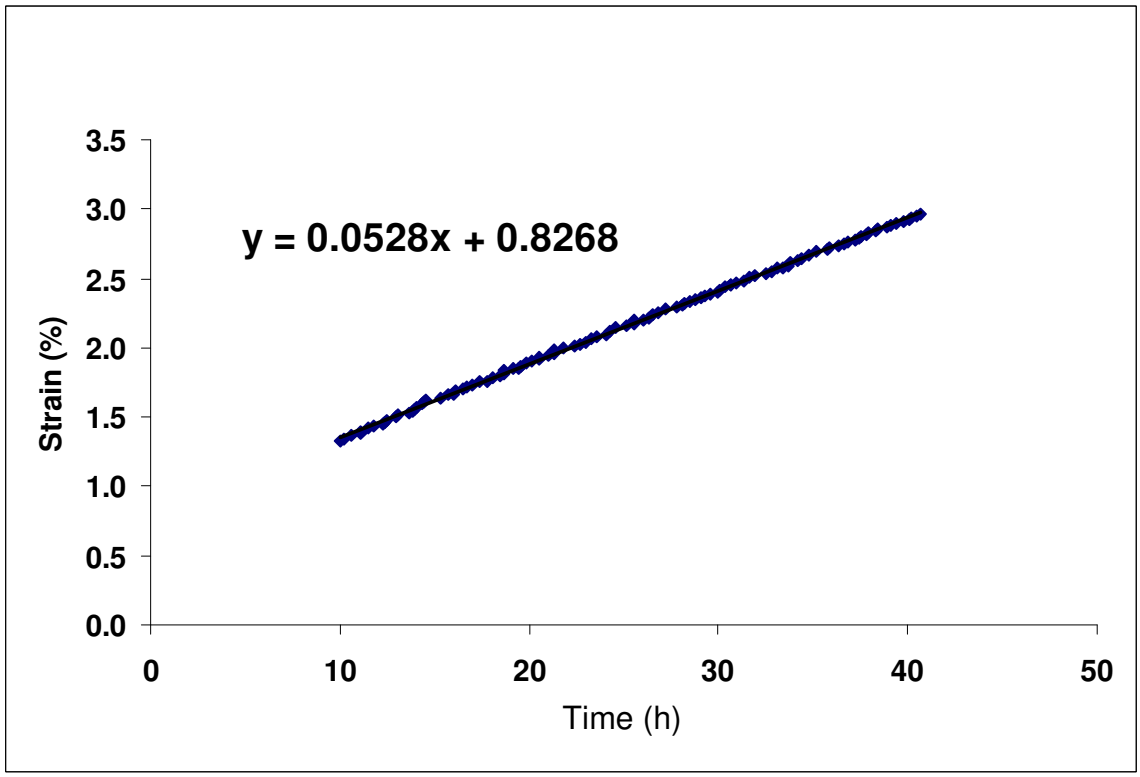

Figure 2-b, Test 4C second stage creep plot.

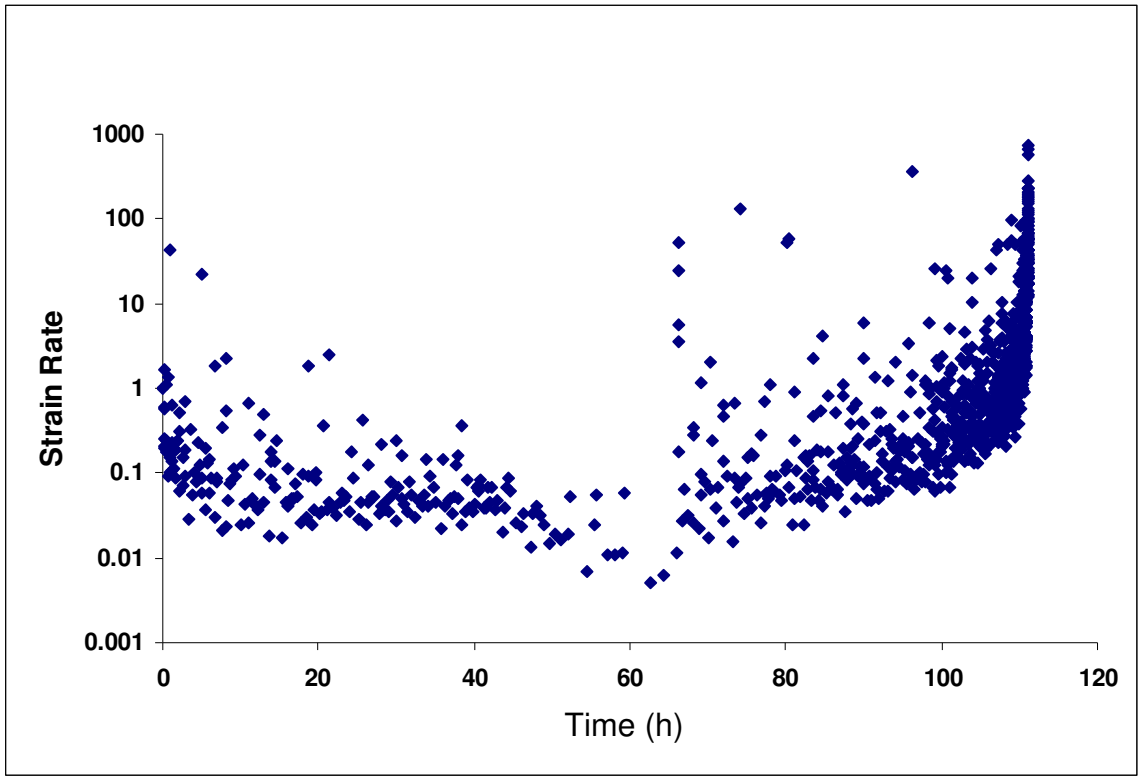

Figure 2-a, Test 4C strain rate plot.

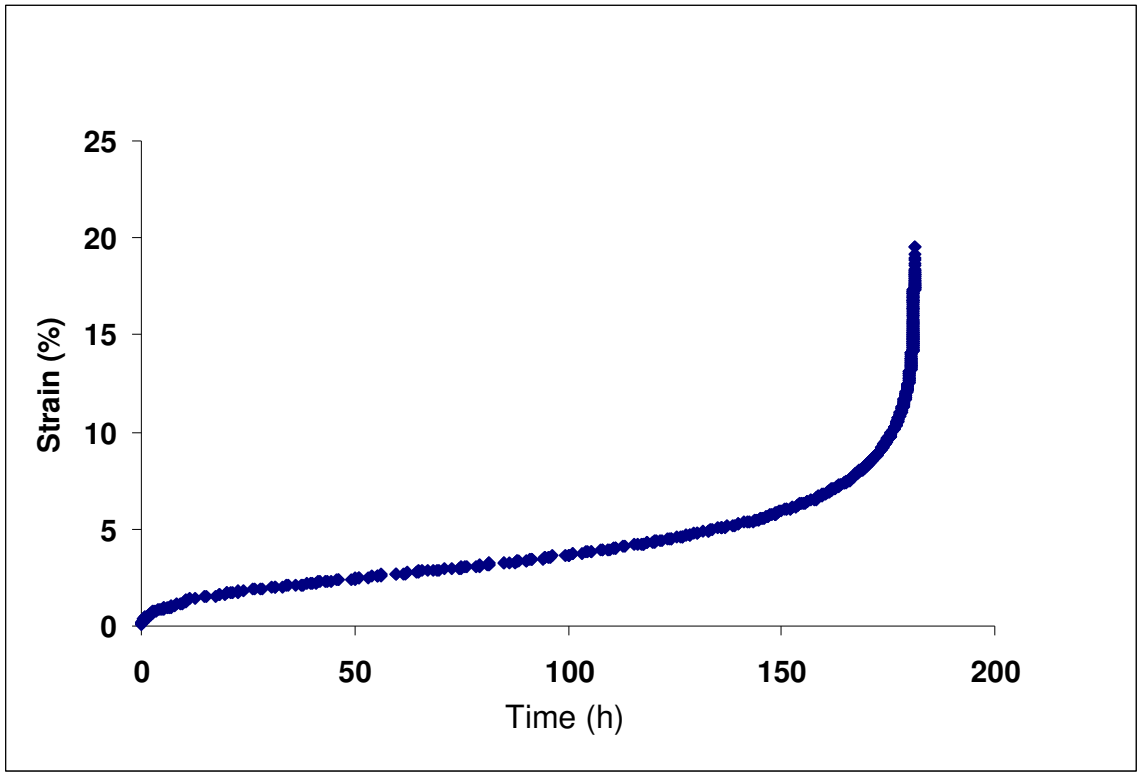

Figure 3-a, Test 5D, 538°C @ 394.3 MPa.

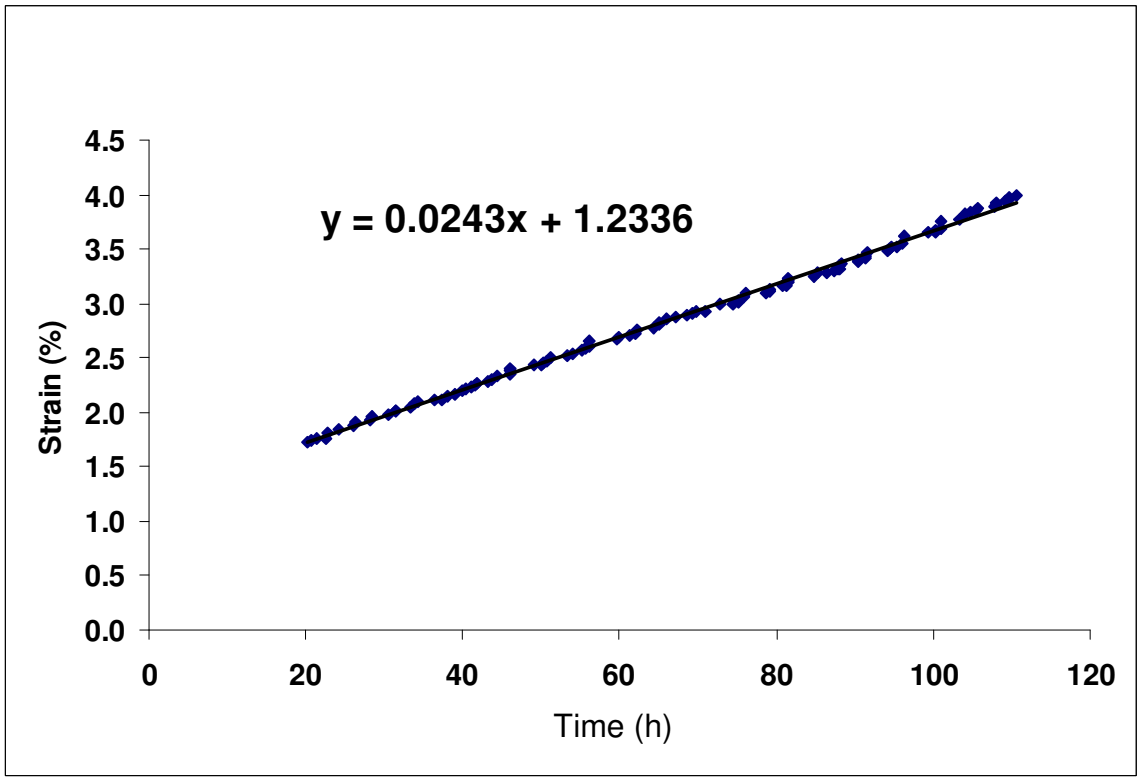

Figure 3-b, Test 5D second stage creep plot.

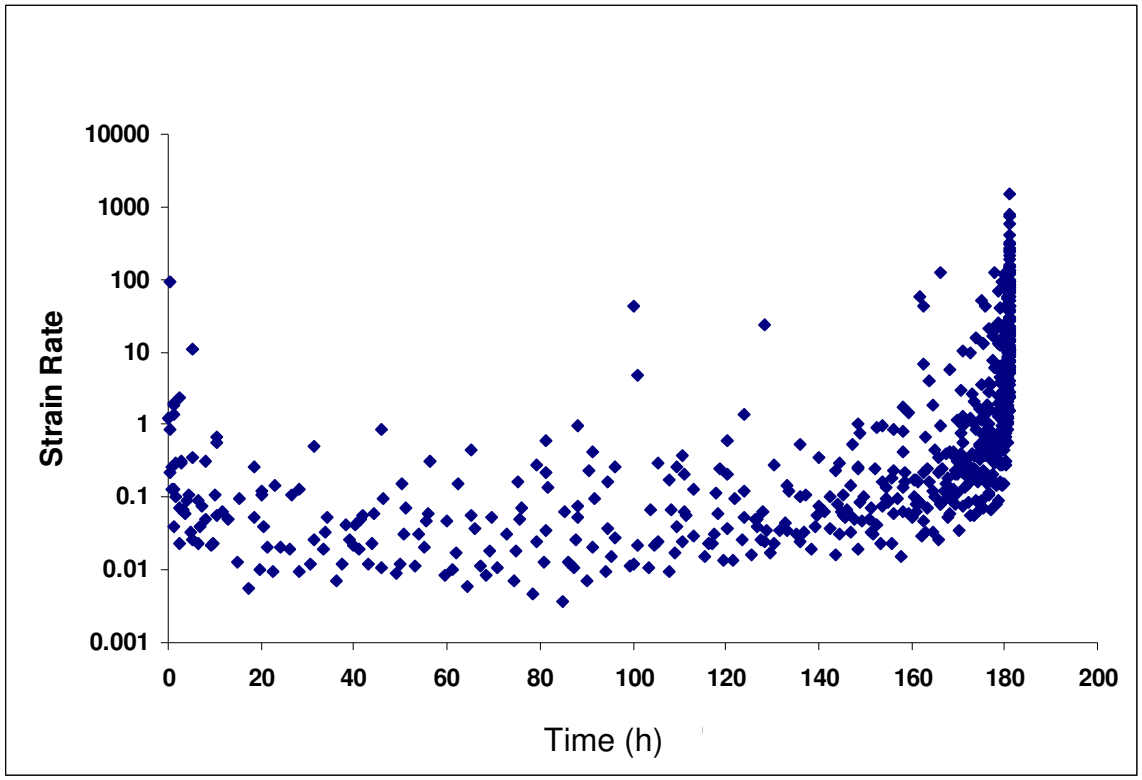

Figure 3-c, Test 5D strain rate plot.

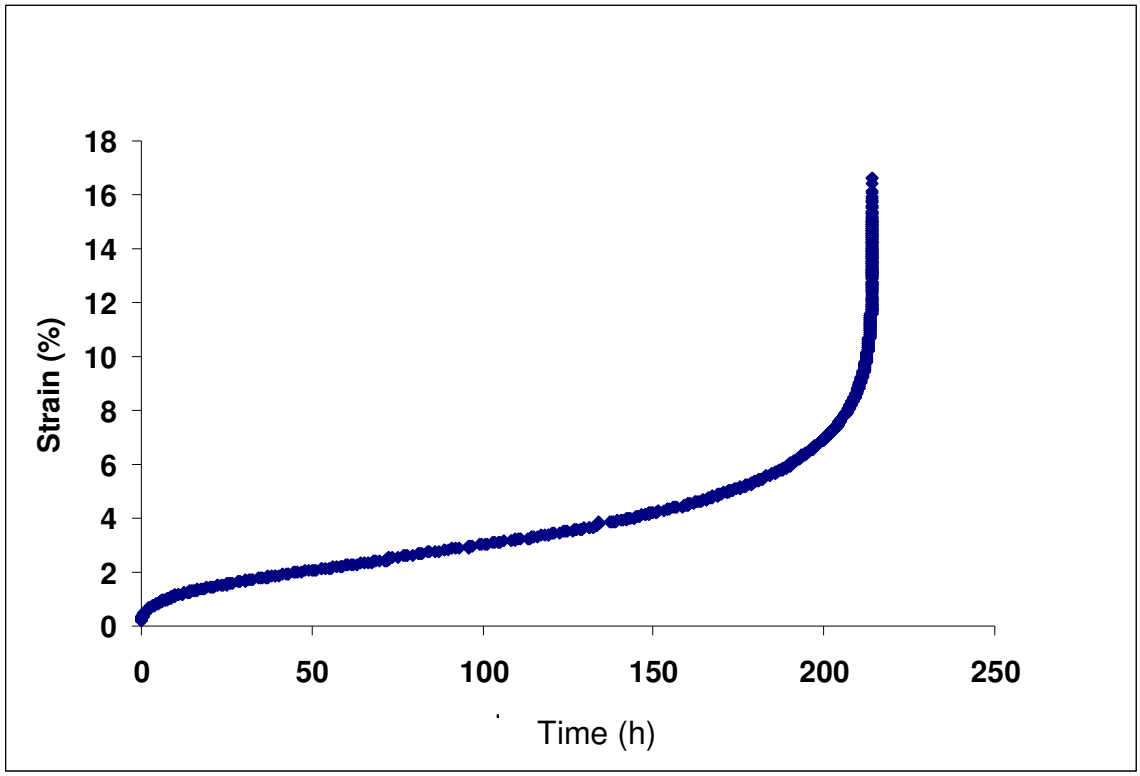

Figure 4-a, Test 5J, 538°C @ 215 MPa.

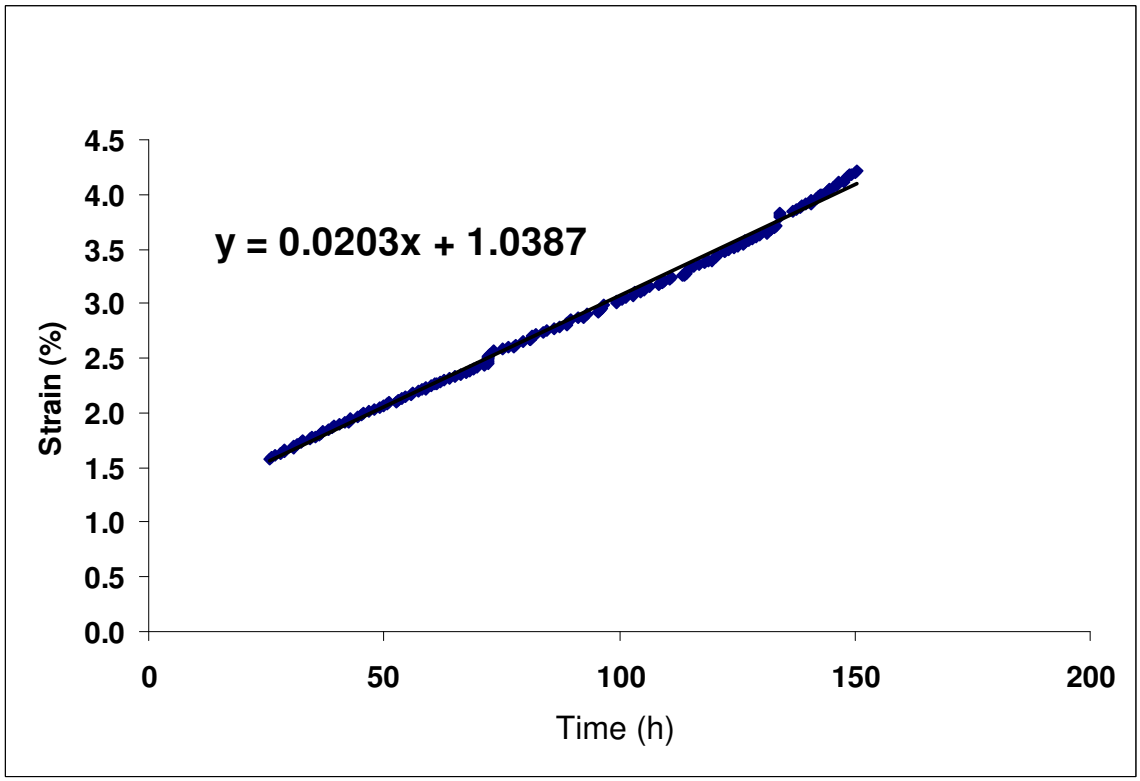

Figure 4-b, Test 5J second stage creep plot.

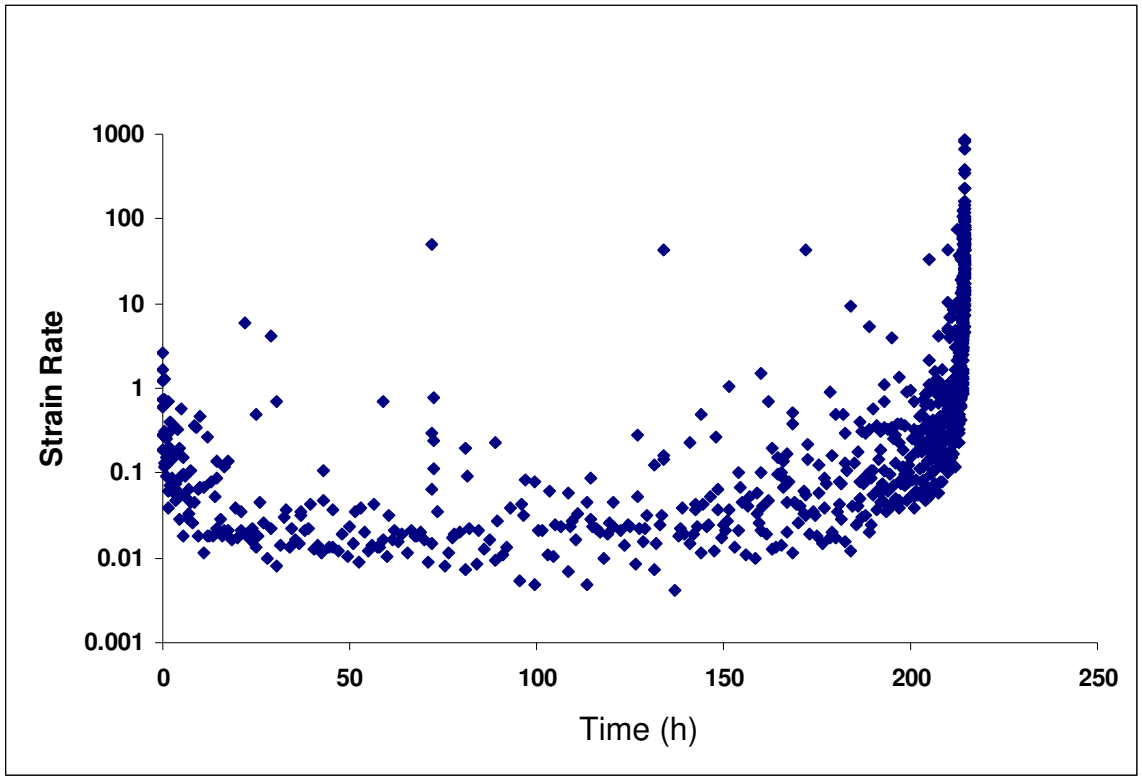

Figure 4-c, Test 5J strain rate plot.

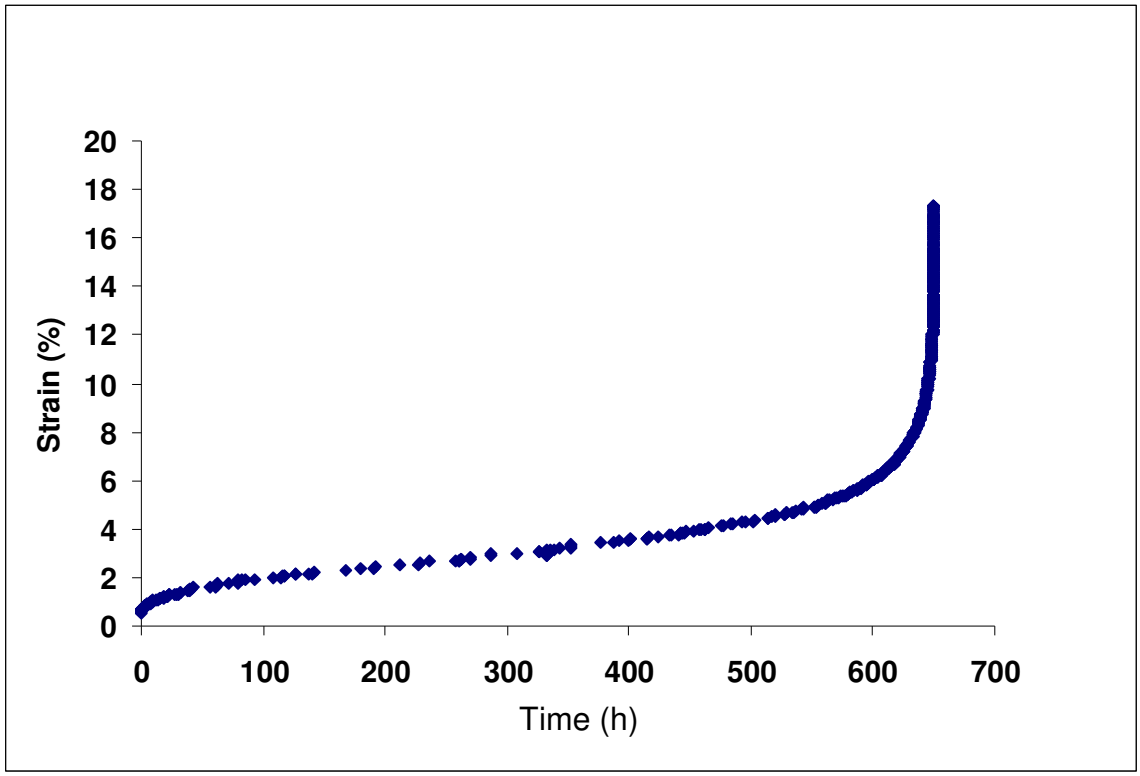

Figure 5-a, Test 9F, 538°C @396.3 MPa.

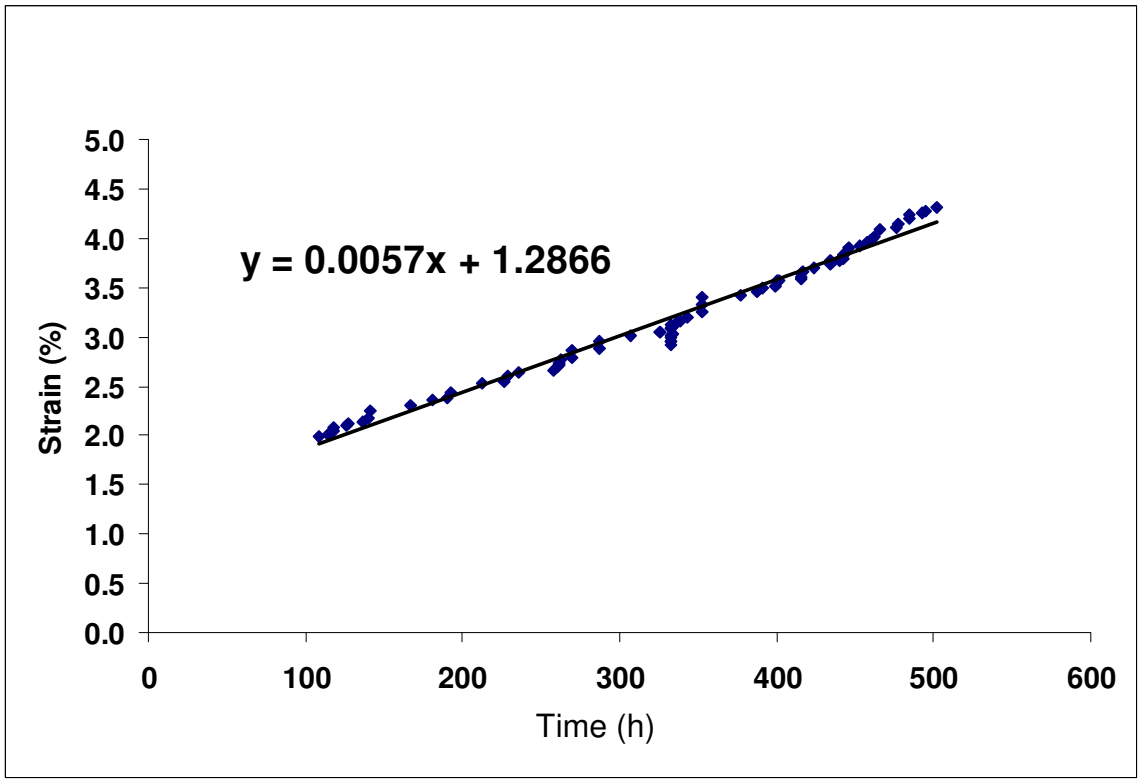

Figure 5-b, Test 9F second stage creep plot.

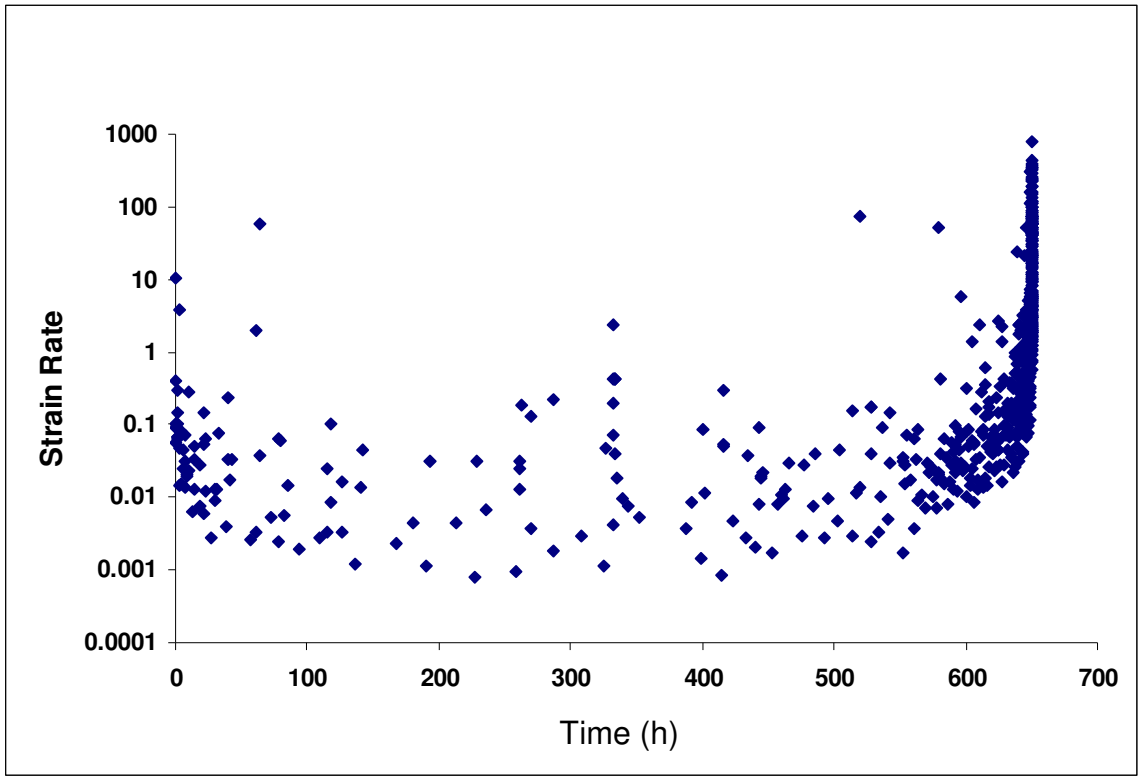

Figure 5-c, Test 9F strain rate plot.

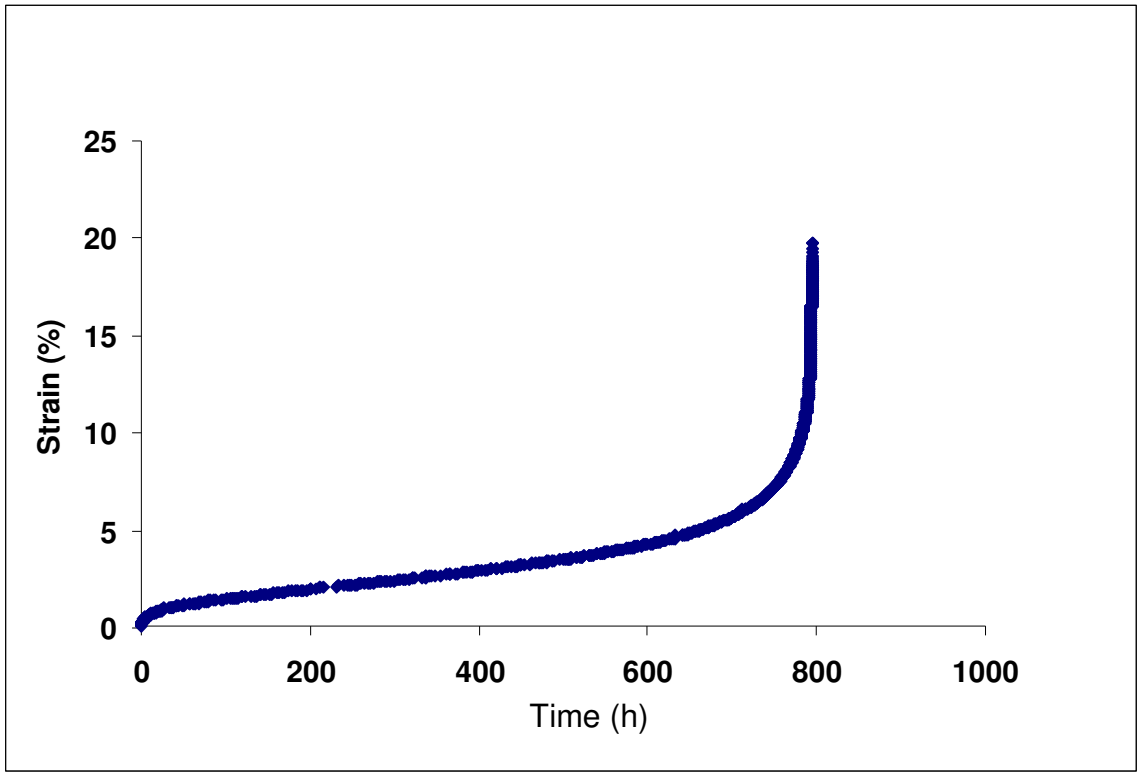

Figure 6-a, Test 4D, 538°C @ 370.6 MPa.

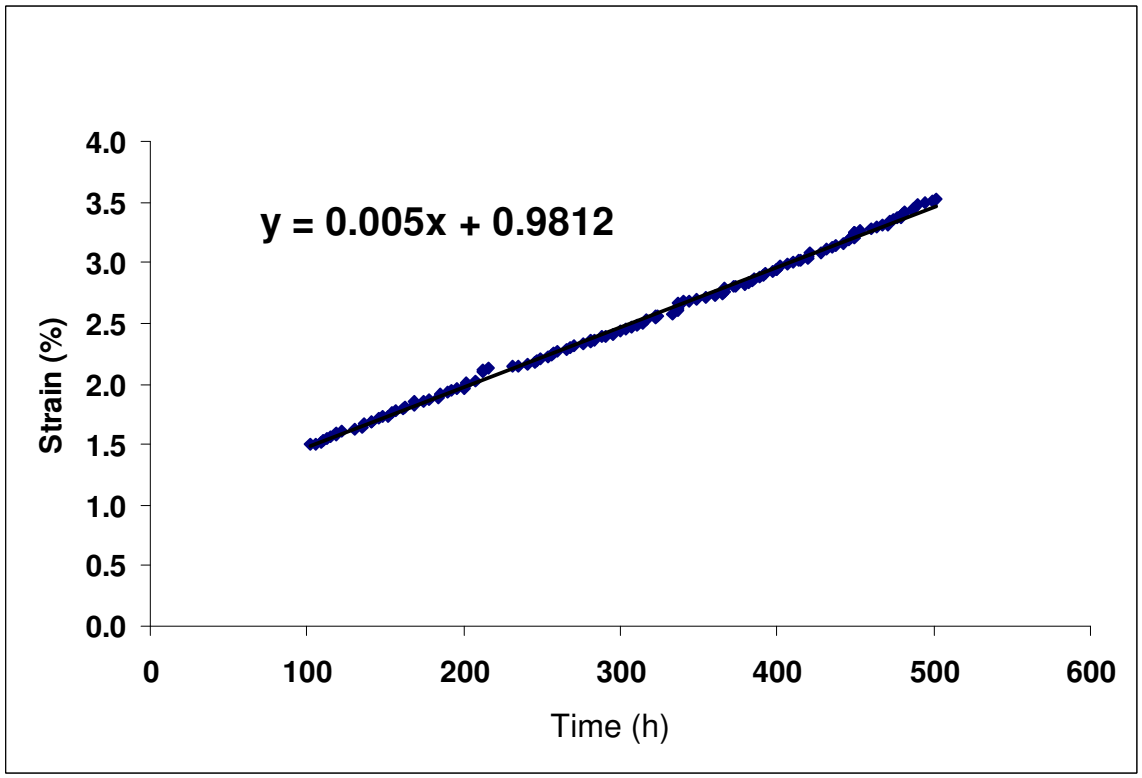

Figure 6-b, Test 4D second stage creep plot.

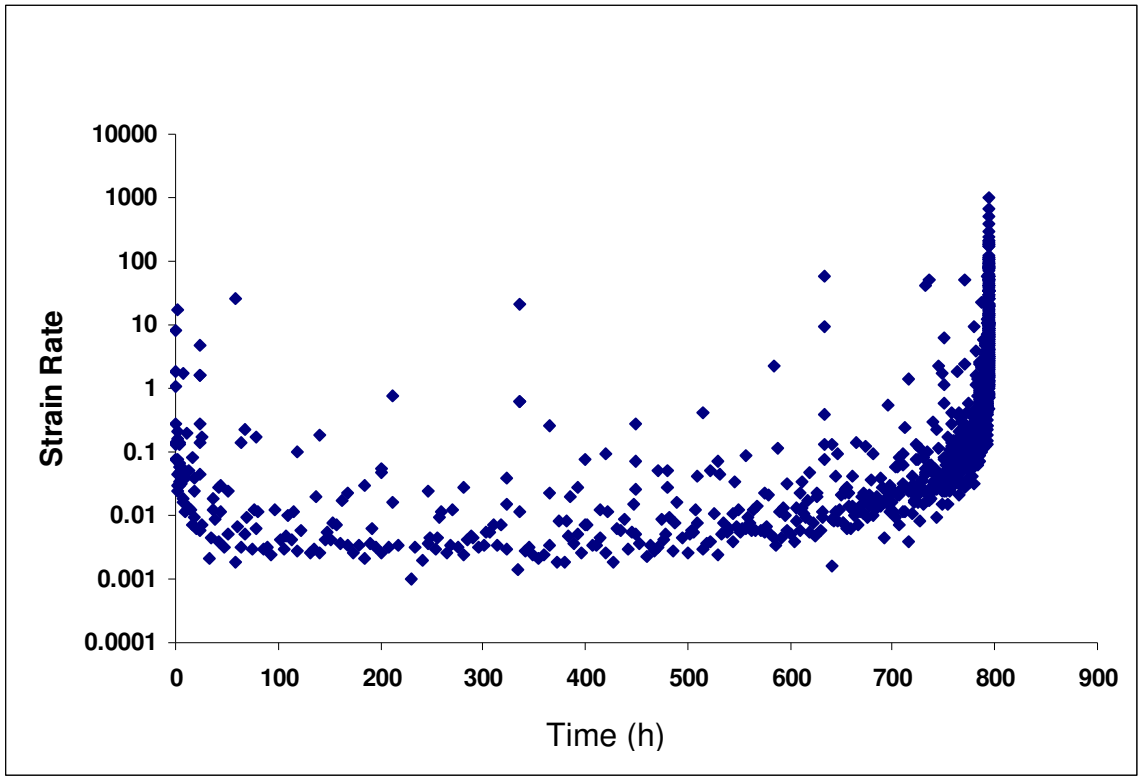

Figure 6-c, Test 4D strain rate plot.

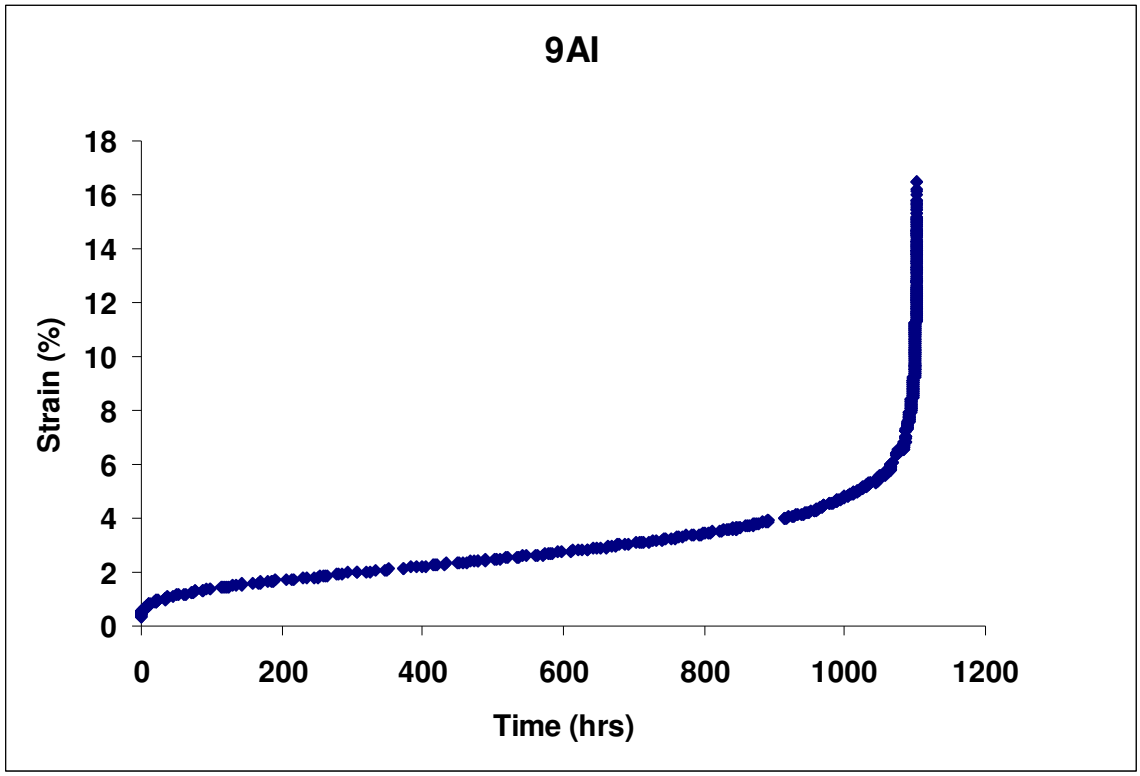

Figure 7-a, Test 9AI, 538°C @350.5 MPa.

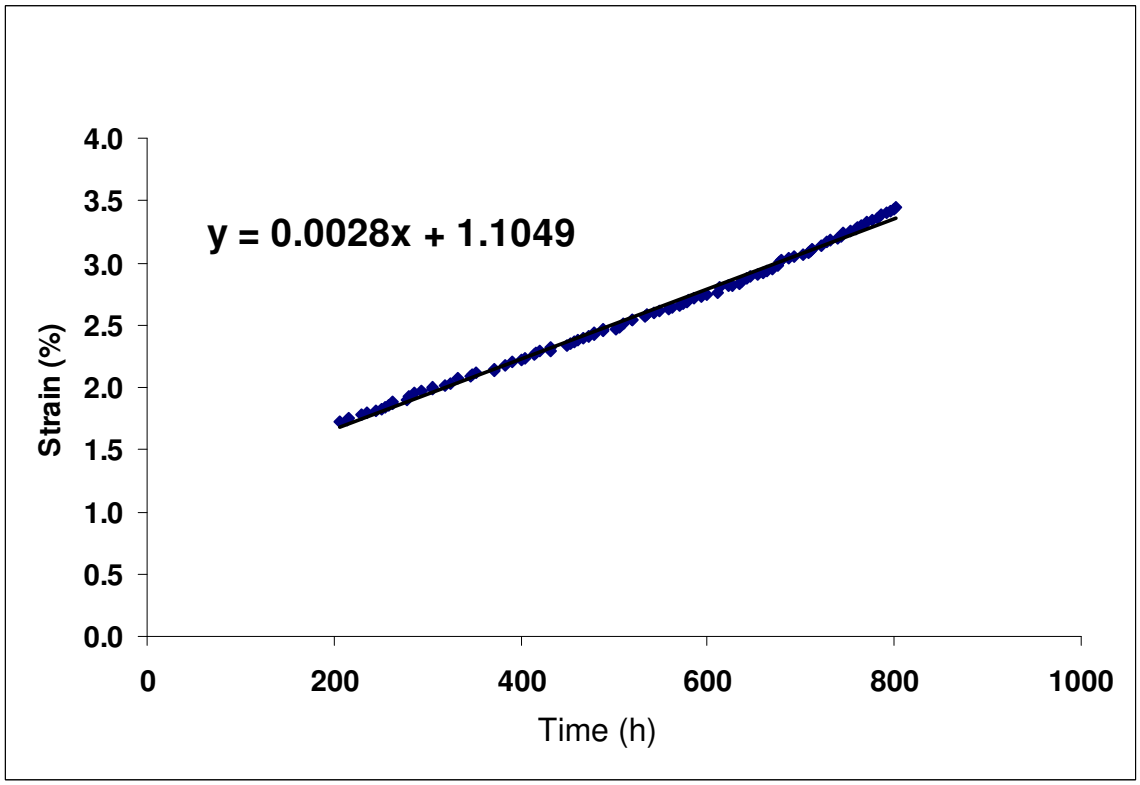

Figure 7-b, Test 9AI second stage creep plot.

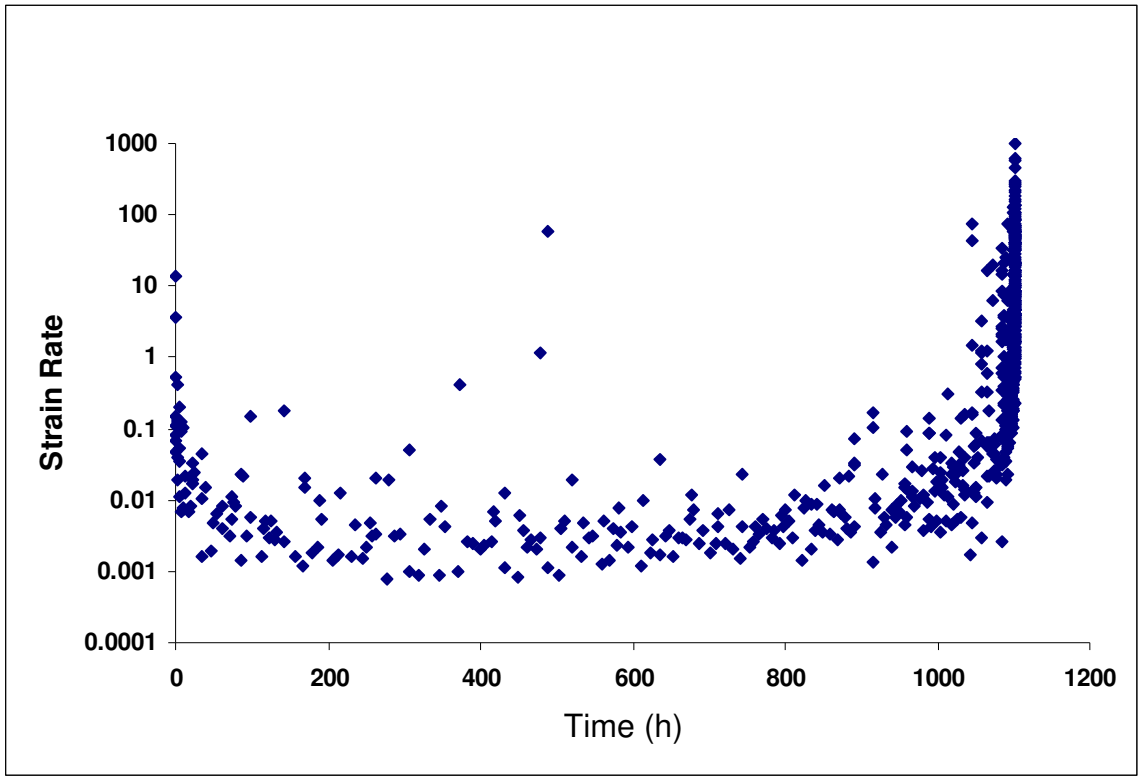

Figure 7-c, Test 9AI strain rate plot.

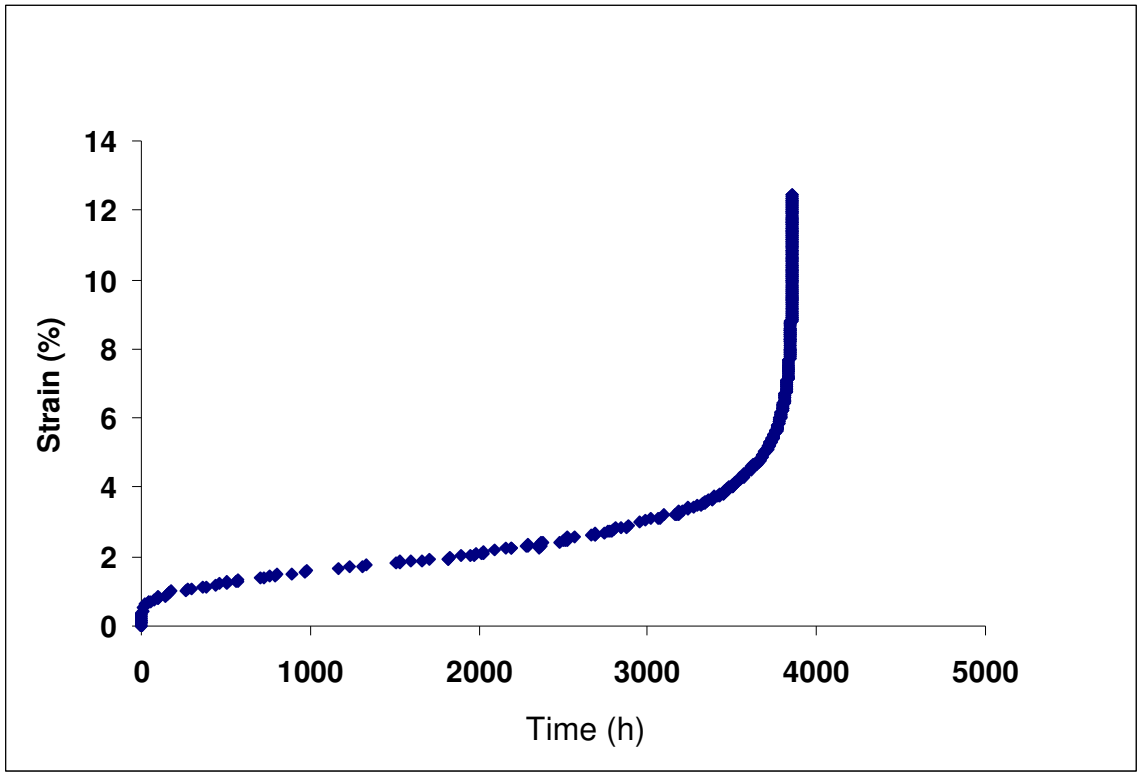

Figure 8-a, Test 5B, 538°C @ 330.8 MPa.

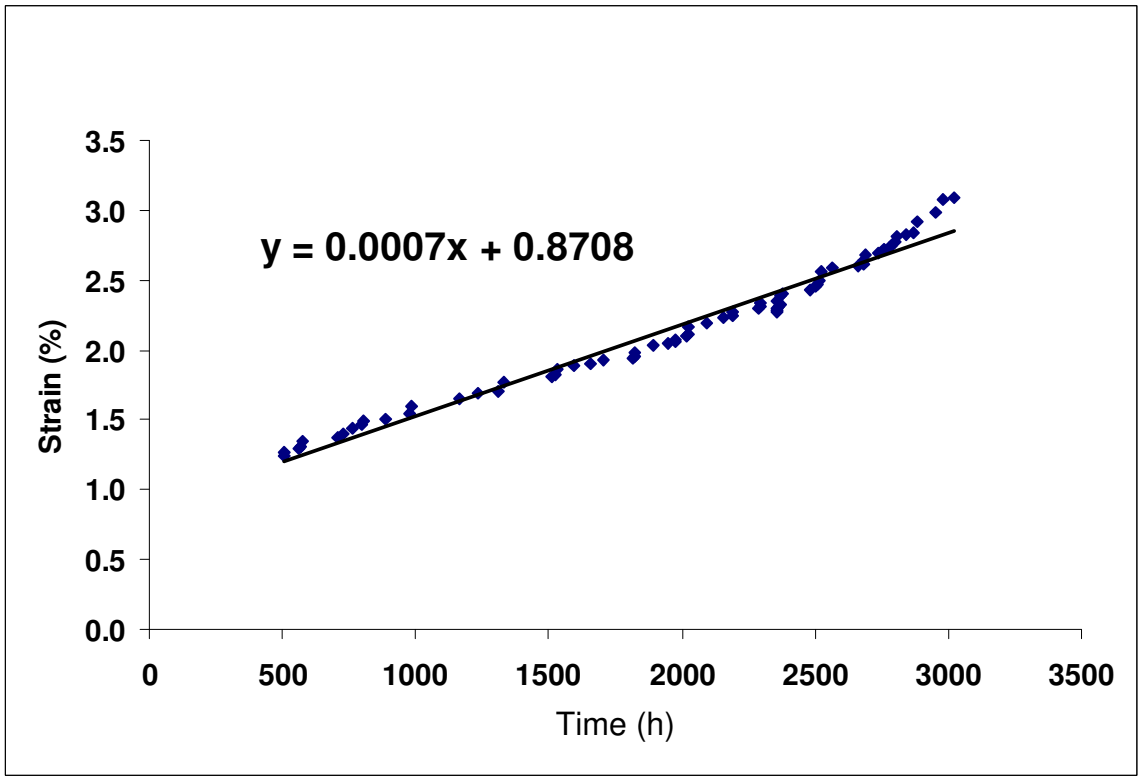

Figure 8-b, Test 5B second stage creep plot.

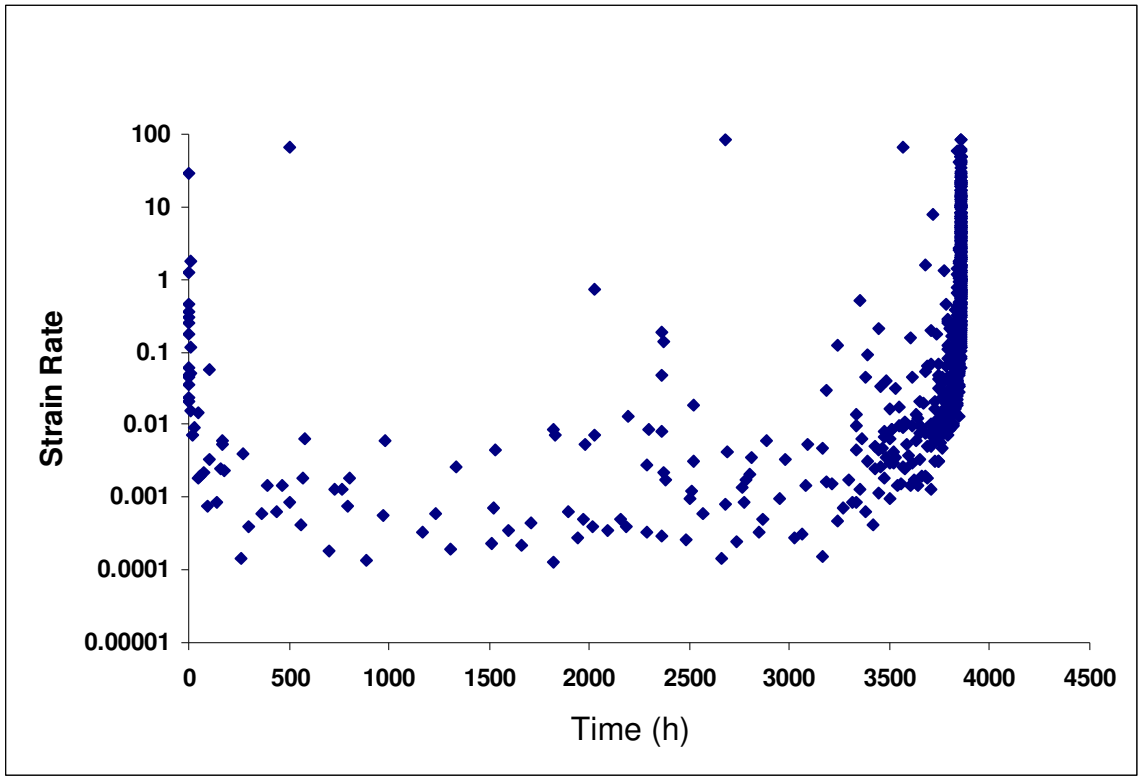

Figure 8-c, Test 5B strain rate plot.

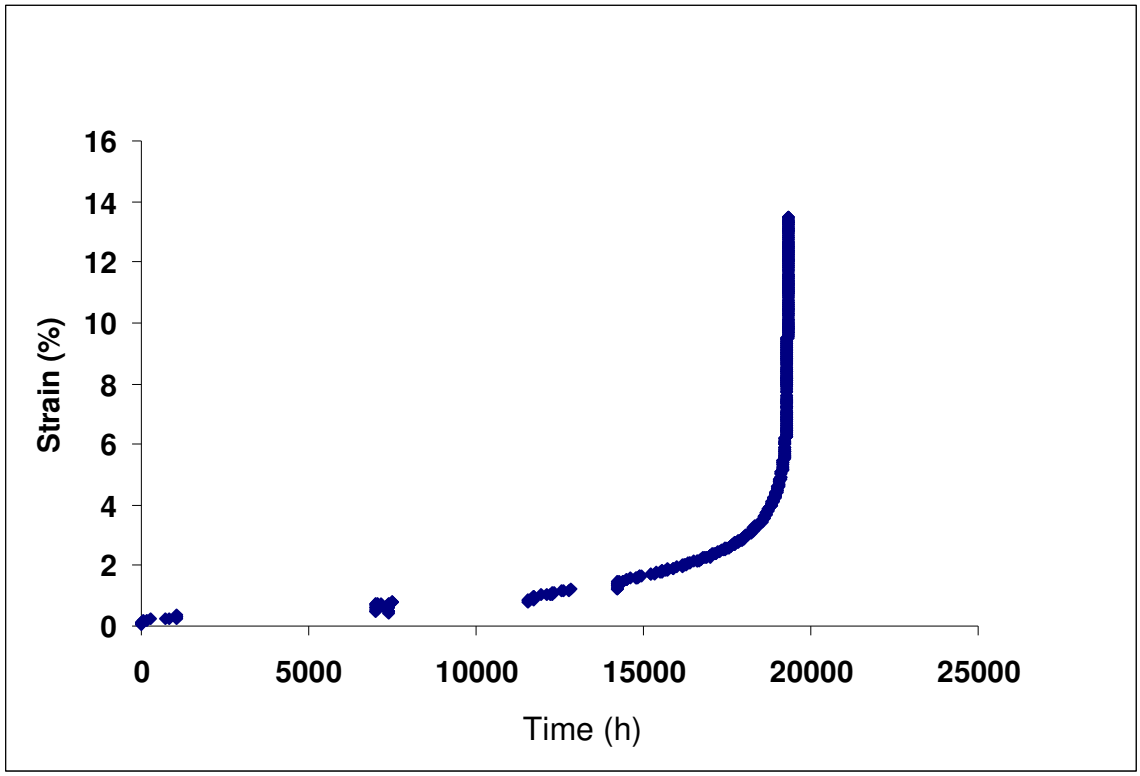

Figure 9-a, Test 9AG, 538°C @ 304.9 MPa.

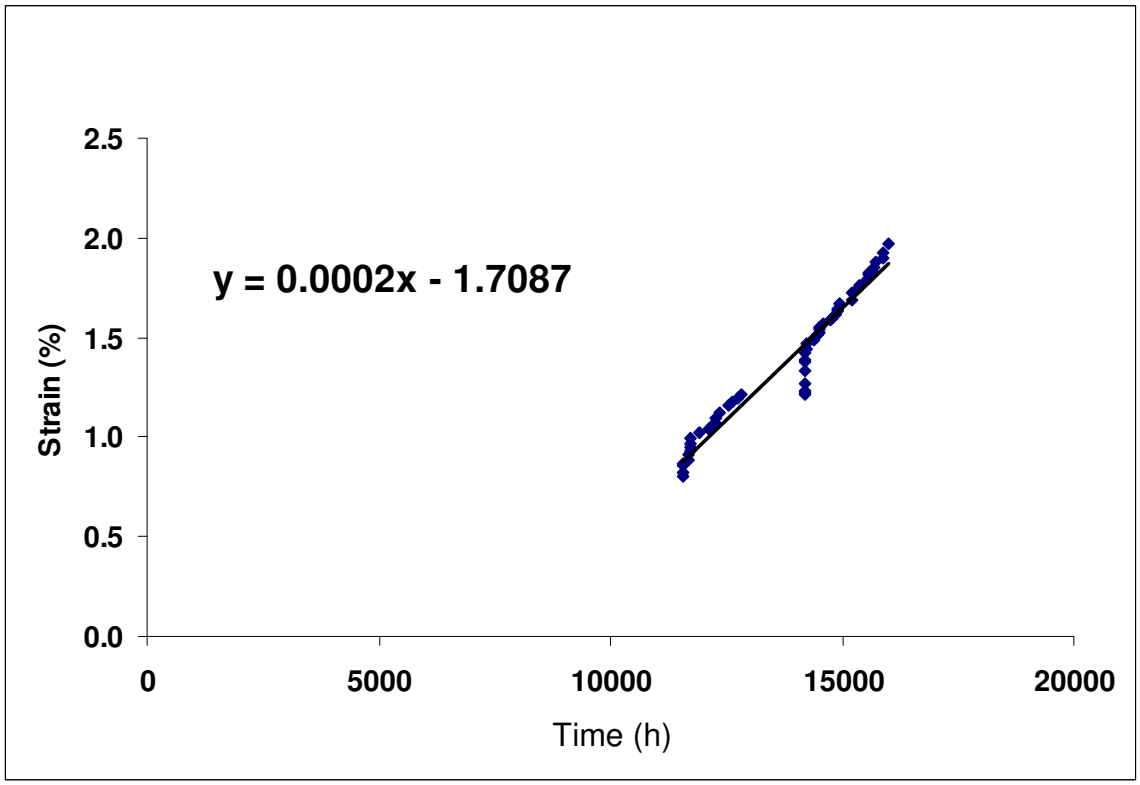

Figure 9-a, Test 9AG second stage creep plot.

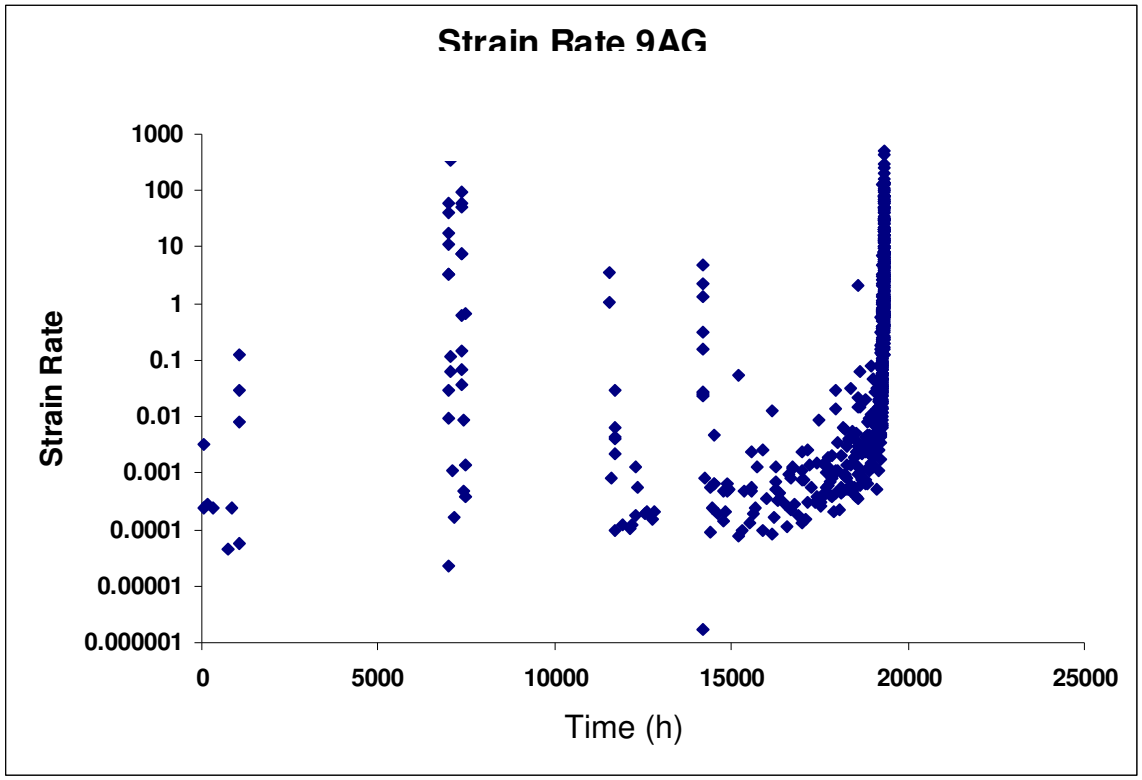

Figure 9-c, Test 9AG strain rate plot.

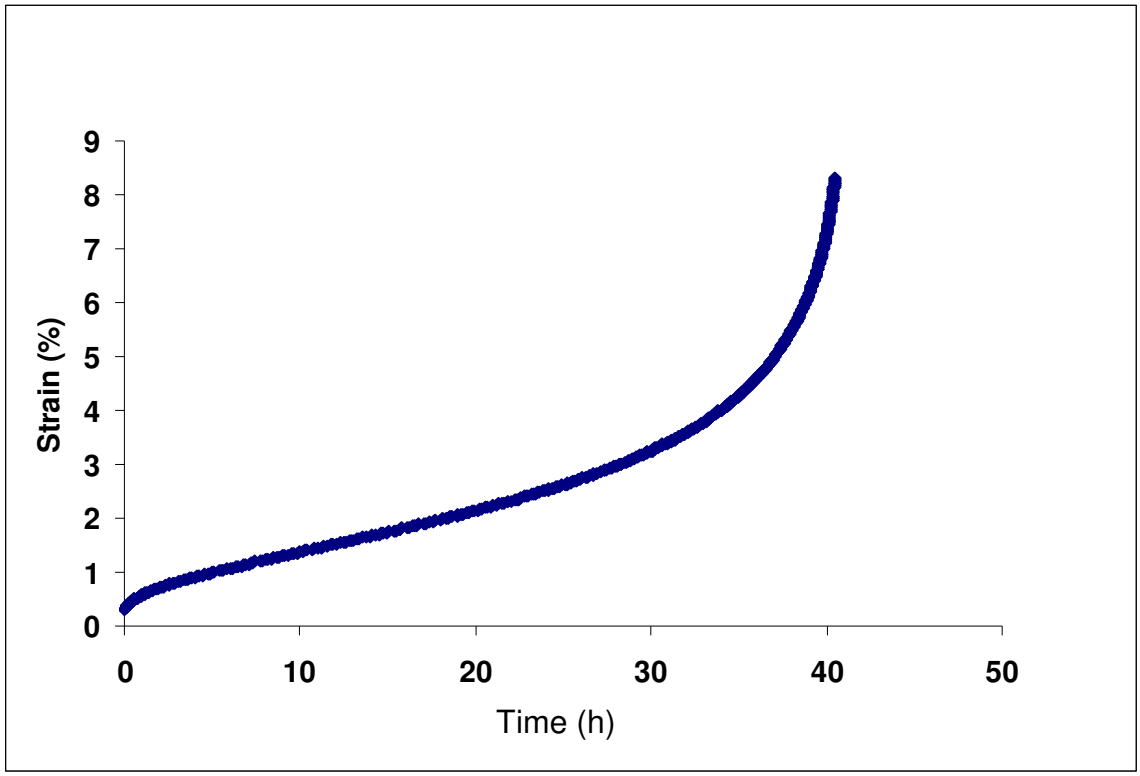

Figure 10-a, Test 9V, 593°C @316.4 MPa.

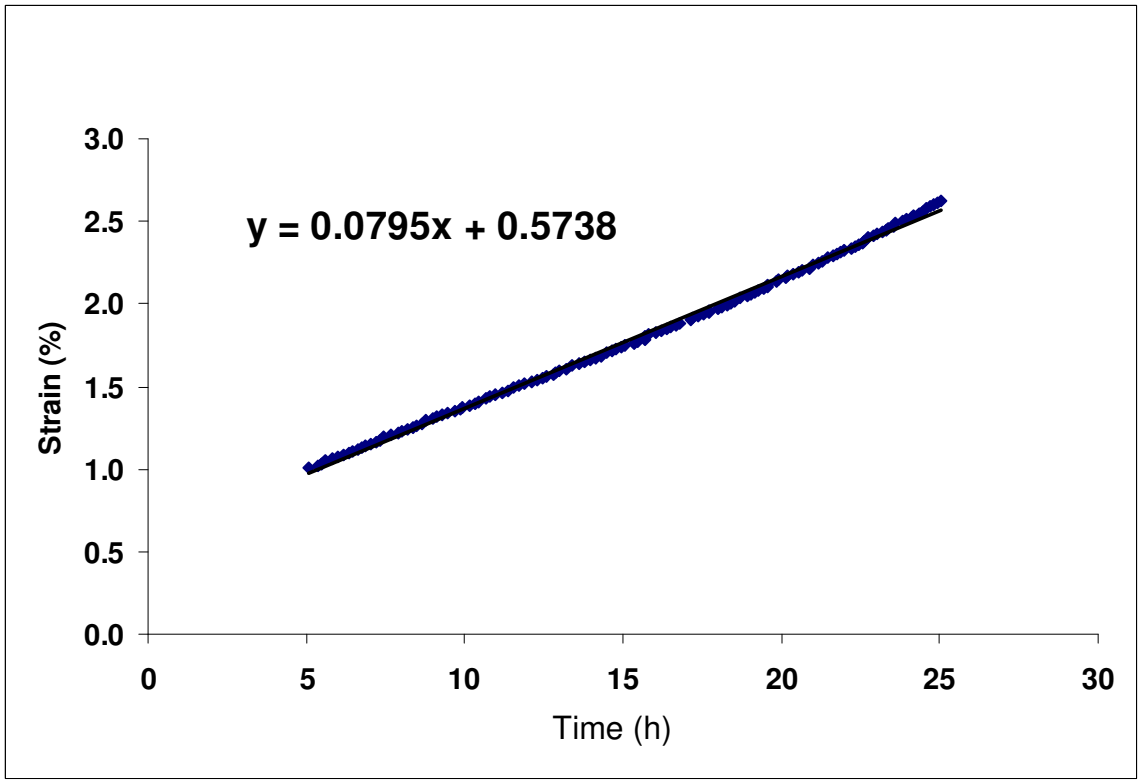

Figure 10-b, Test 9V second stage creep plot.

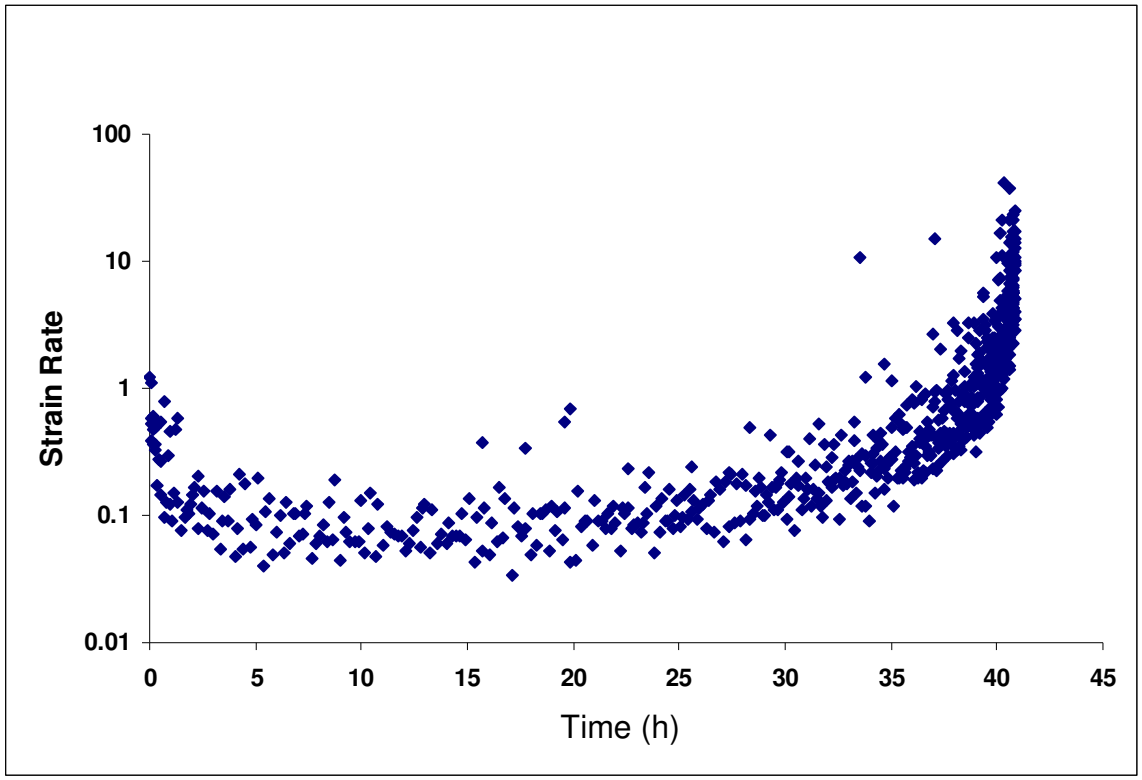

Figure 10-c, Test 9AG strain rate plot.

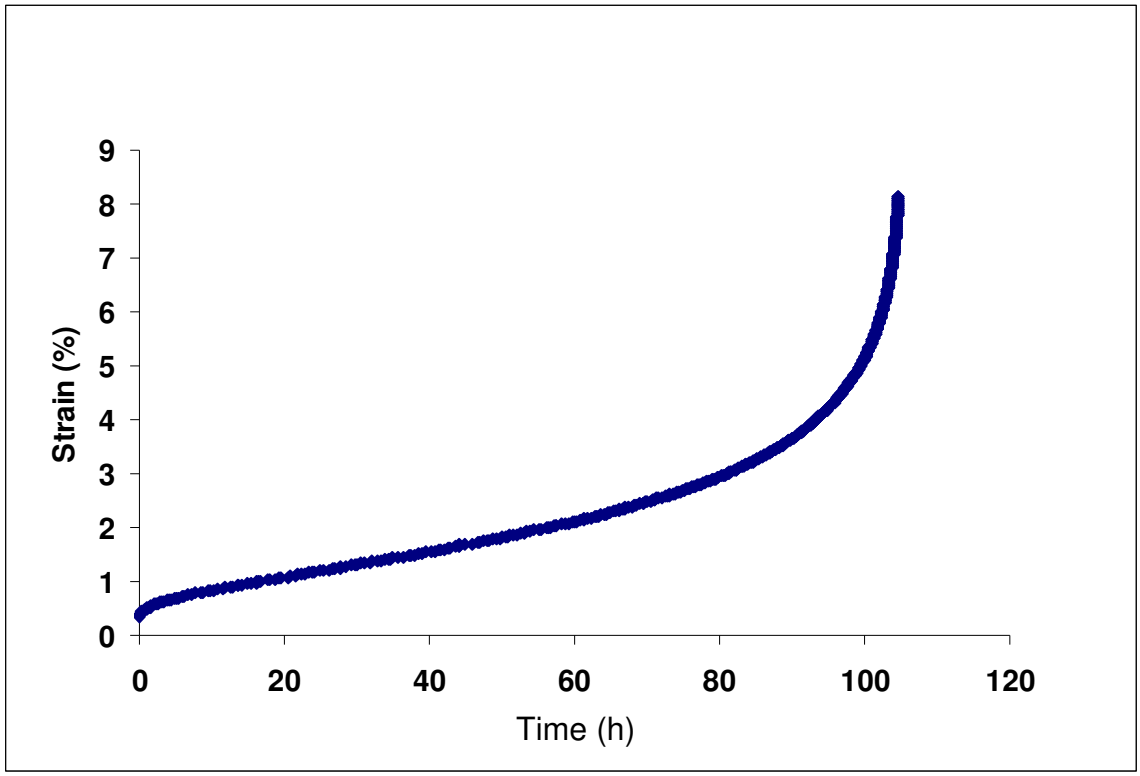

Figure 11-a, Test 9X, 593°C @300.3 MPa.

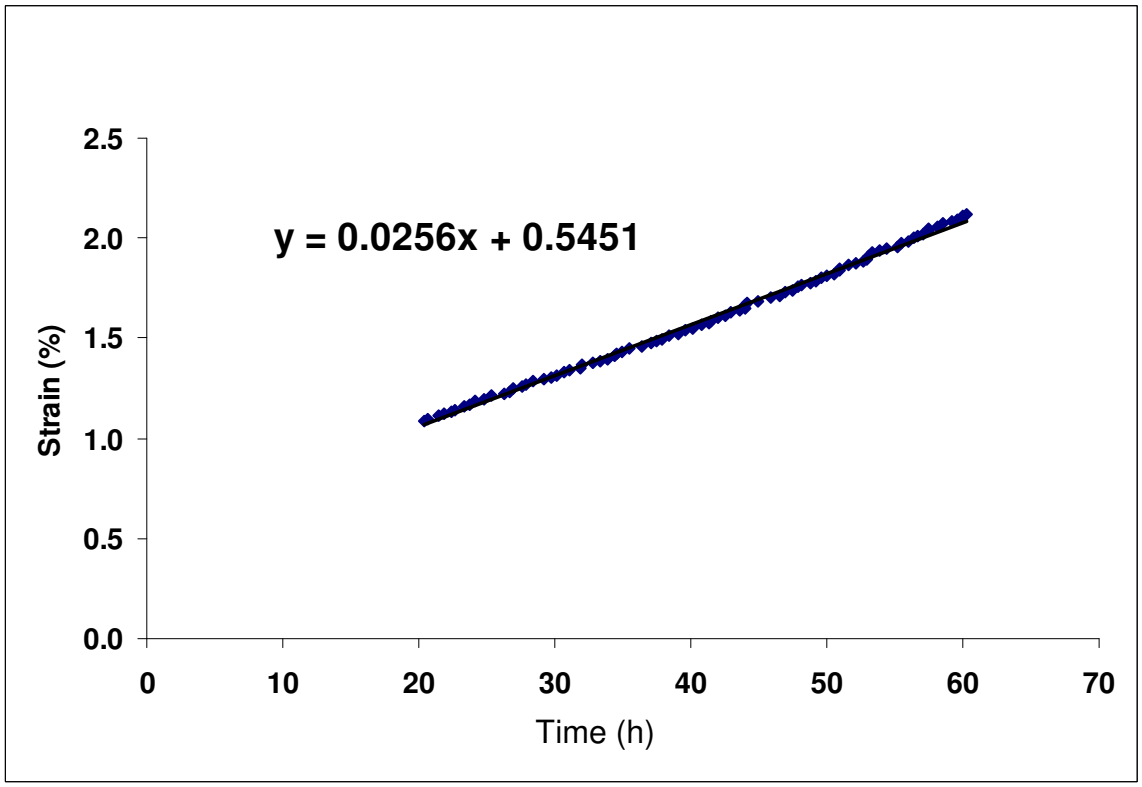

Figure 11-b, Test 9X second stage creep plot.

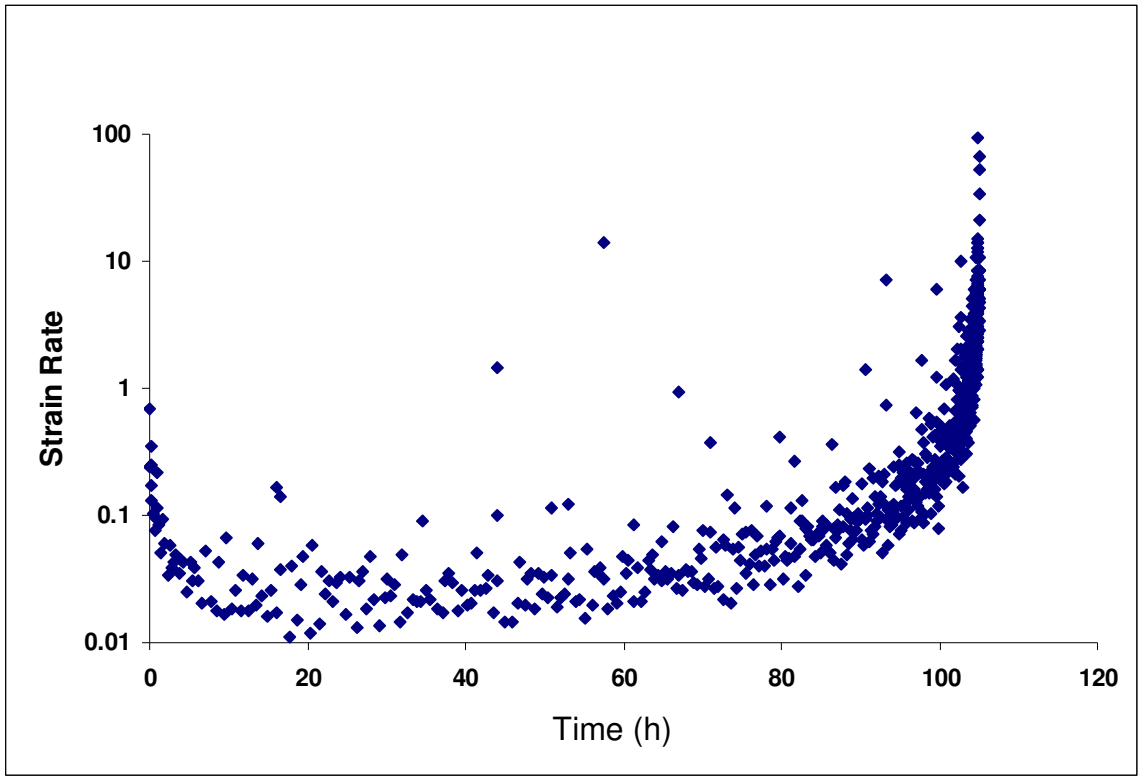

Figure 11-c, Test 9X strain rate plot.

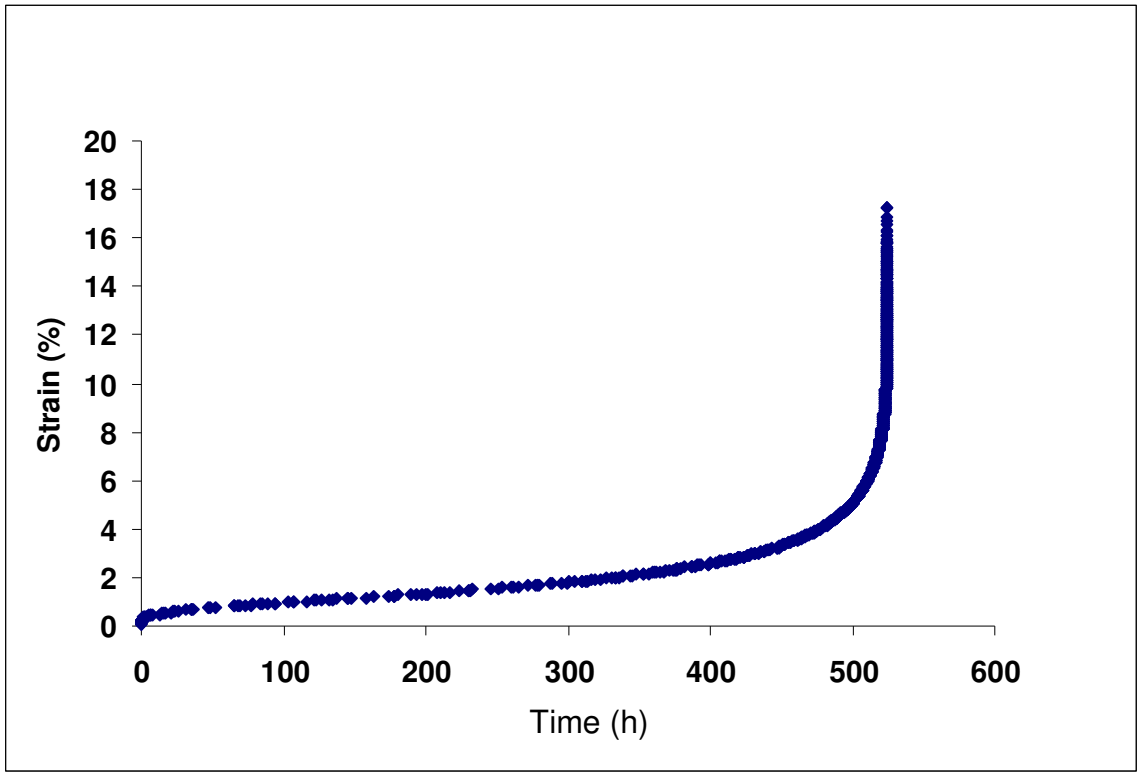

Figure 12-a, Test 4I, 593°C @260.3 MPa.

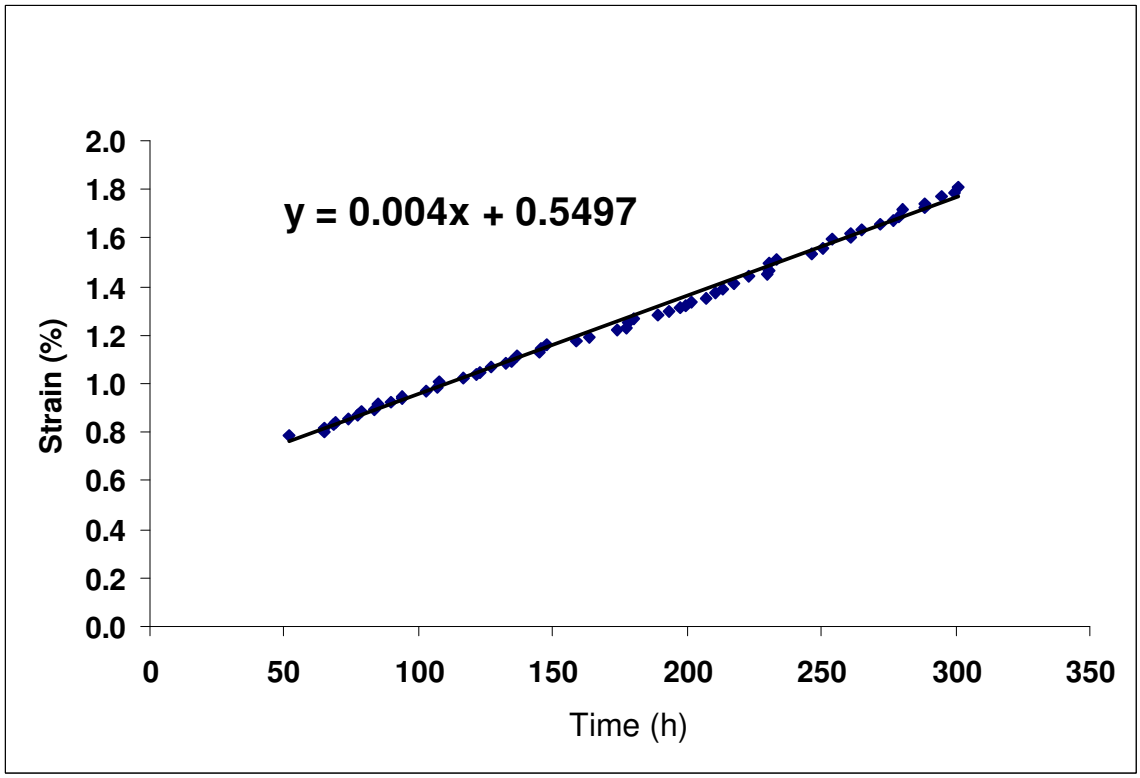

Figure 12-b, Test 4I second stage creep rate.

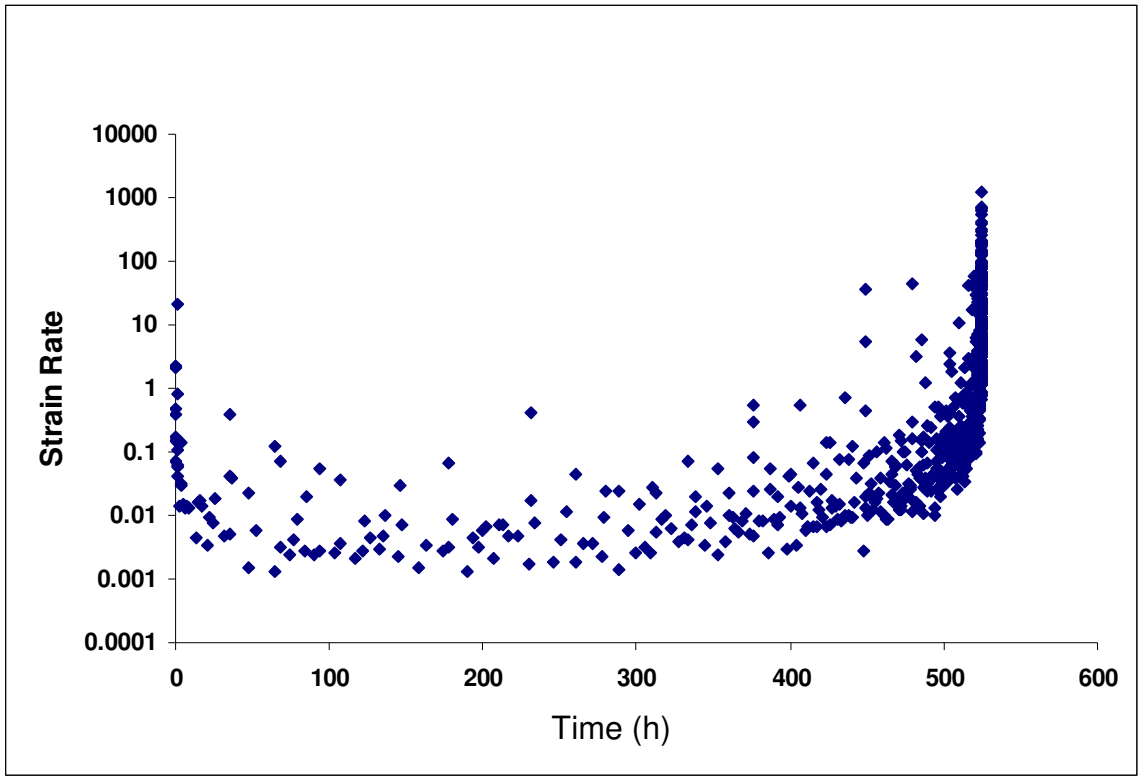

Figure 12-a, Test 4I strain rate plot.

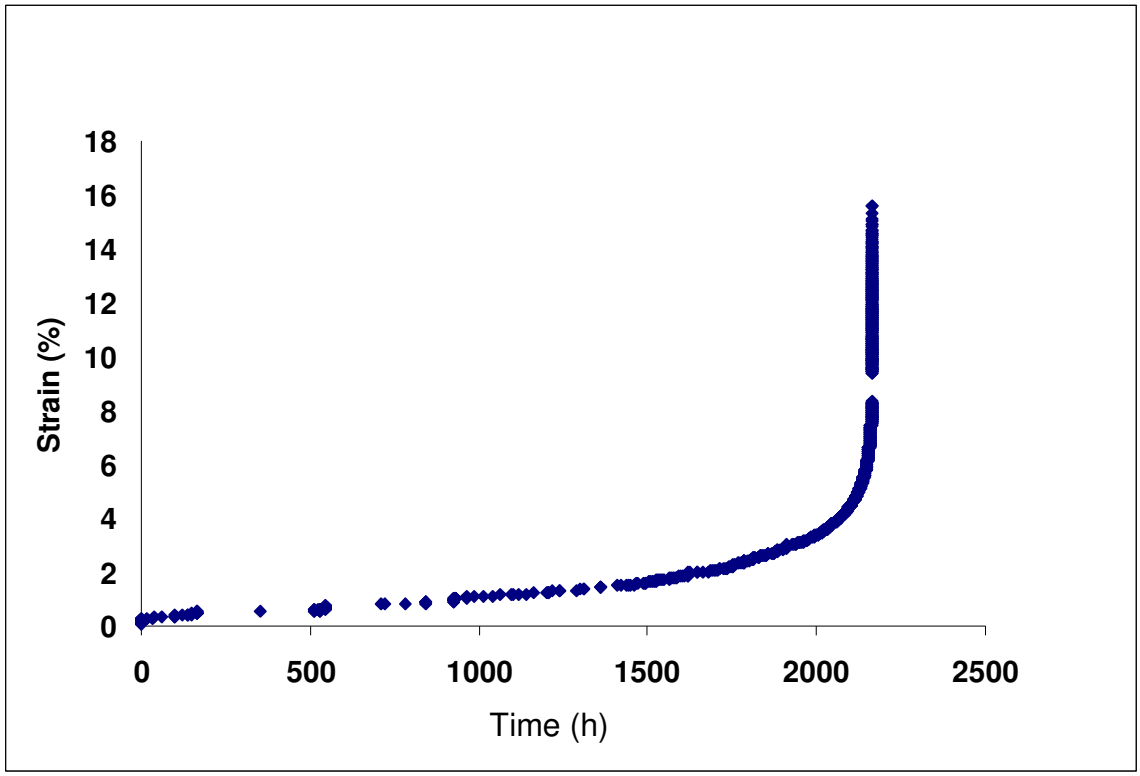

Figure 13-a, Test 9E, 593°C @ 209.6 MPa.

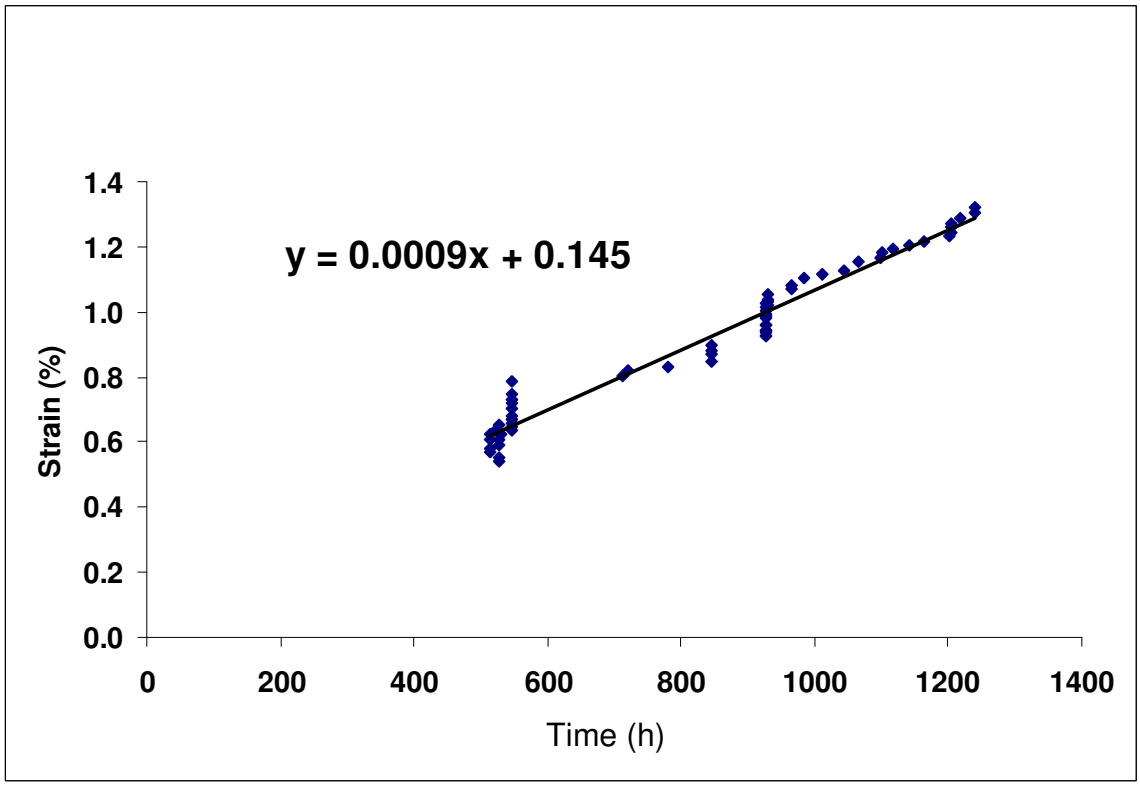

Figure 13-b, Test 9E second stage creep plot.

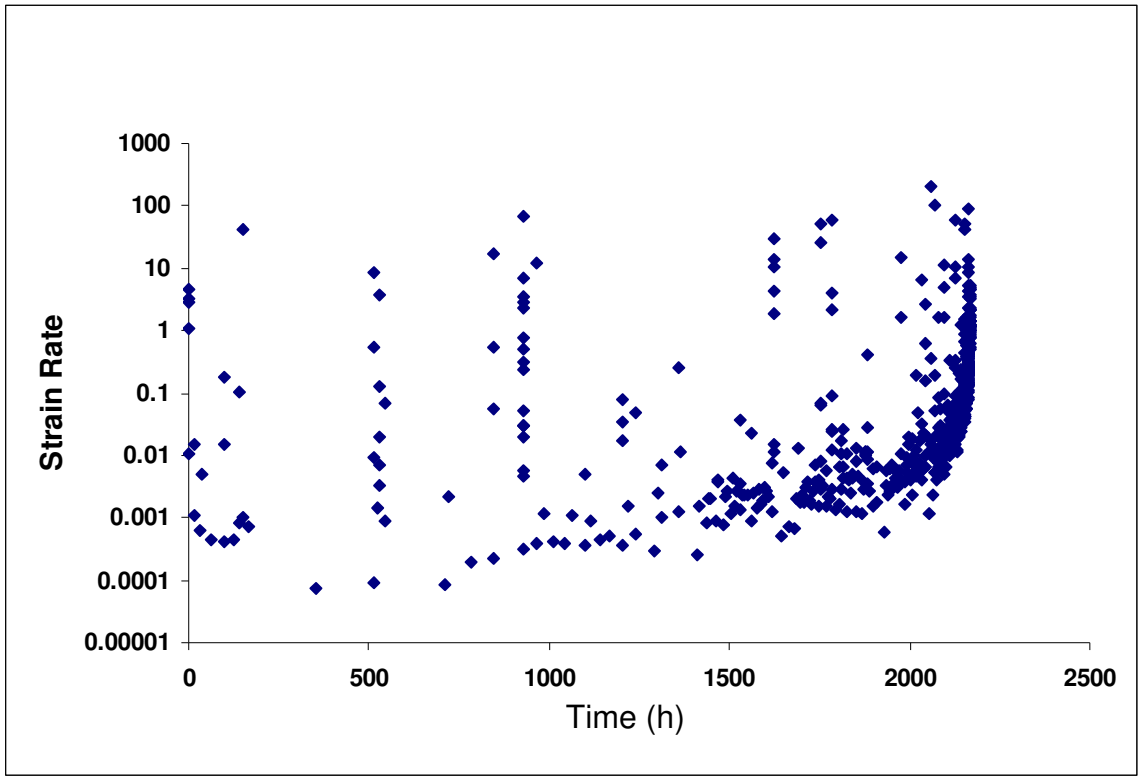

Figure 13-c, Test 9E strain rate plot.

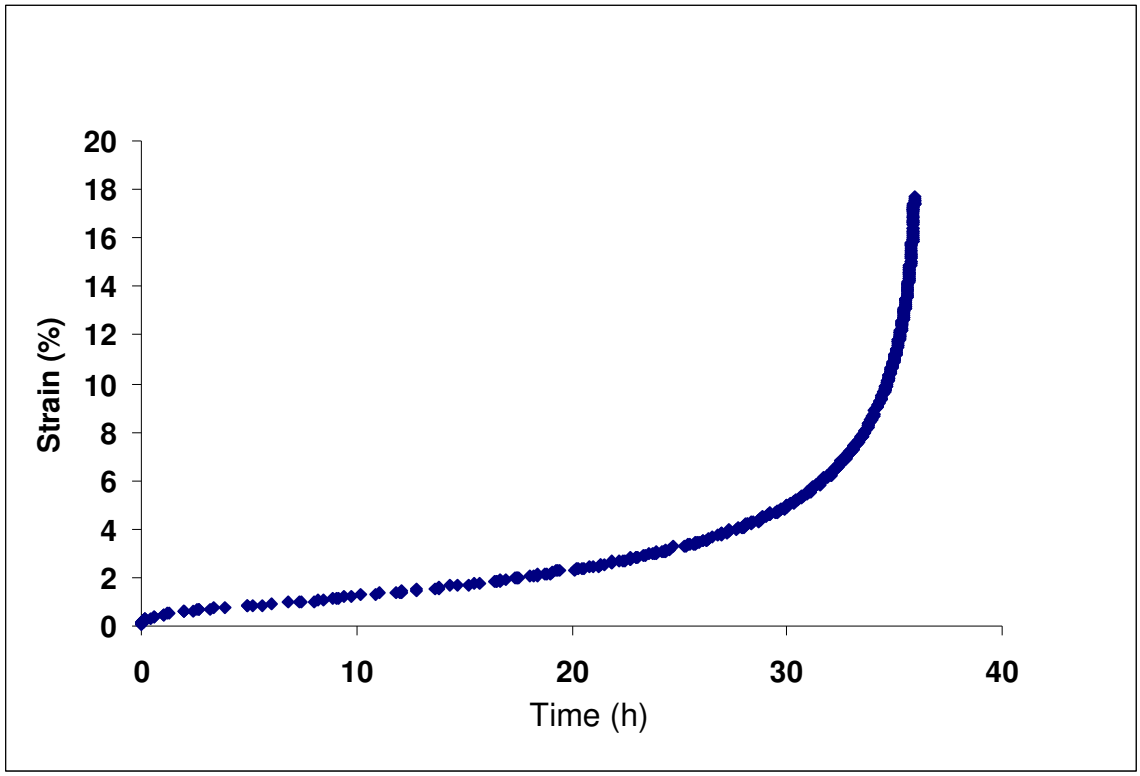

Figure 14-a, Test 5I, 649°C @ 181.7 MPa.

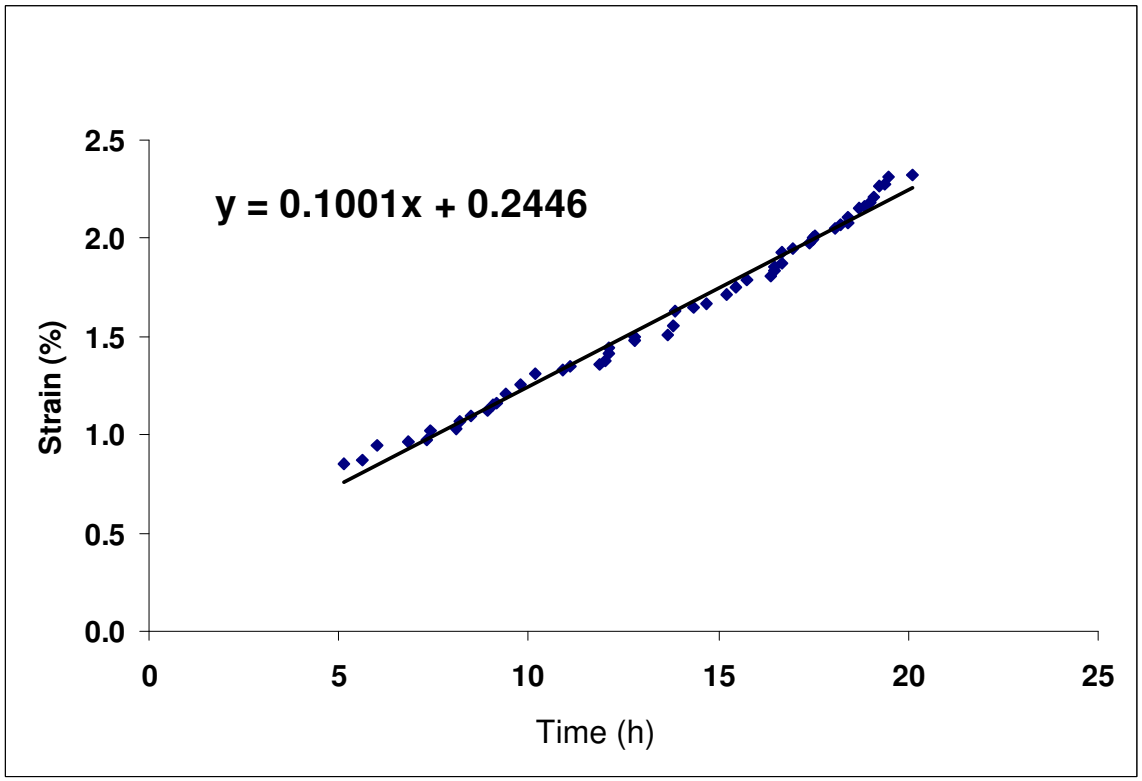

Figure 14-b, Test 5I second stage creep plot.

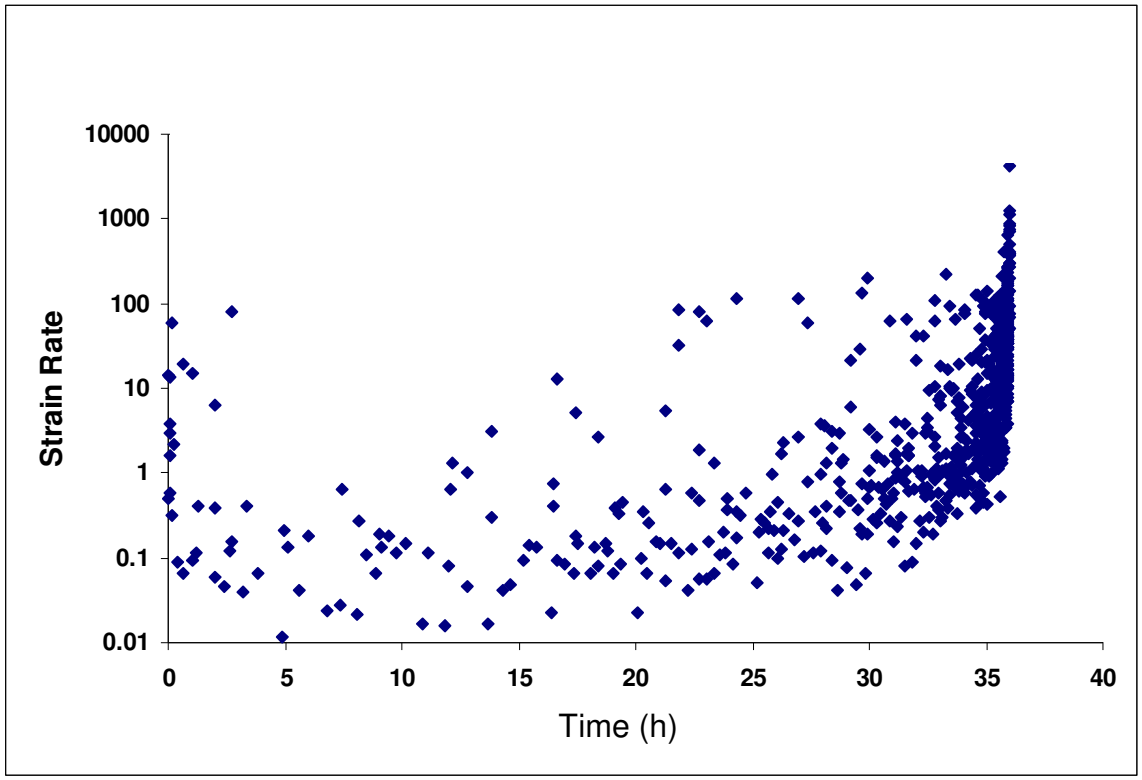

Figure 14-c, Test 5I strain rate plot.

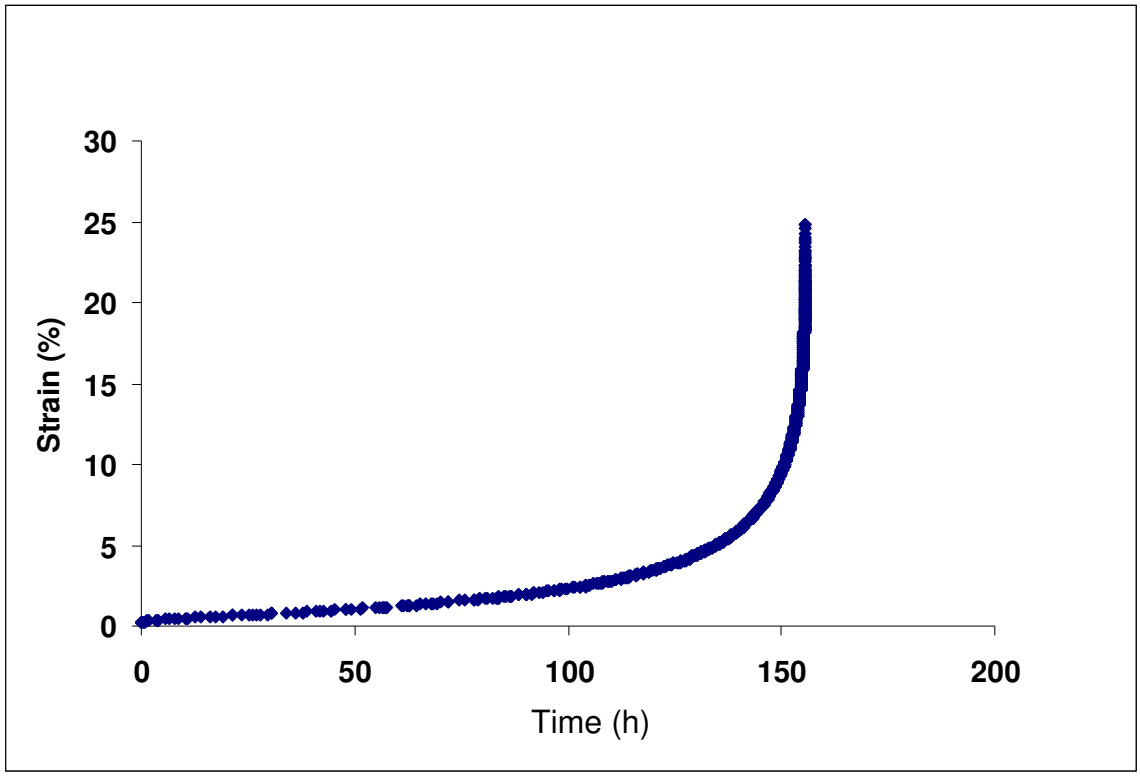

Figure 15-a, Test 4J, 649°C @ 139.7 MPa.

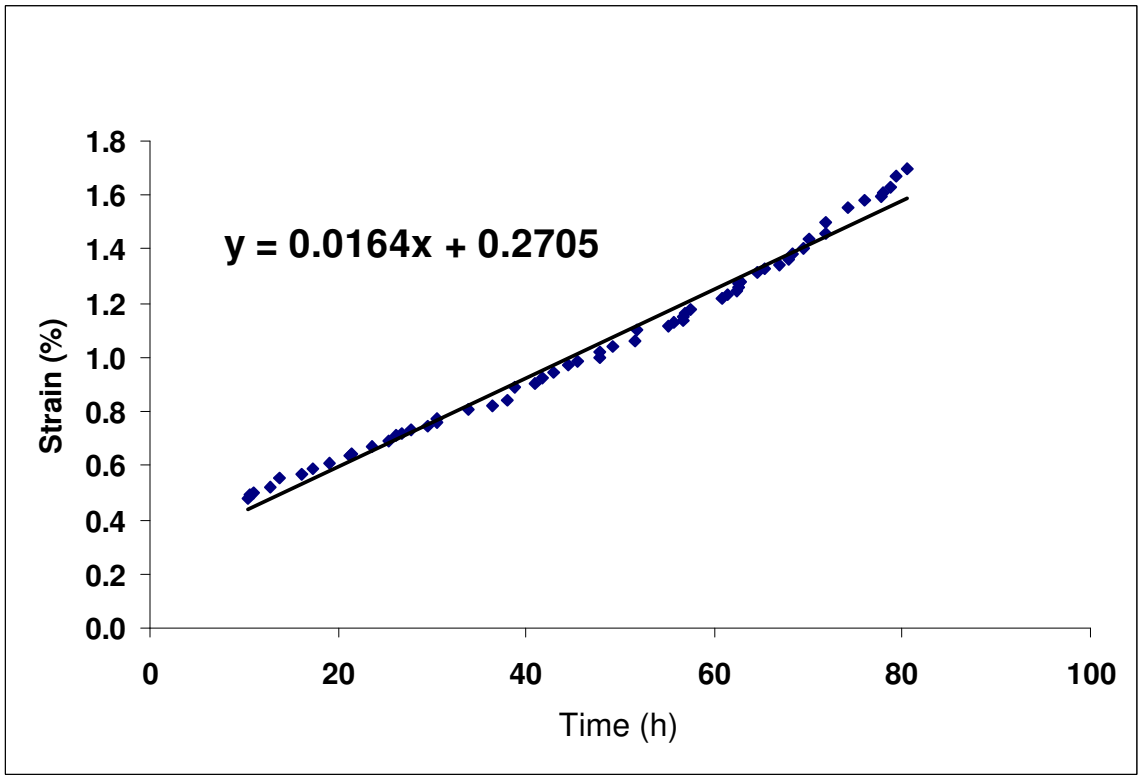

Figure 15-b, Test 4J second stage creep plot.

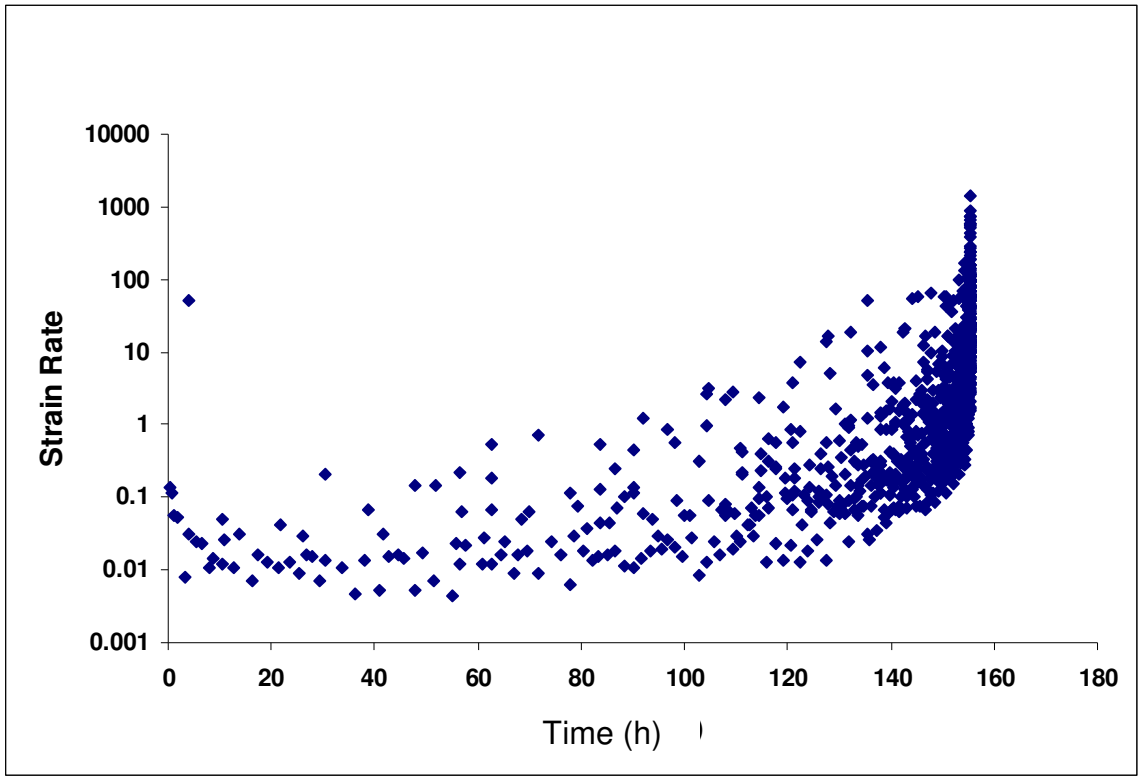

Figure 15-c, Test 4J strain rate plot.

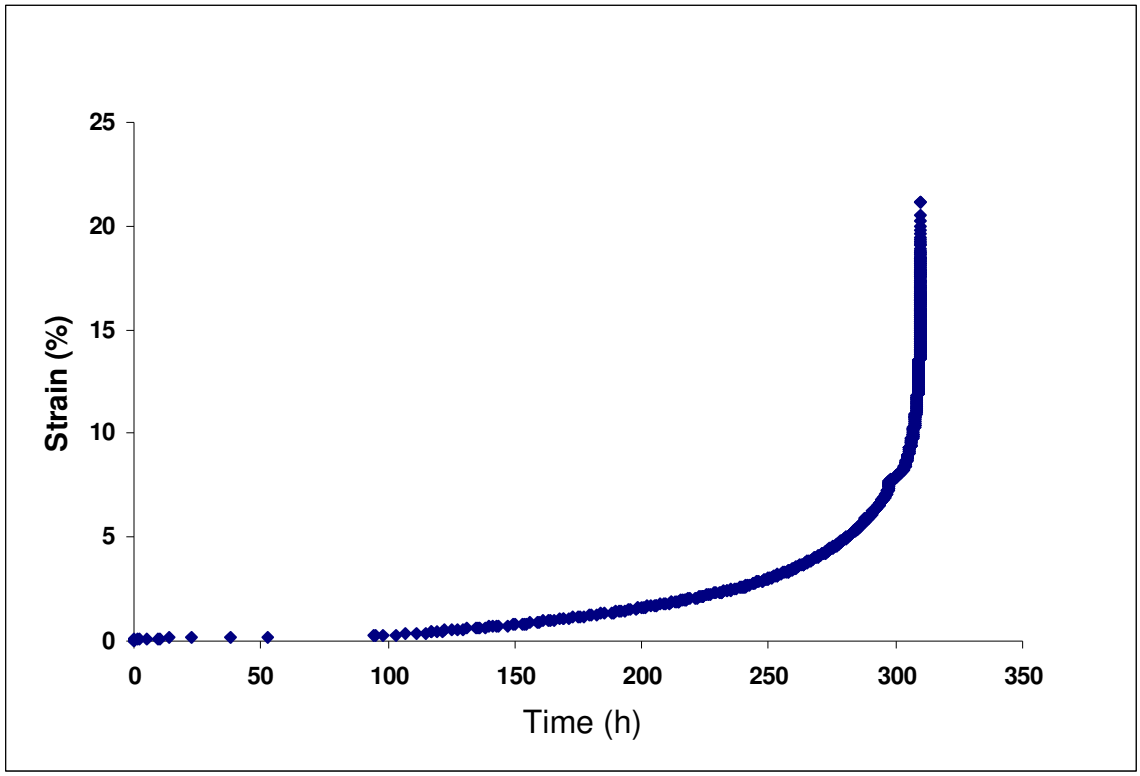

Figure 16-a, Test 9P, 649°C @ 129.6 MPa.

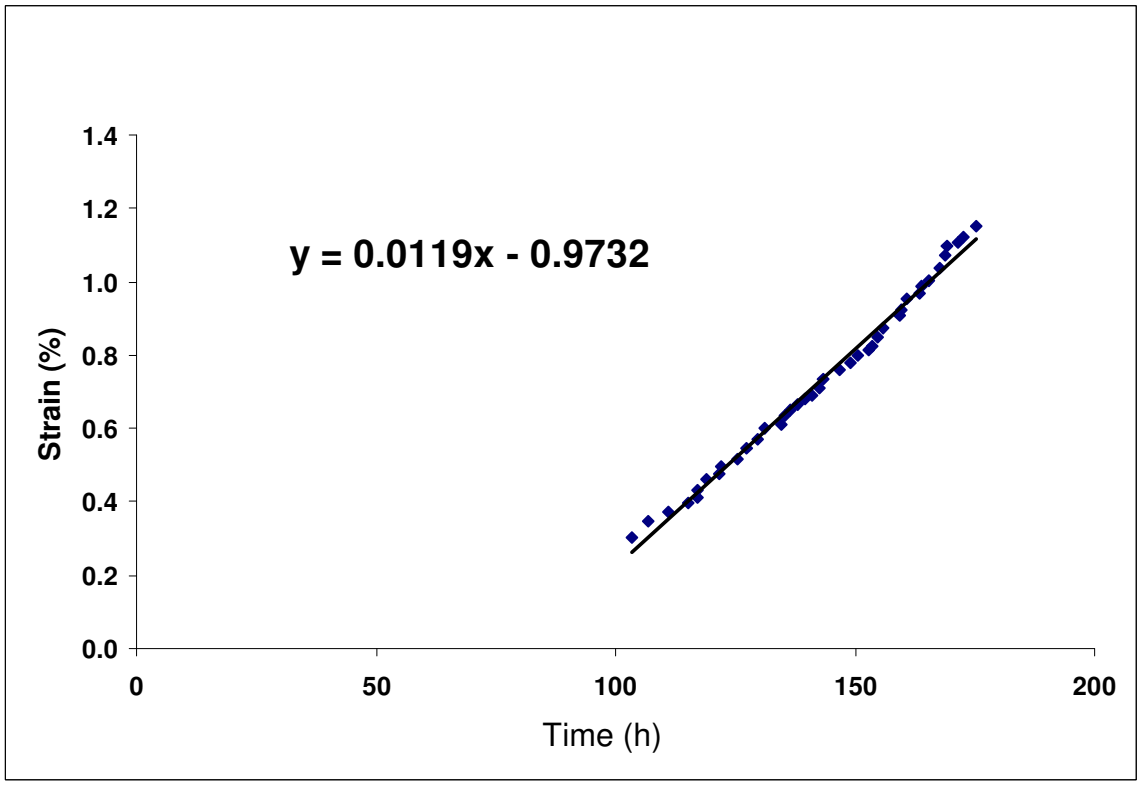

Figure 16-b, Test 9P second stage creep plot.

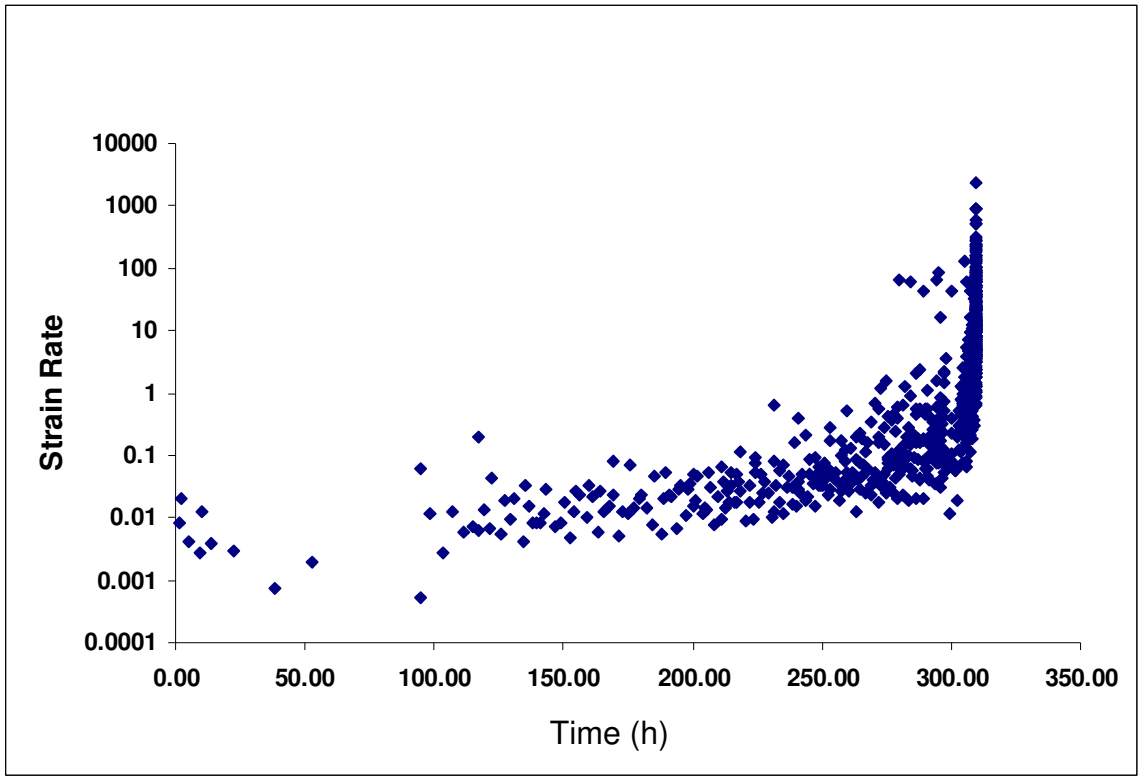

Figure 16-c, Test 9P strain rate plot.

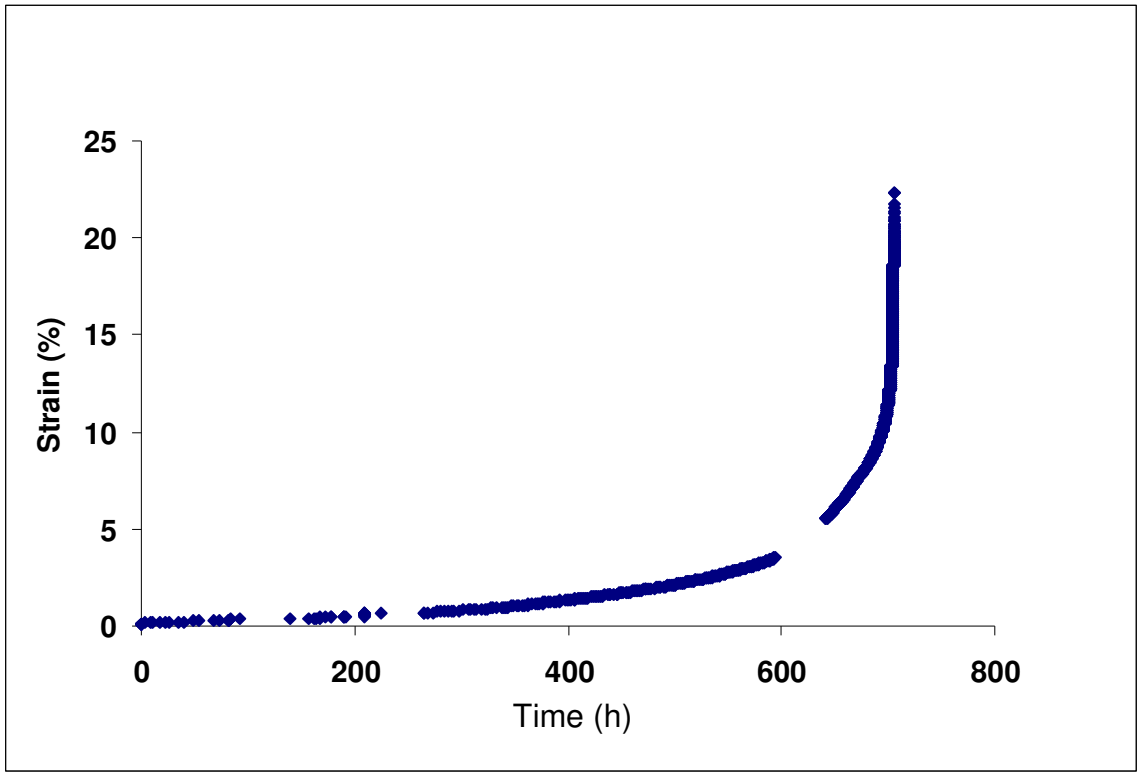

Figure 17-a, Test 9H, 649°C 131.3 MPa.

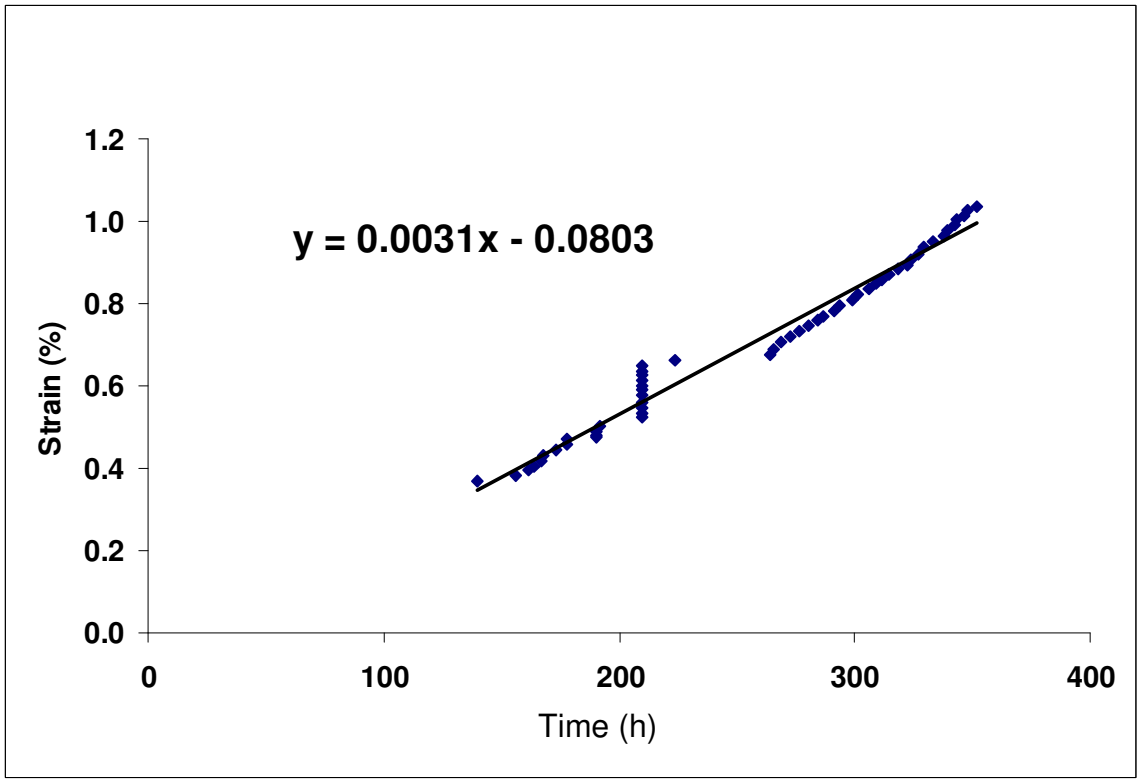

Figure 17-b, Test 9H second stage creep plot.

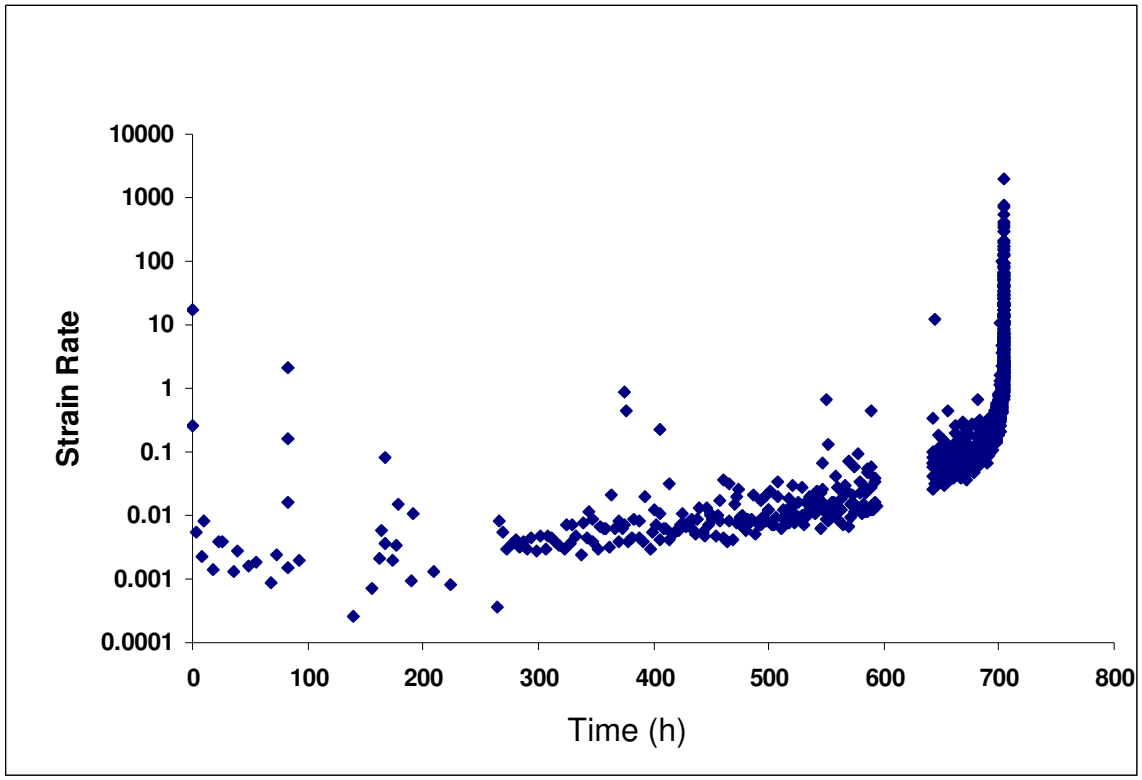

Figure 17-c, Test 9H strain rate plot.

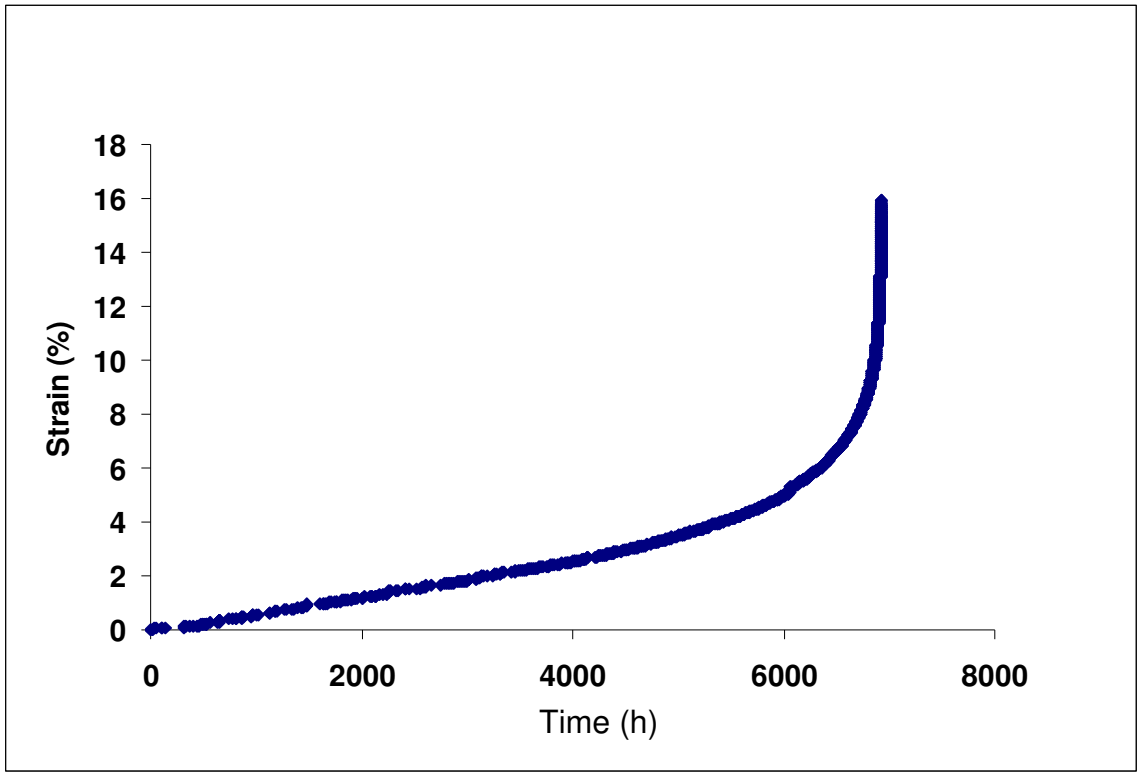

Figure 18-a, Test 9W, 649°C @ 69 MPa.

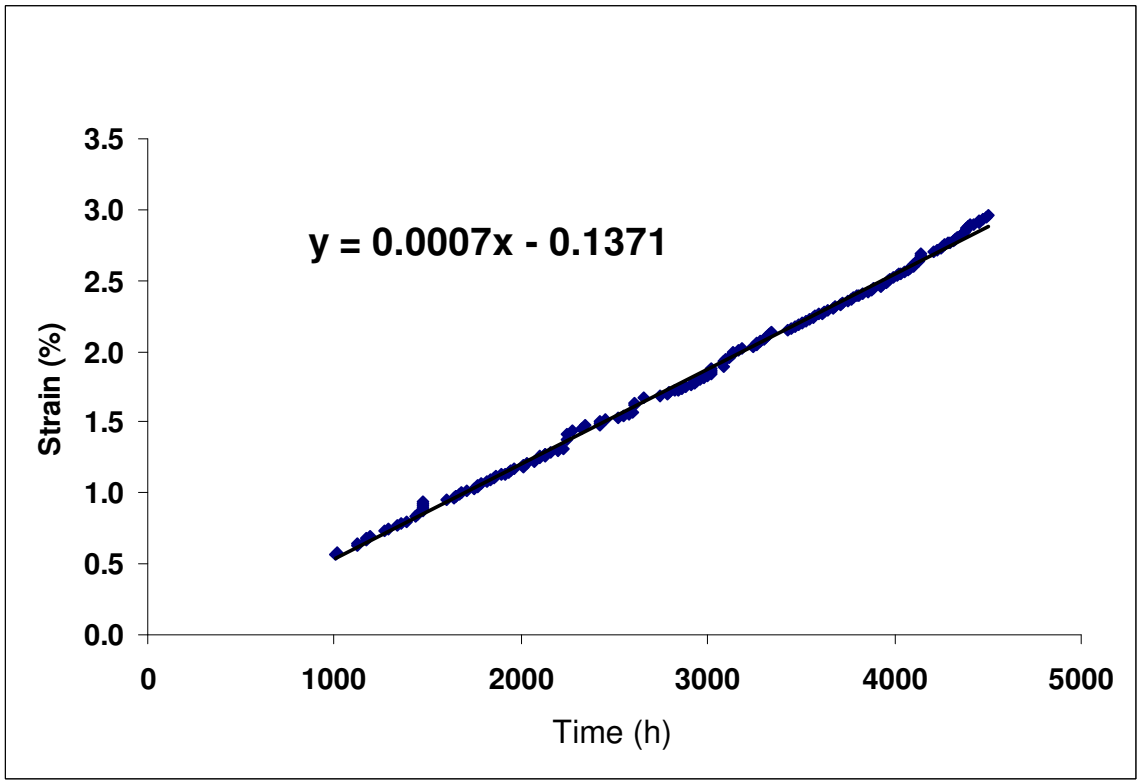

Figure 18-b, Test 9W second stage creep plot.

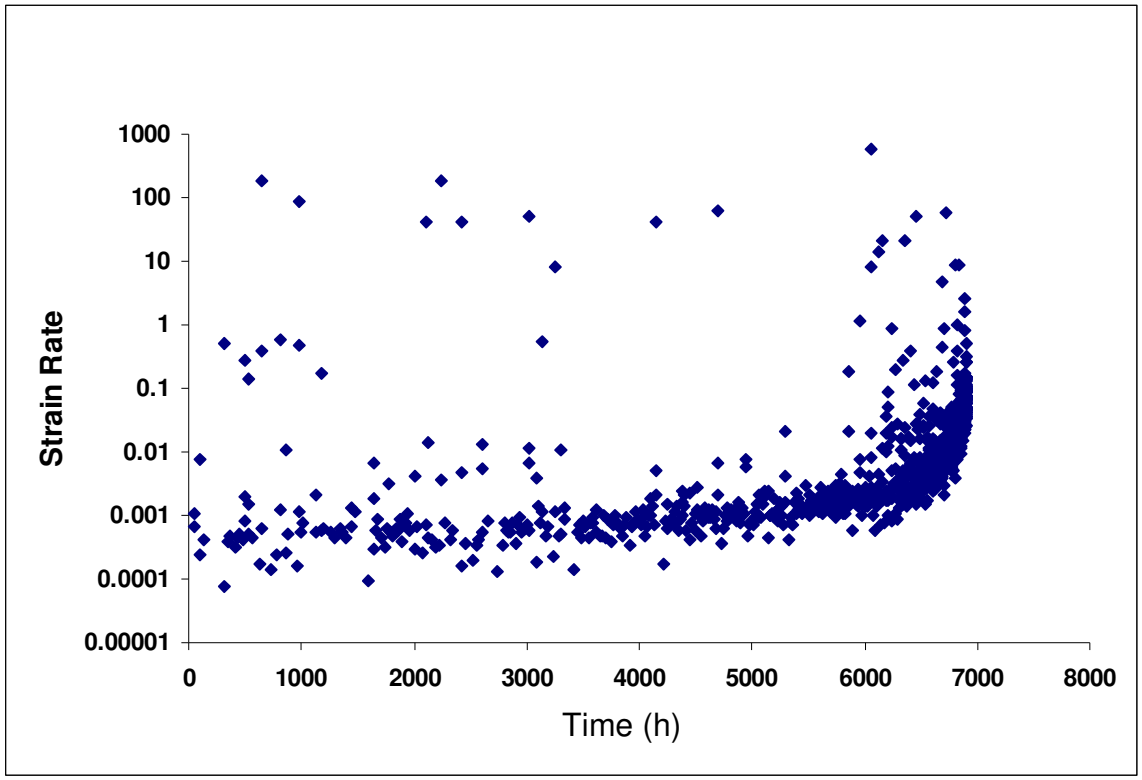

Figure 18-c, Test 9W strain rate plot.

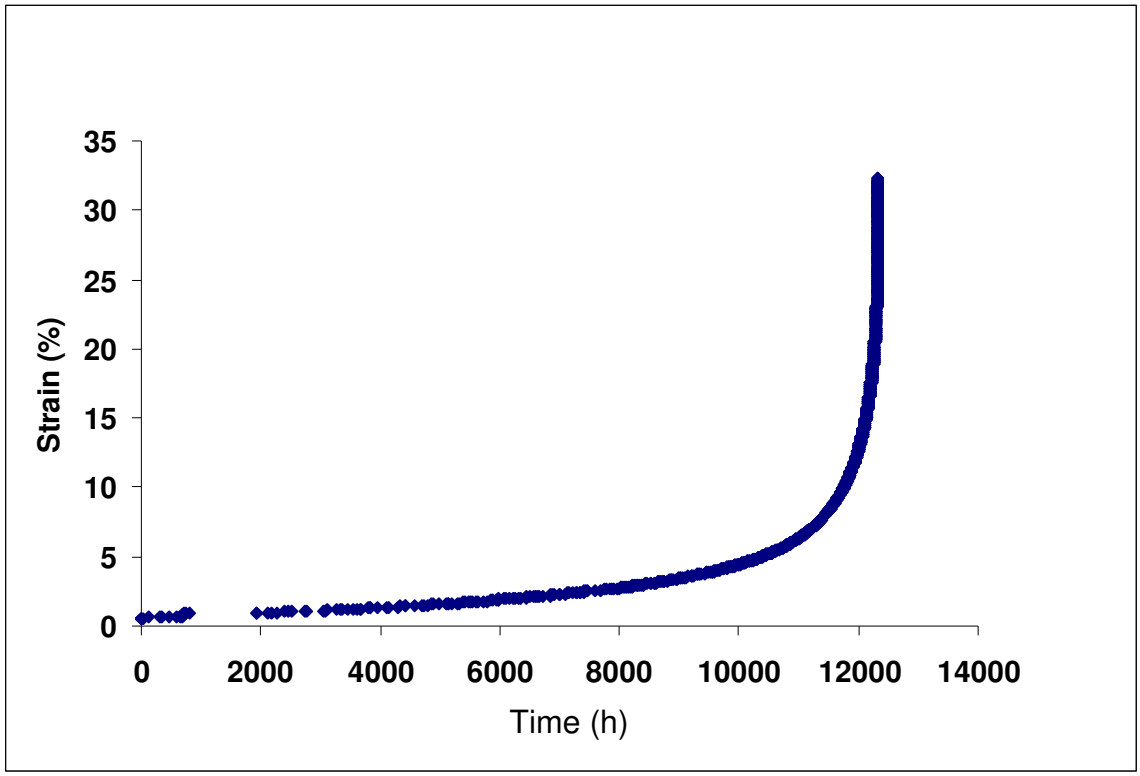

Figure 19-a, Test 4M, 649°C @ 50.2 MPa.

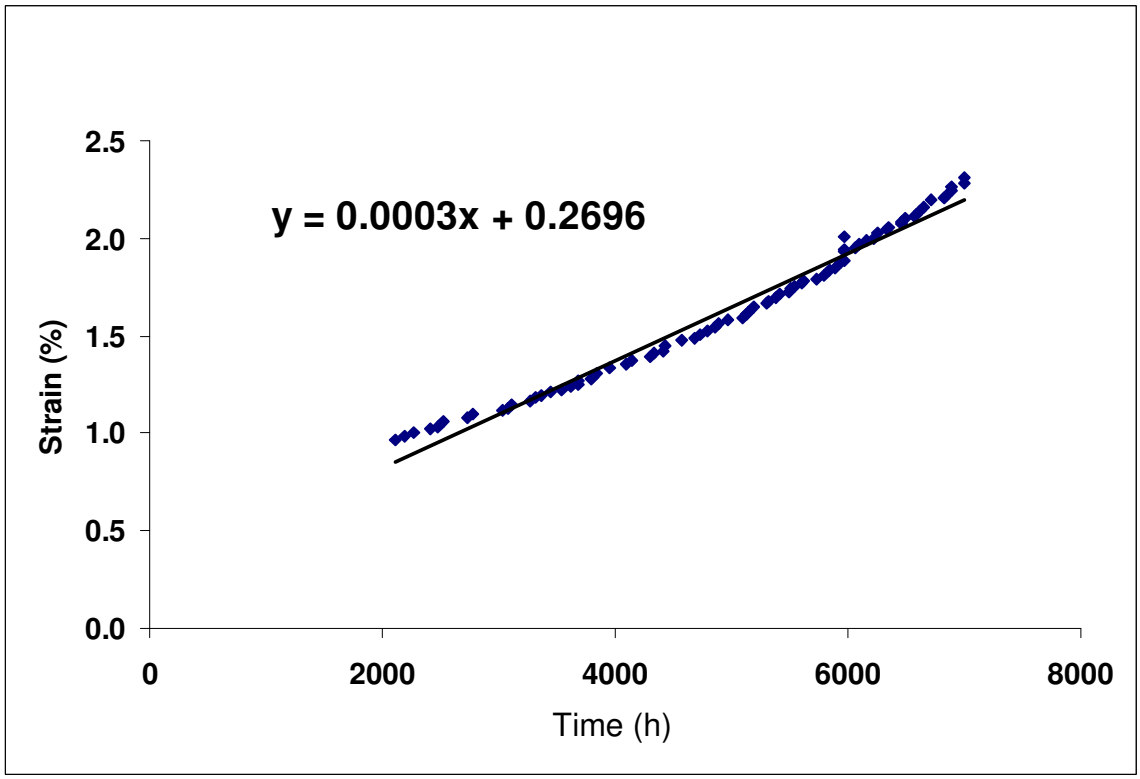

Figure 19-b, Test 4M second stage creep plot.

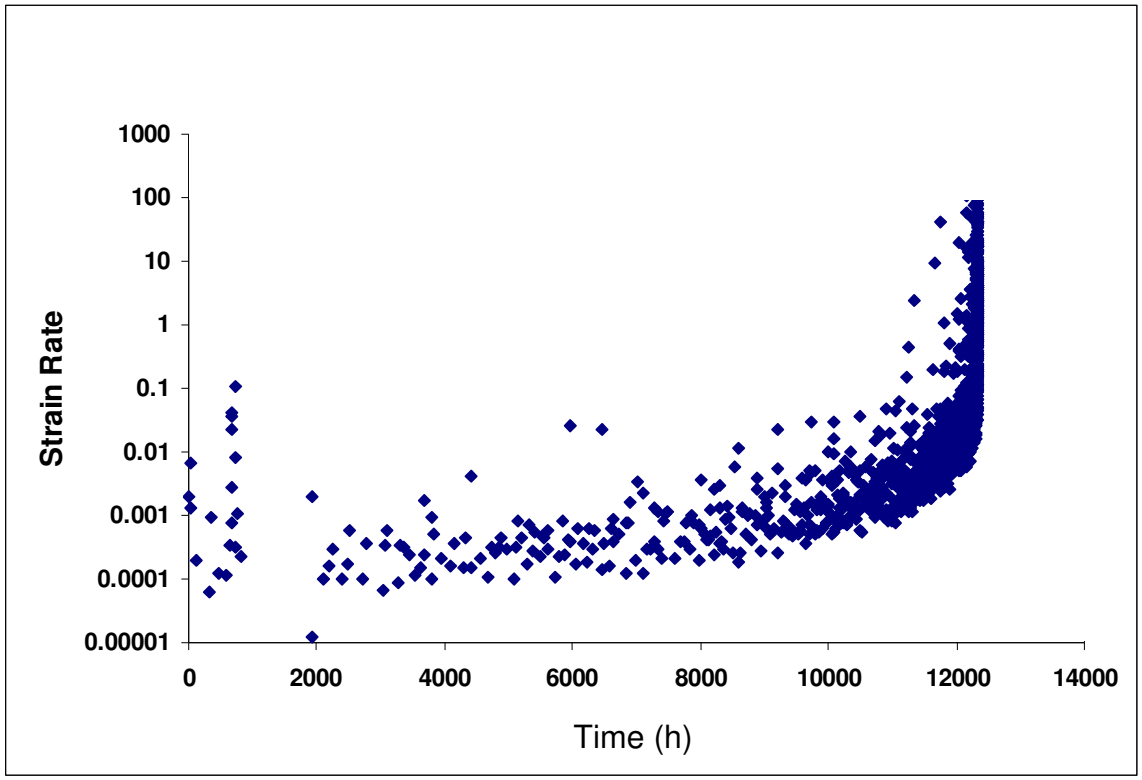

Figure 19-c, Test 4M strain rate plot.

Appendix B

Calculation of an empirically derived formula relating steady state strain to creep stress and temperature:

From figure 4-4, it appears that steady state strain rate can be described by the following stress function,

$$\dot{\varepsilon}_{ss} = X \exp[Y\sigma] \quad \text{Equation (B1)}$$

Where: **σ** is stress in MPa,
Y is a material constant

The function X, appears to be a power driven function dependant on temperature taking the following form,

$$X = \left(\frac{C}{T}\right)^n \quad \text{Equation (B2)}$$

Where: **T** is the absolute temperature in Kelvin,
n is a material constant and,
C is activation energy constant

From figure 4-4, the following data is taken,

At 538°C (811.15K)

$$\left(\frac{C}{T}\right)^n = 5.94x10^{-10}$$

$$Y = 0.044 \quad \text{Equation (B3)}$$

At 593°C (866.15K)

$$\left(\frac{C}{T}\right)^n = 1.47x10^{-7}$$

$$Y = 0.041 \quad \text{Equation (B4)}$$

At 649°C (922.15K)

$$\left(\frac{C}{T}\right)^n = 3.03x10^{-5}$$

$$Y = 0.044 \quad \text{Equation (B5)}$$

Entering in temperature allows a two variable equation based upon *C* and *n* to be determined for each set of testing temperatures.

649°C:

$$3.03x10^{-5} = \left[\frac{C}{922.15}\right]^{n}$$

$$\log\left(3.03x10^{-5}\right) = n\left(\log(C) - \log(922.15)\right)$$

$$n = \frac{\log\left(3.03x10^{-5}\right)}{\log(C) - \log(922.15)} \quad \text{Equation (B6)}$$

593°C:

$$\log\left(1.47x10^{-7}\right) = n\left(\log(C) - \log(866.15)\right)$$

$$n = \frac{\log\left(1.47x10^{-7}\right)}{\log(C) - \log(866.15)} \quad \text{Equation (B7)}$$

538°C:

$$\log\left(5.94x10^{-10}\right) = n\left(\log(C) - \log(811.15)\right)$$

$$n = \frac{\log\left(5.94x10^{-10}\right)}{\log(C) - \log(811.15)} \quad \text{Equation (B8)}$$

Solving for *n* and *C* at different temperatures reveals the following:

$$\frac{\log\left(3.03x10^{-5}\right)}{\log C-\log(922.15)}=\frac{\log\left(5.94x10^{-10}\right)}{\log C-\log(811.15)}$$

$$\log C=\frac{\log\left(3.03x10^{-5}\right)\cdot\log(811.15)-\log\left(5.94x10^{-10}\right)\cdot\log(922.15)}{\log\left(3.03x10^{-5}\right)-\log\left(5.94x10^{-10}\right)}$$

$$\log C=3.0183$$

C = 1042.95 649°C ⇔ 538°C _____ Equation (B9)

$$\frac{\log\left(3.03x10^{-5}\right)}{\log C-\log(922.15)}=\frac{\log\left(1.47x10^{-7}\right)}{\log C-\log(866.15)}$$

$$\log C=\frac{\log\left(3.03x10^{-5}\right)\cdot\log(866.15)-\log\left(1.47x10^{-7}\right)\cdot\log(922.15)}{\log\left(3.03x10^{-5}\right)-\log\left(1.47x10^{-7}\right)}$$

$$\log C=3.0179$$

C = 1042.15 649°C ⇔ 593°C _____ Equation (B10)

$$\frac{\log\left(1.47x10^{-7}\right)}{\log C-\log(866.15)}=\frac{\log\left(5.94x10^{-10}\right)}{\log C-\log(811.15)}$$

$$\log C=\frac{\log\left(1.47x10^{-7}\right)\cdot\log(811.15)-\log\left(5.94x10^{-10}\right)\cdot\log(866.15)}{\log\left(1.47x10^{-7}\right)-\log\left(5.94x10^{-10}\right)}$$

$$\log C=3.0189$$

C = 1044.55 593°C ⇔ 538°C _____ Equation (B11)

Average = 1043

St.Dev. = 1.2

The results have a standard deviation less than one percent, so the average of the three results is then used to solve for the exponential constant, *n*.

$$n = \frac{\log\left(5.94x10^{-10}\right)}{\log(1043) - \log(811.15)}$$

$$= \mathbf{-84.502 @ 538°C} \qquad \text{Equation (B12)}$$

$$n = \frac{\log\left(1.47x10^{-7}\right)}{\log(1043) - \log(866.15)}$$

$$= \mathbf{-84.677 @ 593°C} \qquad \text{Equation (B13)}$$

$$n = \frac{\log\left(3.03x10^{-5}\right)}{\log(1043) - \log(922.15)}$$

$$= \mathbf{-84.486 @ 649°C} \qquad \text{Equation (B14)}$$

Average = –84.6

St.Dev. = 0.11

The resulting spread of data again has a less than one percent standard deviation resulting in the following expression of steady state creep rate as a function of temperature and stress.

$$\dot{\varepsilon}_{SS} = \left(\frac{\mathbf{T}}{\mathbf{1043}}\right)^{\mathbf{84.6}} \mathbf{exp}[\mathbf{0.044\sigma}] \qquad \text{Equation (4.1)}$$